Microstructural modeling of cross-linked fiber network embedded in continuous matrix

by

Lijuan Zhang

A Thesis Submitted to the Graduate

Faculty of Rensselaer Polytechnic Institute

in Partial Fulfillment of the

Requirements for the degree of

DOCTOR OF PHILOSOPHY

Major Subject: MECHANICAL ENGINEERING

Approved by the
Examining Committee:

_____
Mark S. Shephard, Thesis Adviser

_____
Catalin R. Picu, Thesis Adviser

_____
Antoinette M. Maniatty, Member

_____
David T. Corr, Member

_____
Victor H. Barocas, Member

Rensselaer Polytechnic Institute
Troy, New York

December 2013

CONTENTS

LIST OF TABLES

LIST OF FIGURES

ACKNOWLEDGMENT

Foremost, I would like to express my sincere gratitude towards my advisor Dr. Mark S. Shephard for his continuous support and encouragement during my graduate study in SCOREC. His guidance helped me in all the time of research and writing of this thesis. I am deeply grateful to have been given the chance to work as one of his graduate students.

I have also been fortunate to have Dr. Catalin R. Picu as my co-advisor during my Ph.D study. His technical advice and guidance is essential to the completion of the dissertation. I would also want to thank him for his patience of listening and answering the questions that come out during the research.

I would also like to thank the rest of my committee members: Dr. Antoinette M. Maniatty, Dr. David T. Corr and Dr. Victor H. Barocas, for their direction, dedication and invaluable advice along the project.

I am particularly grateful to Dr. Victor H. Barocas, who enriched me the knowledge on the biomechanics of soft tissues. His insightful comments and suggestions from a biological perspective greatly contribute to the thesis. This work would not have been possible without the help and contributions from our collaborators in University of Minnesota: Spencer Lake, Faisal Hadi and Victor Lai.

I would also like to thank the people of biotissue group for their help and suggestions: Xiaojuan Luo, Cameron Smith, Bill Tobin. Special thanks to my dear friends: Nanhu Chen, Yanheng Li, Peng Wu, Junqiang Zhang, Yi Chen, Li Zhang, Yixiao Zhang, Fan Zhang, Qiukai Lu, Shujuan Huang, Jianfeng Liu and Xuemei Gao.

Most of all, I would like to express my gratitude to my beloved parents Peng Zhang and Li Chen, as wells as the other family members for their love and support throughout my life.

Lastly, my profound gratitude goes to my husband, Zhi Li, for his remarkable patience and unwavering love all the time.

ABSTRACT

A soft tissue's macroscopic behavior is determined by its microstructural components (often a collagen fiber network surrounded by a non-fibrillar matrix (NFM)). In the present study, a coupled fiber-matrix model is developed to quantify the internal stress field within such a tissue and to explore interactions between the collagen fiber network and matrix.

Voronoi tessellations (representing the collagen networks) are embedded in a continuous three-dimensional NFM. To achieve computational efficiency, fibers are represented as one-dimensional wire edges embedded in three-dimensional matrix where conventional two-manifold geometric modeling is not applicable. Therefore non-manifold geometric modeling providing unified representation of general combinations of 1D, 2D and 3D geometric entities is employed in creating the geometry of fiber embedded matrix. After the (parasolid) geometric model is created, conforming mesh is generated by using automatic meshing tools.

Fibers are represented as one-dimensional nonlinear springs and the NFM, meshed via tetrahedra, is modeled as a compressible neo-Hookean solid. Three-dimensional finite element modeling is employed to couple the two tissue components, and the resulting representative volume element (RVE) is subjected to uniaxial tension. The overall coupled RVE response yields results consistent with those obtained using a previously developed parallel model based upon superposition. The detailed stress field in the composite RVE demonstrates the high degree of inhomogeneity in NFM mechanics, which cannot be addressed by a parallel model.

To gain additional insight in the mechanics of cross-linked fiber embedded in matrix, a linear material model is also employed to represent both the fibers and matrix and the solution fields are examined for the case of an isotropic network. As the matrix modulus increases, the network is constrained to deform more affinely. This leads to internal forces acting between the network and the matrix, which produce strong stress concentrations at the network cross-links. This interaction increases the apparent modulus of the network and decreases the apparent modulus of the matrix. A model is developed to predict the effective modulus of the composite and its predictions are compared with numerical data for a variety of networks.

A volume averaging based multiscale model is presented to effectively link the microstructure mechanics of the cross-linked fiber network to the overall tissue mechanics. This development demonstrates that the methodology developed can be applied to real systems and sets the stage for future developments and application to more complicated cases.

1. Background in soft tissue modeling and thesis organization

1.1 Background and motivation

Tissue engineering (TE) has emerged in the last few decades with the goal of developing tissues or organs *in vitro* to replace or support the injured or diseased body parts such as blood vessels, skin, ligaments, heart valves, tendon, menisci, cartilage and intervertebral discs. TE is an advantageous clinical treatment in that it completely avoids risks of immunological responses and viral infections which sometimes occur in organ transplantation from donors or other species. Moreover, compared to the vast majority of implants made of inert materials, engineered tissues are more biologically interactive and long-lasting therefore it has the enormous potential to bring the revolution to the next generation of implants [1, 2, 3].

The basic concept of TE involves (1) identifying and isolating cell sources (2) synthesizing appropriate polymeric materials to be later used as cell substrate and scaffold (3) seeding cells into or onto the scaffold (4) culturing the cells *in vitro* until desired tissue or organs are developed (5) placing engineered tissue or organ into appropriate *in vivo* site [3]. Biomechanics plays a very important role in the successful development of engineered tissues [1]. First of all, in the process of development, it is found that biomechanical stimuli are essential to producing engineered tissues with high strength and endurance. For example, in the field of vascular tissue engineering, cyclic mechanical distension is found to effectively strengthen the engineered arteries. Secondly, it must be ensured that engineered tissues could withstand and function within a specific biomechanical environment once implanted. Depending on their types, functional tissues are subjected to very complex physiological loadings in human beings. For instance, blood vessels transporting blood throughout the body have to distend in response to pulse waves; musculoskeletal tissues such as articular cartilage, bone, intervertebral disc, ligament, tendon, meniscus and muscles are all subjected to exceptionally high mechanical demand *in vivo*.

It is well known that the biomechanical response of both native and engineered tissues is largely determined by the properties of their underlying microstructures. Therefore, to allow for a better design of engineered tissues, it is meaningful to

investigate the relative contributions of microstructural components and how they relate to the overall mechanical response of soft tissues. The following section begins with an overview of general mechanical characteristic of soft connective tissues and briefly discusses how the morphology of microstructural components of soft tissues changes under tensile loading.

1.2 Mechanical behaviors of soft connective tissues: structure – function relationship

Soft connective tissues connect, support and protect our human body and other structures such as organs. Typical soft connective tissues include tendons, ligaments, blood vessels, skins and articular cartilages etc.. Compared to conventional materials (e.g. metals, wood, concrete, etc.) and hard tissues such as bones, soft tissues are characterized by the capacity of withstanding large deformation and very soft mechanical behaviors (Table 1). For instance, soft tissues such as aorta and articular cartilage could be strained up to 100% under tensile load.

Table 1.1: Mechanical properties and associated biochemical data of some representative organs mainly consisting of soft connective tissues [4].

Material	Ultimate Tensile Strength (Mpa)	Ultimate Tensile Strain (%)	Collagen (% dry weight)	Elastin (% dry weight)
Tendon	50-100	10-15	75-85	< 3
Ligament	50-100	10-15	70-80	10-15
Aorta	0.3-0.8	50-100	25-35	40-50
Skin	1-20	30-70	60-80	5-10
Articular Cartilage	9-40	60-120	40-70	-

The mechanical properties of many soft connective tissues are governed by a fiber network (primarily collagen in most tissues) and surrounding non-fibrillar matrix (NFM; e.g., proteoglycans, glycoaminoglycans, cells, etc.). Collagen is a protein which is the major load carrying constituent and is very important to mechanical integrity and strengths to human beings. Collagen fibrils generally are wavy and crimped, which are composed of collagen molecules being linked to each other by covalent bonds.

Depending on the primary function and strength requirement of soft tissues, the diameter of individual fibrils varies. Also, the arrangement of collagen fibrils is different from tissue to tissue. For tendon and ligament which are primarily loaded in tension, the structure of their collagen fibrils appears as parallel oriented fibers to maximum the load bearing capacity. Another example is intervertebral discs, where fibers of the annulus fibrosus are oriented in multiple directions to be able to adapt to the multiple loading environment. For many other types of soft tissues such as skins, the collagen fibrils form a very complex and cross-linked fiber network (Figure 1.1). The fiber arrangement (i.e. fiber orientation and connectivity) has a very close relationship with their global mechanical properties.

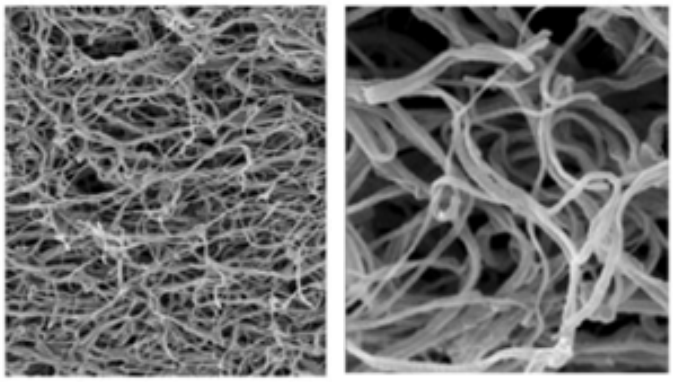

(a) 10,000X (b) 50,000X

Figure 1.1: Scanning electron images of collagen fiber network at (a) 10,000X and (b) 50,000X magnification [5].

It is well known that biological soft tissues have quite different mechanical behaviors than most conventional materials, which can be described by Hookes law. Generally, most soft tissues exhibit a nonlinear, inelastic, heterogonous, anisotropic character that varies from point to point, from time to time and from individual to individual [6]. The mechanical behaviors of soft tissues are closely related to the underlying microstructure (i.e. collagen network and interaction between collagen fibers and matrix materials). The tensile mechanical behavior of soft tissues shows nonlinear stiffening, which is related to the fact that the amplitude of the waviness of the crimped

fibers decreases at initial strain region and fiber reorientation to the load direction. Also, some tissues show viscous behavior (relaxation and creep), which are known to be associated with the viscous interaction between collagen fibrils and the matrix of proteoglycans.

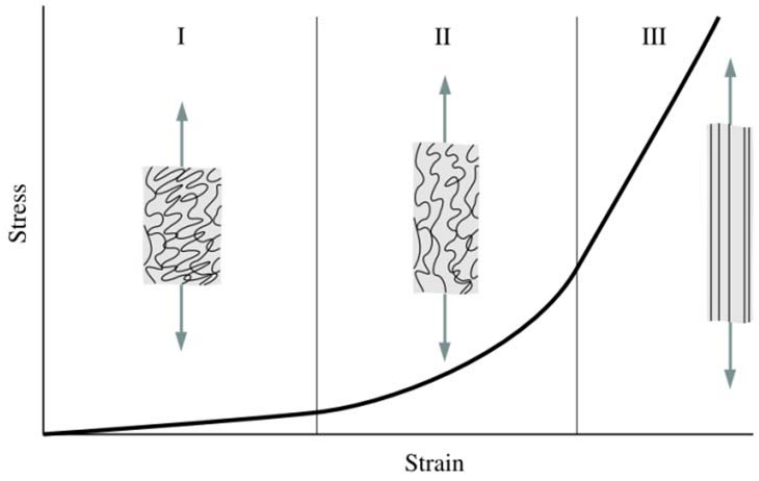

Figure 1.2: Schematic diagram of a typical (tensile) stress-strain curve for skin showing the associated collagen fiber morphology [4].

Figure 1.2 is a schematic diagram of a J-shaped (tensile) stress-strain curve for skin. The collagen fibers in unloaded condition appear wavy and crimped therefore in the initial stage (phase I), it does not require stretching every fiber of the network to achieve deformation, which results in a low stiffness response. The curve can be approximated with a straight line in the low strain range. As the load increases (phase II), the originally crimped fibers start to elongate and gradually reorient to the load direction, which leads to an obvious stiffening effect during this region. At higher tensile stresses (phase III), fibers become much straighter and aligned with the loading direction. The stress-strain curve becomes linear again, i.e. the axial deformation response of individual fibers determines the global system response.

1.3 Computational model developments

Early investigations on the constitutive modeling of soft tissues were based on phenomenological approaches, which describe the mechanical response of biological

materials under applied load by fitting a mathematic equation to the observed stress-strain curves of tissue specimens. Based on experimental elongation results on rabbits' mesentery, Fung [7] developed a one dimensional constitutive model for simple elongation where the tensile stress is an exponential form function of strain. Later, he expanded the one-dimensional model to 3D by postulating an existence of a three dimensional pseudostrain energy function $W = c(e^{Q} - 1)$, which led to an exponential relationship between second Piola-Kirchhoff stress tensor and the Green strain tensor.

There are other forms of strain energy functions proposed to describe mechanical behavior of various types of soft tissues. Early forms of strain energy function W borrowed ideas from the field of rubber elasticity because both rubberlike material and soft tissue are composed of similar long-chained, cross-linked polymeric microstructures. In such a framework, the strain energy function W is related to deformation by $W=W(I_C,II_C)$ in various forms, where $I_C=\mathrm{tr}(\boldsymbol{C})$, $II_C=(\mathrm{tr}(\boldsymbol{C}))^2 - \mathrm{tr}(\boldsymbol{C}^2)$ are coordinate invariant measures of the right Cauchy strain tensor $\boldsymbol{C}$ [6]. However, the disadvantage of such methods is that they are not able to capture the anisotropic behavior generally exhibited by biological materials. Later Humphrey [8] proposed a new form of pseudostrain-energy function W for transversely isotropic biomaterials such as myocardium. In his study, the strain energy function takes the following form: $W=W(I_C, IV_C)$ where $I_C=\mathrm{tr}(\boldsymbol{C})$ and $IV_C=\boldsymbol{M}\cdot\boldsymbol{C}\cdot\boldsymbol{M}$, with $\boldsymbol{M}$ denoting a measure of fiber orientation in such material obtained from a biaxial stretching test.

Although phenomenological models [7, 8, 9, 10] provided initial insights into the mechanics of fibrillar tissues, the disadvantage of such models is that it is unable to reveal the underlying mechanism that determines the mechanical behavior at functional scale. Hence, structural models [11, 12, 13, 14, 15, 16, 17, 18, 19] which include collagen fibers explicitly modeled as one of the components, have emerged to capture more information about the tissue architecture and they have been applied to a variety of intact tissues and tissue components such as lung, collagen, cartilage, mature skin.

In the work of Lanir et al. [11], the tissue total strain energy is assumed to be the sum of individual fiber strain energies transformed from individual fiber (local) coordinates to tissue (global) coordinates. This model allows the use of fiber orientation distribution information (experimental values or mathematic function) and individual

fiber constitutive models to formulate the tissue stress-strain relationship and is based on the affine deformation assumption. Based on Lanir's model, several researchers have successfully applied and refined the model to predict the mechanical behavior of a variety of tissues [13, 20, 21]. In order to directly incorporate quantitative structural information for direct implementation, Sacks [13] directly incorporated the fiber orientation distribution parameter obtained by using small angle light scattering (SALS) in the constitutive model formulation. And it was demonstrated that this model accurately predicted the measured biaxial mechanical response of native bovine pericardium by only requiring a single equibiaxial test to determine the effective fiber stress-strain response and the SALS-derived fiber orientation distribution. In order to capture the accurate stress-strain response of arterial layers, a general hyper-elastic free energy function was developed in by Gasser et al. [21] with explicit representation of the dispersion of collagen fiber orientation in the adventitial and intimal layers, as shown by polarized light microscopy of strained arterial tissue. In particular, by using continuous fiber angular distribution in articular cartilage matrix modeling, Ateshian [20] was able to predict the transition of very low Poisson's ratio (~0.02) in compression to very high values in tension (~2), which could not be explained by previous models with only three orthogonal fiber bundles to describe the tissue matrix.

Another approach adopted generalized structure tensors (GST) to model tissues with continuous distributed collagen fibers [22]. These tensors are used to represent the three-dimensional distribution of fibers. The strain of individual fiber is assumed affine and obtained as the multiplication of structure tensor and the global strain tensor. Compared to the approach based on continuous fiber orientation distribution, this approach is relatively simple and requires a smaller amount of calculations to get the fiber strain energy and stress. However, as pointed out in [14], this approach can only be used when fibers are all in tension and the angular distribution is small.

In the aforementioned literature, there is a key assumption that individual collagen fibers are acting independently (i.e. without interaction with other fibers) and deform according to the macroscopic deformation field, which is popularly known as the 'affine' model. However, these models perform poorly when applied to networks with low density or networks subjected to complex loading paths [23]. Nonaffine deformation is

widely observed in experimental studies [24, 25]. In order to investigate the effect of network nonaffinity (NA) on the overall mechanical behavior of soft tissues, full network models composed of interconnected fibers allowing for fiber-fiber interaction have been developed. Fiber crosslinks are modeled as pin-joints [26] or rotation joints (pin joint transmits no moments and fiber only carries axial force; however, rotation joint allows bending of fibers) [27, 28, 29]. The degree of non-affinity is determined by network density, individual fiber constitutive properties and also the observation scale. Chandran [26] compared the affine-model and the network model and it was shown that the network behavior was actually characterized by extensive fiber reorientation and moderate stretch ratios, which in turn gives a softer mechanical response of the network on the system level than affine approaches. Onck [30] indicated that strain-stiffening observed in semi-flexible networks (e.g. cytoskeleton) is caused by nonaffine network arrangement, which governs a transition from bending-dominated response at small strain to stretching dominated response at large strains. They also indicated that filament undulations merely postpone the transition. Liu [31] measured the local strain field for a semi-flexible network under shear and observed that the degree of nonaffinity increases with the decrease of crosslink density.

Various measures have been used to quantify the degree of nonaffinity [29, 30, 32, 33]. A strain-based measure was introduced in [29] by Hatami-Marbini and Picu to probe the network mechanics at various scales. The degree of NA decreases as the length scale of observation increases and the scaling is a power law with different exponents for length scales smaller or larger than a characteristic length scale proportional to the fiber length. It was also found that as bending stiffness of fibers increases relative to axial stiffness, the NA decreases. Onck [30] employed a nonaffine (NA) measure $||\delta\mathbf{u}-\mathbf{u}_{aff}||$ (where $\mathbf{u}$ is the actual displacement of crosslinks and $\mathbf{u}_{aff}$ is the corresponding affine displacement) and showed that the degree of NA decreases when the network is subjected to large deformations.

The mechanical interaction between collagen fiber network and the nonfibrillar matrix is also being studied. Nonfibrillar matrix is often modeled using a simple mathematical representation, such as Neo-Hookean [34, 35, 36, 37] or Mooney-Rivlin [38, 39, 40, 41] and is assumed to contribute to the fiber-matrix composite in a summed

or ‘parallel’ sense. For instance, in the study on mechanical modeling of arterial wall conducted by Holzapfel [34], the isochoric strain energy function Ψ of the two layered fiber reinforced composite was considered to be the summation of two parts, Ψ_{iso} associated with the mechanical response of non-matrix material and Ψ_{aniso} associated with the anisotropic mechanical behavior of collagen fibers. Similarly, in Tang et al. [36], the contribution of matrix material was accounted for by an additional strain energy in neo-hookean form weighted by the volume ratio of the matrix material. Some other models [42, 43, 44] have utilized an additional term to account for the fiber-matrix interaction. However, in general, the appropriate definition for the interaction term is unknown. To overcome this limitation, the current study presents a method wherein the collagen fiber network and surrounding NFM are microscopically coupled, making it possible to evaluate specifically the interaction between fibers and matrix.

1.4 Organization of dissertation

Chapter 2 discusses the pre-processing step for the coupled fiber-matrix model. In order to use automatic meshing to create fiber-matrix finite element model, non-manifold geometric representation is employed. Then it introduces the non-manifold geometric creation for the fiber embedded matrix and specifies the topological adjacencies between topological entities that make up the geometric model. Next the multi-dimensional mesh generation is described to derive both the isotropic and graded meshes from the created geometry.

Chapter 3 presents the nonlinear finite element formulations for the coupled fiber-matrix system. Both geometric and material nonlinearities are taken into account in the nonlinear finite element analysis. Tangential stiffness matrix and force vector are derived for the coupled fiber-matrix system. Standard Newton’s iteration is employed to solve the nonlinear equations.

Chapter 4 analyzes the finite element results of the uniaxial extension by employing the coupled fiber-matrix model. The overall constitutive response of the coupled fiber-matrix system is compared with the parallel model for the same set of input parameters; Interactions between the two constituents are investigated by examining the stress distribution of the matrix material and the nonaffine measure of network deformation;

An analytical method is proposed to predict the effective elastic modulus and Poisson's ratio of the RVE composite.

Chapter 5 presents a volume averaging based multiscale model to effectively link the microstructure mechanics to the overall tissue mechanics. By applying the multiscale approach, fiber reorientation occurring in the tissue microstructure is captured in the dogbone uniaxial extension test.

Chapter 6 concludes the present work and describes possible future improvements.

2. Non-manifold geometry modeling and mesh generation

2.1 Introduction and overview of the coupled model

Microstructural modeling is essential to characterize and quantify the roles of collagen and non-fibrillar matrix (NFM) in imparting mechanical properties to soft tissues at functional level. Recently, a computational network-based microstructural model (referred here as parallel model) was developed by our collaborators to examine how specific NFM properties alter the response of fiber-matrix composites under load [45]. This model is constructed according to the conventional "parallel" approach of superposition of the two constituents (i.e., collagen network and NFM). Some relevant details of the parallel model are provided here for clarity. In the parallel model, the stress due to the collagen network is computed via a volume-averaging approach based on the nodal forces on each RVE boundary:

$$\sigma_{ij}^{n} = \frac{1}{V} \sum_{\substack{boundary \\ node}} x_i f_j \tag{2.1}$$

where superscript 'n' represents network, V is RVE volume, and f_j are the forces acting on boundary nodes (at positions x_i). The Neo-Hookean NFM stresses $\boldsymbol{\sigma}^m$ are dependent only on the macroscopic deformation of the RVE, and the two stress fields are combined in a simple summed (parallel) sense [45]:

$$\sigma_{ij} = \sigma_{ij}^{n} + \sigma_{ij}^{m} \tag{2.2}$$

where σ_{ij} denotes the total stress.

As shown in Chapter 4, the parallel model and the current developed coupled model could produce reasonably close prediction in gross soft tissue behavior such as averaged stress for certain ranges of system parameters. However, the drawback of the parallel model is that it is unable to examine interactions between collagen fibers and the surrounding NFM or to identify inhomogeneities in the stress field[1]. For example, in a uniaxial extension experiment, the average transverse and shear stresses would be zero, but local shear would surely occur in the neighborhood of a fiber. Such local stresses

[1] Portions of this chapter previously appeared as: L. Zhang, S. P. Lake, V. K. Lai, C. R. Picu, V. H. Barocas, and M. S. Shephard, "A coupled fiber-matrix model demonstrates highly inhomogeneous microstructural interactions in soft tissues under tensile load," *J. Biomech. Eng.*, vol. 135, p. 011008, Jan. 2013.

could be much larger than average values, which could have important implications in initiating failure of the NFM or in greatly altering the site-specific cellular environment. Therefore, a fully coupled fiber network and matrix model is developed in present study, which is capable of (a) quantifying local stresses throughout the computational domain and (b) exploring interactions between NFM and the embedded collagen network. The coupled model can also be used in the future to study material failure driven by fiber or matrix damage accumulation.

Both the parallel model and the current coupled fiber-matrix model are based on a full fiber network representation with direct account for interactions between individual fibers, which can be modeled as three-dimensional cylinders or simplified one-dimensional structural elements (i.e., truss or beam). However, it has been shown that explicit representation of the volume of fibers is not necessary when volume fraction occupied by fibers is small [46]. Furthermore, in the coupled fiber-matrix model, the matrix prevents the fibers from coming in direct contact with each other during deformation at points other that the existing cross links, so representing the fiber volume is also not critical from this point of view. The coupled model is shown in Figure 2.1. The cubic simulation representative volume contains a network of trusses which are joined at all crossing points by freely rotating pins. These links transmit forces, but not moments. The network has additional nodes at the intersection points with the boundaries of the volume element. The finite element method is adopted in the coupled fiber-matrix model, in which the geometric domain of the RVE is discretized into a finite element mesh that will maintain an appropriate alignment with the fibers.

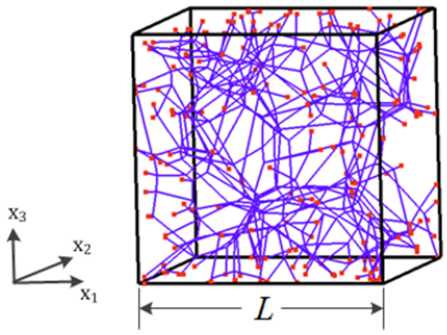

Figure 2.1: Schematic representation of the network: The red dots represent the points where the network intersects the model boundaries.

The workflow for applying the finite element method (see Figure 2.2) includes four steps: (1) Creation of a fiber network; (2) creation of the geometric model represented in non-manifold form based on the generated fiber network; (3) multidimensional mesh generation from the created geometry; and (4) formulation and solution of finite element equations of the coupled fiber and matrix system.

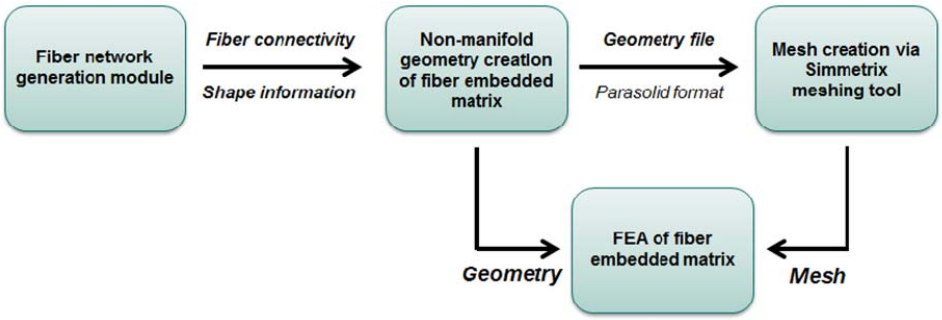

Figure 2.2: Work-flow demonstrating construction protocol for the coupled model.

This chapter presents the methods used for the first three steps, which are Voronoi fiber network generation (section 2.2), non-manifold geometry creation of fiber embedded matrix (section 2.3) and multi-dimensional mesh generation (section 2.4). Chapter 3 presents the finite element formulation of the fiber network with matrix.

2.2 Voronoi fiber network generation

Voronoi networks are used to represent the locations of fibers in the unit cell in the present study due to their ability to provide a close approximation to collagen gel behavior [47]. Such networks exhibit very large Poisson's ratios (~3) similar to those observed experimentally due to its low coordination number compared to other types of model networks [5]. This section overviews the process of Voronoi fiber network generation, the output of which is used as input for generating the geometry of fiber network within a matrix material.

The procedure of Voronoi network generation is shown in Figure 2.3 and summarized as follows [45]:

Step 1: Seed points are randomly placed in a cubic box with side length L.

Step 2: The Voronoi tessellation is formed around the generated seed points.

Step 3: The edges of the Voronoi cells become network segments.

Step 4: Nodes are placed at edge intersections and at intersections with the cube boundaries.

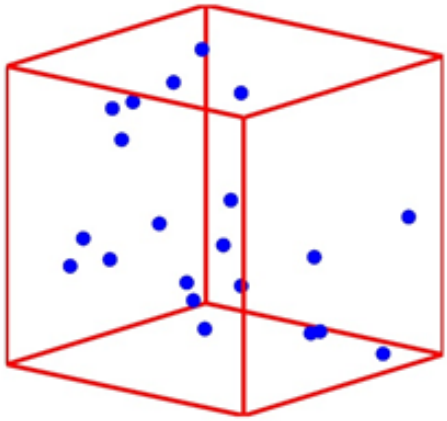

Step 1. Random seed points

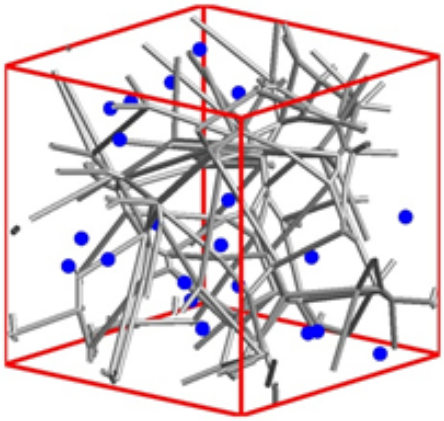

Step 2. Voronoi Tessellation

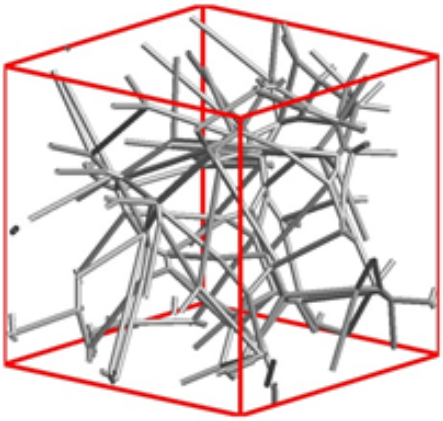

Step 3. Fiber Network

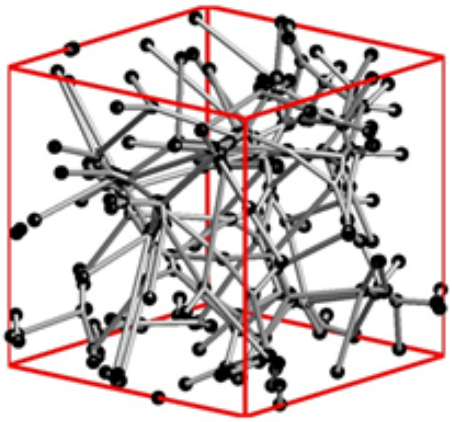

Step 4. Nodes at intersections of fibers and between fibers and boundaries

Figure 2.3: Procedure of Voronoi network generation.

Note that in this model fibers do not carry cross-links in the middle of the fiber span. There are only two cross-links per fiber and these are placed at the ends of the respective fiber where it either intersects other fibers or the RVE boundary. The generated network contains two essential components of information, which completely defines the network configuration:

(1) Fiber connectivity defining which fiber is adjacent to which fiber crosslinks;

(2) Spatial coordinates of crosslinks.

The following are the input parameters used to characterize the generated Voronoi networks:

- Network density ρ, defined as the total length of fibers per unit volume:

$$\rho = \frac{\sum_{i}^{N} l_i}{L^3} \tag{2.3}$$

where N is the total number of fibers, l_i is i-th fiber length and L is the side length of the unit cube.

- Mean segment length l_c:

$$l_c = \frac{\sum_{i}^{N} l_i}{N} \tag{2.4}$$

- Fiber orientation parameter:

$$\Omega_{11} = \frac{\sum_{i}^{N} {l_{1i}}^2 / l_i}{\sum_{i}^{N} l_i}, \Omega_{22} = \frac{\sum_{i}^{N} {l_{2i}}^2 / l_i}{\sum_{i}^{N} l_i}, \Omega_{33} = \frac{\sum_{i}^{N} {l_{3i}}^2 / l_i}{\sum_{i}^{N} l_i} \tag{2.5}$$

where l_{1i} , l_{2i} and l_{3i} are the projections of fiber length in x_1, x_2 and x_3 directions respectively. For an isotropic network, $\Omega_{11} = \Omega_{22} = \Omega_{33} = 1/3$; for a perfectly aligned network in x_1 direction, $\Omega_{11} = 1$ [48].

These network parameters play an important role in determining the overall network behavior as shown in [23, 26, 29, 48]. The result analysis presented in Chapter 4 uses these parameters to identify different random networks.

2.3 Non-manifold geometric modeling using Parasolid

The geometric model contains topological and shape information of the object being analyzed. In the current study, the geometry of fiber network within solid matrix is created based on a full representation of the embedded fiber network, i.e. the connectivity of the fibers and spatial coordinates of fiber crosslinks are explicitly represented and could be queried by CAD modelers. Since each individual embedded fiber is considered as one-dimensional geometric edge, which has zero cross-section area, conventional manifold modeling is not able to properly represent the desired model. Instead, non-manifold form, which provides a much more general geometric representation, is adopted in the current geometric modeling.

2.3.1 Introduction to non-manifold and manifold models

Compared to manifold solid presentation, non-manifold form is able to provide a unified representation of general combinations of 1-D, 2-D and 3-D geometric entities. A manifold (more strictly stated 2-manifold) solid representation is one where every point on a surface is two dimensional, which means that every point on the boundary has a boundary neighborhood which is homeomorphic to a two-dimensional disk [49]. However, non-manifold geometric models do not maintain this constraint. In other words, the surface area around a given point need not be a simple two-dimensional disk. Hence, in such a framework, it allows non-manifold situations such as a cone touching upon another surface at a single point, wire edges embedded in solid volume or emanating from a point on a surface, or more than two faces meeting along a common edge. These situations are common to engineering analysis idealizations and it greatly increases the efficiency and productivity in engineering practices if one could account for these situations appropriately. For example, finite element meshes where interior mesh faces are shared by two mesh regions (Fig 2.4(a)) within two different material regions can be conveniently represented in a non-manifold form. In the area of composite modeling where the diameter of single embedded fiber is much smaller than the overall size of the composite, it is natural to consider the composite as a multi-dimensional case (Figure 2.4(b)) in which the fiber is represented as one-dimensional wire edges as opposed to a three dimensional solid region.

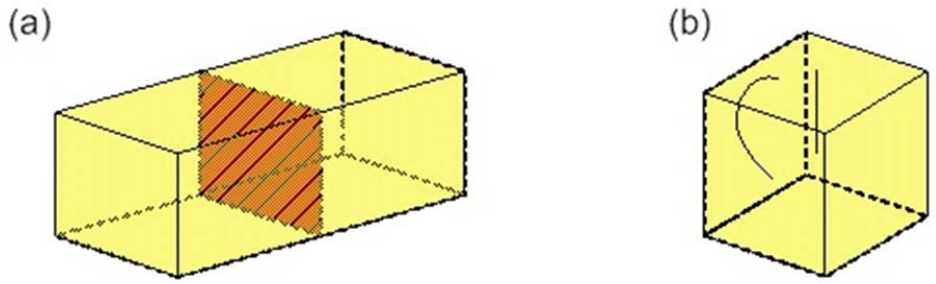

Figure 2.4: (a) Cellular body: Interior face shared by two regions – each side of the face is used by the associated region; (b) Multi-dimensional body: Three-dimensional region with embedded one-dimensional wire edges.

2.3.2 General description of construction of the non-manifold geometric model

The Parasolid geometric modeling kernel [50] is employed to construct the non-manifold geometric representation of the fiber-matrix model. This section uses the same terminology as used in Parasolid.

Following the definition of a geometry, which is topology with attached geometric information, the process of creating the non-manifold fiber-matrix model is therefore conducted in two steps: the first is to construct the topology by specifying topological entities that make up the model and describing adjacent relationships between these entities; Once the topology is constructed, the geometric information defining the shape of that entity is attached to associated topological entities. A description of topology and geometric entities is provided first; then the non-manifold topological adjacencies of the specific case-multi-dimensional fiber-matrix model are discussed.

Topology and topological entities

Topology serves as the structure or skeleton of a geometric model. It consists of topological entities that are linked through a set of adjacent relationships.

Types of topological entities include:

- **Body**

A body could be considered as a repository for all topological entities from zero to three dimensions.

- **Region**

A region is a connected volume of space whose boundary is a collection of shells. Regions could be either solid or void (empty). A body always has an infinite void region, which could be considered as all the space outside the body itself.

- **Shell**

In a manifold representation, a shell is a connected set of faces (each used by shell on one side of the face) which form a closed volume. However, in a non-manifold representation, the definition of a shell is much more general, which could be a combination of adjacent faces, a wireframe or even a single vertex.

- **Face**

A face is a bounded portion of a shell. Its boundary is a collection of zero or more loops. An example of zero loop is a spherical surface.

- **Loop**

A loop is a connected boundary of a single face. It consists of an oriented sequence of edges (Figure 2.5(a)) or may be just a single vertex loop or wire loop (Figure 2.5(b)).Vertex or wire loops are corresponding to vertices or edges scribed inside a face. Fiber crosslinks on the RVE boundaries are represented as vertex loops.

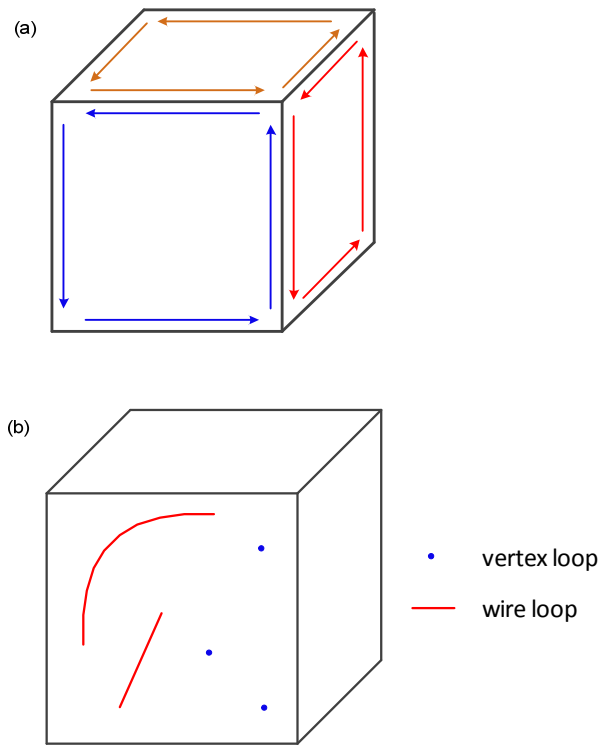

Figure 2.5: (a) Loops of a solid cube (only shows loops of three faces); (b) Vertex and wire loops.

- **Fin**

A fin represents an oriented use of an edge by a loop. The direction of the fin is the same as that of a loop that contains the fin. In the case of solid cube (Figure 2.5(a)), each cube edge has two fins in opposite direction. For a wire edge (Figure 2.5(b)), there is no fin.

- **Edge**

An edge is bounded portion of a curve. An edge which is not connected to any face is called a wire edge.

- **Vertex**

A vertex represents a point in space.

Geometric entities

Geometric entities define the shape information associated with the topological entities in a geometric model. Types of geometric entities include:

Surfaces are attached to faces of the model.

Curves are attached to edges or fins of the model.

Points are attached to vertices. All points are Cartesian points.

2.3.3 Constructing the non-manifold model of fiber and matrix

The non-manifold topological adjacencies for the geometry of fibers within matrix are discussed based on the rules of non-manifold geometric model construction. To make the description clearer, a case with three embedded fibers (Figure 2.6) in solid matrix is used as an example.

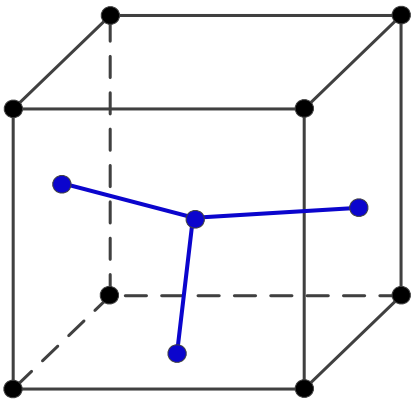

Figure 2.6: Three fibers within matrix – blue lines and blue dots represent embedded fibers and fiber crosslinks (only one inner crosslink, the other three are boundary crosslinks); black lines and black dots represent cube edges and cube vertices.

The geometry in Figure 2.6 contains the following topologies entities:

Body: there is only one body which serves as a container to hold all topological entities.

Regions: an infinite void region and a solid region.

Shells: two shells here. A shell enclosing the void region and a shell associated with the solid region. The shell enclosing the solid region consists of cube faces (inner side of cube faces is used by the solid region) and embedded three wire edges representing fibers.

Faces: six RVE cube faces (Figure 2.7). The normal of the faces in a solid body must point away from the solid region.

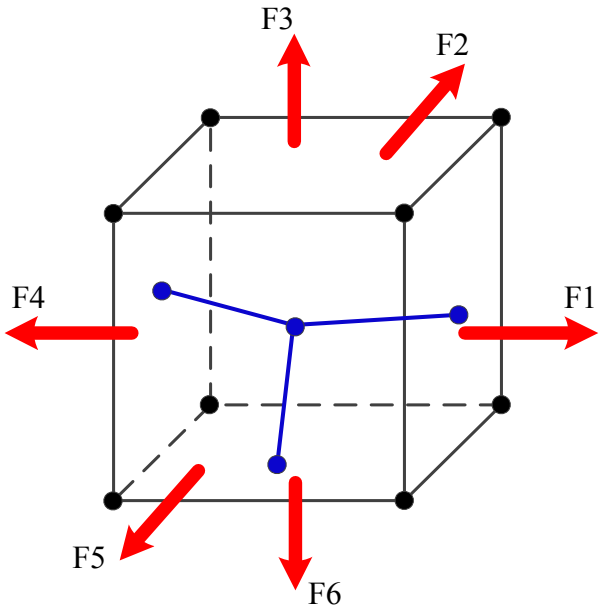

Figure 2.7: Faces of the studied case with red arrows representing face normal.

Loops: there are two types of loops (Figure 2.8). One type is the loop that bounds a cube face; the other type is the single vertex-loop that is associated with the intersection of fibers with RVE cube faces. For the type of loops comprised of a sequence of edges, the 'forward' direction of the loop has the face on the left of the loop, when viewing the face down the face normal.

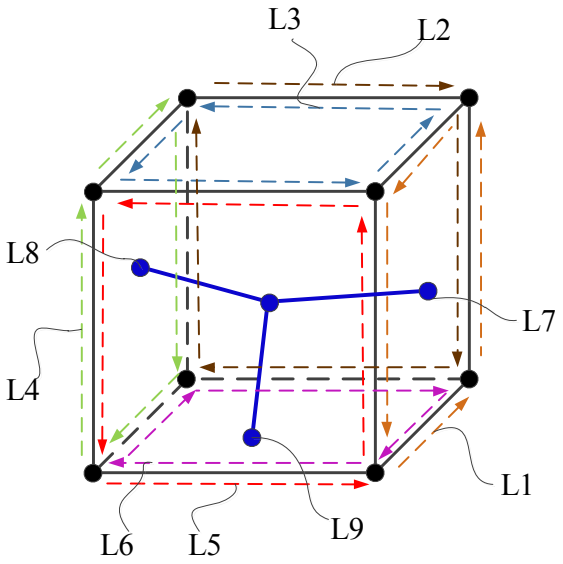

Figure 2.8: Loops of the studies case: L1 through L6 are six loops bounding cube faces; L7, L8 and L9 are vertex loops.

Edges: there are also two types of edges (Figure 2.9). One type is those edges that form loops bounding cube faces. The other type of edges is wire edges representing embedded fibers.

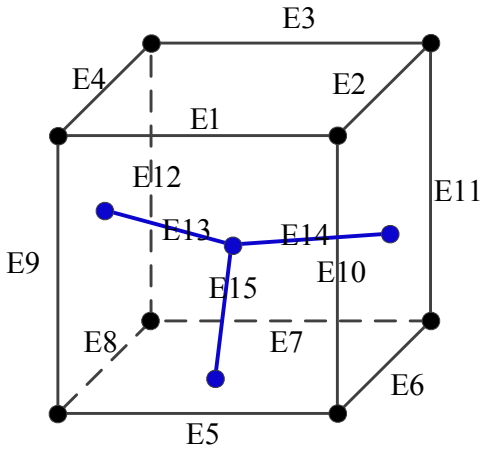

Figure 2.9: Edges of the studied case: E1 through E12 are cube edges; E13, E14 and E15 are wire edges associated with embedded fibers.

Vertices: there are eight vertices associated with cube and other vertices associated with fiber crosslinks (including boundary crosslinks) (Figure 2.10).

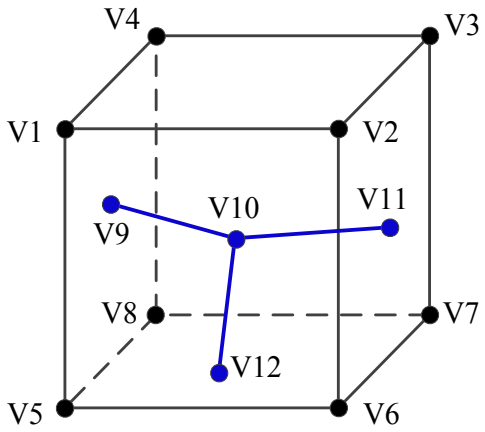

Figure 2.10: Vertices of the studied case: V1 through V8 are cube vertices; V9, V10, V11 and V12 are vertices associated with fiber crosslinks in which V10 is an embedded vertex.

To create a topology using Parasolid, it is required to specify all topological adjacencies between topological entities existing in the model one would want to generate. Following terminology in Parasolid, each topological adjacent relationship is defined by three entries: parent, child and sense; 'Parent' and 'Child' refer to two adjacent topological entities; 'Sense' indicates the manner in which a child is used by its parent. In relationships in which 'sense' matters, 'sense' should be set to 'positive' or 'negative'; In relationships in which 'sense' does not matter, it should be set to 'none'. Table 2.1 to 2.8 list topological adjacent relationships between each topological entity described in section 2.3.3. When using Parasolid to create topology, these listed topological adjacent relationships need to be specified.

Table 2.1: Body ~ Region adjacent relationships.

Parents	Children	Senses
Body	R_void	negative
Body	R_solid	positive

'Negative' means the region is void; 'Positive' means the region is solid.

Table 2.2: Region ~ Shell adjacent relationships.

Parents	Children	Senses
R_void	Shl_void	none
R_solid	Shl_solid	none

Table 2.3: Shell ~ Face adjacent relationships.

Parents	Children	Senses
Shl_void	F1,F2,…,F6	positive
Shl_solid	F1,F2,…,F6	negative

'Positive' means the face normal points to the interior of the shell and 'negative' means the face normal points away from the interior of the shell.

Table 2.4: Shell ~ (Wire) Edge adjacent relationships.

Parents	Children	Senses
Shl_solid	E13	none
Shl_solid	E14	none
Shl_solid	E15	none

Table 2.5: Face ~ Loop adjacent relationships.

Parents	Children	Senses
F1	L1	none
F2	L2	none
F3	L3	none
F4	L4	none
F5	L5	none
F6	L6	none
F4	L8	none
F6	L9	none
F1	L7	none

Table 2.6: Loop ~ Edge adjacent relationships.

Parents	Children	Senses
L1	E6	positive
L1	E11	positive
L1	E2	positive
L1	E10	positive
L2	E7	positive
L2	E11	negative
L2	E3	positive
L2	E12	positive
L3	E1	positive
L3	E2	negative
L3	E3	negative
L3	E4	positive
L4	E4	negative
L4	E12	negative
L4	E8	positive
L4	E9	positive
L5	E1	negative
L5	E9	negative
L5	E5	positive
L5	E10	negative
L6	E5	negative
L6	E6	negative
L7	E7	negative
L8	E8	negative

‘Positive’ means the edge is in the same direction of as the loop; ‘negative’ means the edge is in the opposite direction to the loop.

Table 2.7: Loop ~ Vertex adjacent relationships.

Parents	Children	Senses
L7	V11	none
L8	V9	none
L9	V12	none

Table 2.8: Edge ~ Vertex adjacent relationships.

Parents	Children	Senses
E1	V1,V2	none
E2	V2,V3	none
E3	V3,V4	none
E4	V4,V1	none
E5	V5,V6	none
E6	V6,V7	none
E7	V7,V8	none
E8	V8,V5	none
E9	V1,V5	none
E10	V2,V6	none
E11	V3,V7	none
E12	V4,V8	none
E13	V9,V10	none
E14	V10,V11	none
E15	V10,V12	none

2.4 Multi-dimensional mesh generation

Once the geometry of fiber network within matrix is created, the next step is to load the geometry into mesh generator to create an appropriate mesh. In the present study, Simmetrix Inc. meshing tools [51] are used to create the conforming mesh from the generated geometry. The generated mesh is multi-dimensional with 3D tetrahedrons for the solid matrix and 1D truss elements for the collagen fibers. The solid matrix and embedded fiber network are meshed together such that mesh vertices and mesh edges on the fibers are shared with the adjacent 3D solid elements (Figure 2.11). Figure 2.12 shows the interior of the mixed dimensional mesh with shapes of elements intersecting the cutting plane retained.

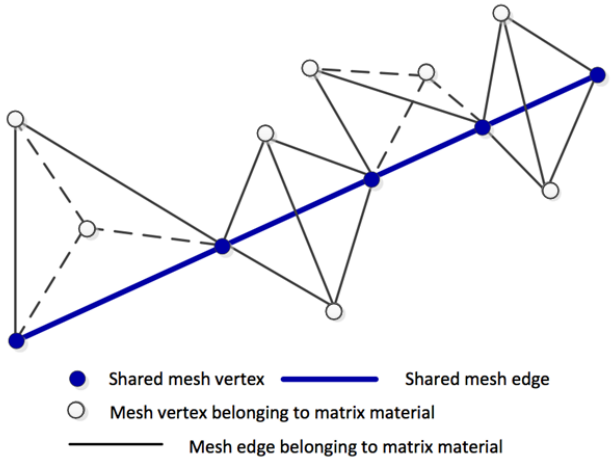

Figure 2.11: Illustration of the conforming multi-dimensional mesh and the mesh classification to the geometric model.

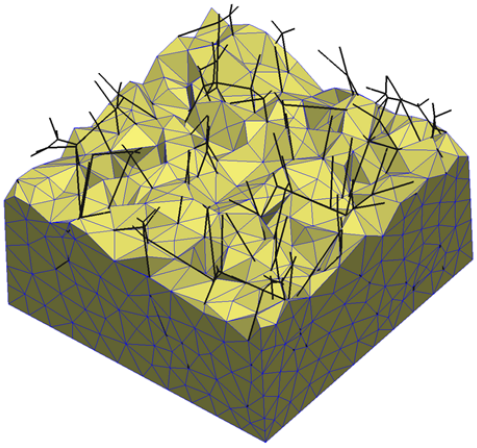

Figure 2.12: Schematic showing the interior of the multi-dimensional mesh showing fibers (black lines) and meshed matrix (yellow elements with blue borders).

Both uniform (Figure 2.13) and graded meshes (Figure 2.14) can be generated and used in finite element analysis. If only global behaviors such as averaged stress are interested, uniform mesh generation could be applied to gain computational efficiency. However, if local stress/strain field inside the RVE computational is interested, a graded mesh is preferred.

Uniform mesh is generated by specifying a global mesh size on the entire model. Assume the RVE side length is L, the mesh shown in Figure 2.13 is obtained by setting

the mesh size to 0.1L. Besides setting the mesh size on the model, one could locally refine the mesh by specifying mesh size on given model entities around which stress concentration occurs or deformation gradient is relatively large. Therefore, in the current case of RVE composite with random fiber network embedded in the matrix, a smaller mesh size is specified on embedded fibers and crosslinks. The graded mesh in Figure 2.14 is corresponding to a mesh size of 0.05L set on fibers and 0.025L set on crosslinks.

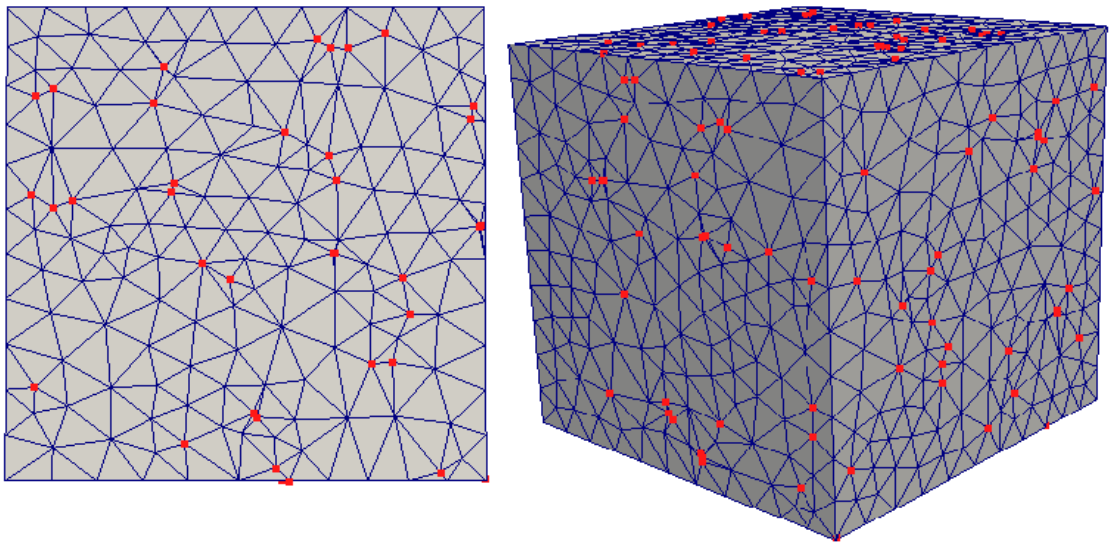

Figure 2.13: 2D and 3D view of uniform multi-dimensional mesh (red dots represent fiber boundary crosslinks).

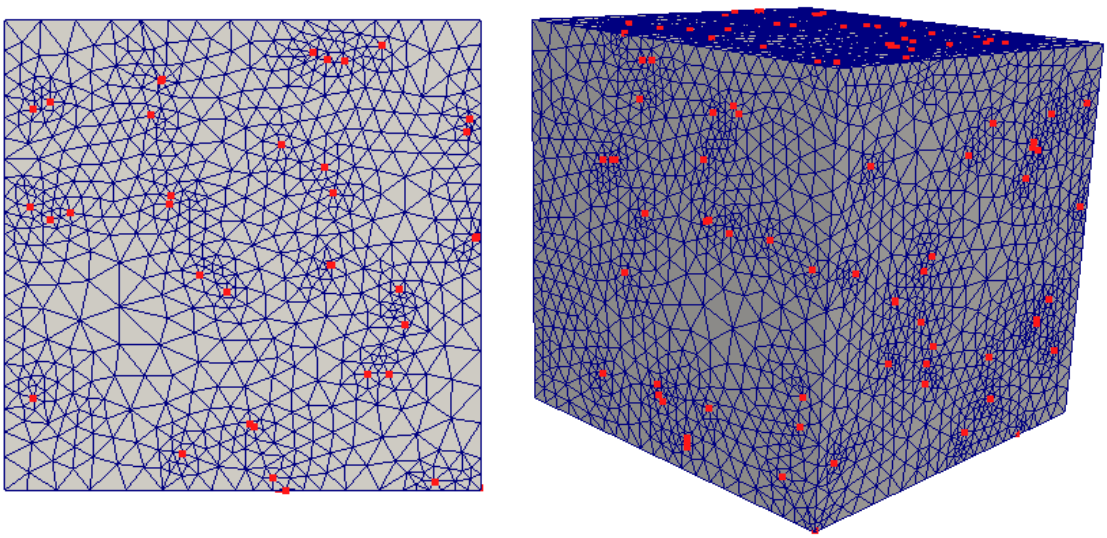

Figure 2.14: 2D and 3D view of graded multi-dimensional mesh (red dots represent fiber boundary crosslinks.

Multiple nodes may be created along a fiber span in the process of meshing (Figure 2.11). These nodes are not cross-links. However, because the fibers are represented using truss elements, placing a node in the middle of a fiber span implies placing a physical hinge at that location. From a modeling point of view, this does not change the fiber behavior significantly in that since fibers have a high aspect ratio, they will carry very little compressive load. In the current model, the fibers between cross links are straight and hence when loaded in tension, the effect of such hinge is not seen. On the other hand, when loaded in compression, the lateral constraint provided by the matrix prevents the fiber from buckling with no constraining force at the hinge and, again, the effect of the node added within the fiber span is minimal, i.e. the fiber responds in compression approximately the same with how it would respond to the same load if it were continuous.

3. Finite element analysis of the coupled fiber-matrix model

In this chapter the nonlinear finite element equations needed to predict the mechanical behavior of the coupled fiber-matrix system are presented. The source of nonlinearity of the current study comes from material nonlinearity and geometric nonlinearity (large deformations). The material models adopted for representing embedded fibers and matrix materials are presented in section 3.1. Section 3.2 presents the nonlinear finite element equations formulated for 3D linear tetrahedrons and 1D truss members while section 3.3 presents the assembling process with coupled tetrahedrons and truss members.

3.1 Material model representing embedded fiber and matrix

Collagen fibers are represented as one-dimensional nonlinear members with constitutive behavior defined as [45, 52]:

$$f^{fib} = \frac{E_f A}{B}(e^{B\varepsilon} - 1) \tag{3.1}$$

where f^{fib} is the axial force in a given fiber, E_f is the fiber Yong's modulus in the zero-strain limit, A is the fiber cross-sectional area, B is a nonlinearity constant and ε is the fiber Green's strain along the fiber, defined as $\varepsilon = 0.5(\lambda^2 - 1)$ where λ is the fiber stretch ratio. Eq. (3.1) specifies properties for individual fibers; of course the mechanical response of each RVE result from the collective behavior of the full network of fibers. The present study uses the same value of material parameters as in [52]: E_fA=0.0065827N, B=3.8.

The non-fibrillar matrix (NFM) is represented as a compressible neo-Hookean solid, with the second Piola Kirchhoff stress tensor $\boldsymbol{S}$ defined as [53]:

$$\boldsymbol{S} = G_m \boldsymbol{I} - G I_3^{-\beta} \boldsymbol{C}^{-1} \tag{3.2}$$

where G_m is the NFM shear modulus, $\boldsymbol{I}$ is the identity matrix, $I_3=\lambda_1\lambda_2\lambda_3$, $\lambda_1,\lambda_2,\lambda_3$ are eigenvalues of $\boldsymbol{C}$, which is the right Cauchy deformation tensor, $\beta = \nu_m / (1 - 2\nu_m)$, and ν_m is Poisson's ratio of the NFM. As done previously [45], ν_m is set to 0.1. The NFM shear modulus is varied over a range of values (G_m = 10, 110, 720 and 4300 Pa) corresponding to 0.05, 0.125, 0.25 and 0.5 % w/v (weight of the solute in volume)

agarose in our experimental collagen-agarose studies [5]. To assess the role of compressibility, a set of simulations with low compressibility of v_m =0.45 is also evaluated for G_m=110 Pa.

As discussed in section 3.2, the formation of the tangent stiffness matrix requires evaluation of the material tangent elasticity tensor (fourth order) $\hat{C}_{ijrs}$ defined as

$$\hat{C}_{ijrs} = \partial S_{ij} / \partial \varepsilon_{rs}, i, j, r, s = 1, 2, 3 \tag{3.3}$$

where ε_{rs} is the Green strain tensor.

With the NFM modeled as neo-hookean Eq.(3.2), the material tangent elasticity $\hat{C}_{ijrs}$ is expressed as [53]:

$$\hat{\boldsymbol{C}} = \delta_1 \boldsymbol{C}^{-1} \otimes \boldsymbol{C}^{-1} + \delta_2 \boldsymbol{C}^{-1} \odot \boldsymbol{C}^{-1} \tag{3.4a}$$

$$\delta_1 = 2\beta G I_3^{-\beta}, \delta_2 = 2G I_3^{-\beta} \tag{3.4b}$$

$$(\boldsymbol{C}^{-1} \otimes \boldsymbol{C}^{-1})_{ijkl} = C^{-1}{}_{ij} C^{-1}{}_{kl} \tag{3.4c}$$

$$\left(\boldsymbol{C}^{-1} \odot \boldsymbol{C}^{-1}\right)_{ijkl} = \frac{1}{2}(C_{ik}^{-1} C_{jl}^{-1} + C_{il}^{-1} C_{jk}^{-1}) \tag{3.4d}$$

3.2 Nonlinear finite element formulation of the coupled fiber-matrix model

In a linear analysis, it is assumed that the displacements of the body under consideration are infinitesimally small and that the material is linear elastic. With these assumptions, there is no need to differentiate between initial (undeformed) and current (deformed) configuration and therefore engineering stress and strain are appropriately employed to formulate the equilibrium equations. However, when the body exhibits large deformations, the equilibrium equations need to be established in the current configuration.

In practice, the calculation of the finite element solution is carried out in a step by step manner instead of applying the external load all together to ensure that the nonlinear iteration converges. In a nonlinear analysis, the aim is to evaluate the equilibrium state of the body at the discrete load points 0, Δt , $2\Delta t$, $3\Delta t$, …, where Δt represents the load increment. In the following section, it is assumed that solutions of static and kinematic

variables for all load steps from 0, Δt , 2 Δt, …, have all been calculated. The task is to seek the unknown state corresponding to load level at $t + \Delta t$. A standard Newton-Raphson iterative approach [54, 55] is adopted here to solve the nonlinear finite element equations. The iterative procedure is described in Section 3.2.1; the derivation of the linearized finite element equations including tangential stiffness matrix and residual force vector with respect to linear tetrahedrons and truss members is presented in subsequent sections.

3.2.1 Newton-Raphson iterative approach

The equilibrium state of a system of finite elements representing the problem domain corresponding to load level $t + \Delta t$ is expressed as

$$\boldsymbol{f}_{int}^{t+\Delta t}(\boldsymbol{u}^{t+\Delta t}) = \boldsymbol{f}_{ext}^{t+\Delta t} \tag{3.5}$$

where $\boldsymbol{f}_{int}^{t+\Delta t}$ and $\boldsymbol{f}_{ext}^{t+\Delta t}$ are internal ('int') and external ('ext') nodal force vectors and $\boldsymbol{u}^{t+\Delta t}$ is the nodal displacement vector at equilibrium state of load level $t+ \Delta t$.

Using Taylor's series and assuming $\boldsymbol{u}^{t+\Delta t} = \boldsymbol{u}_{(i)}^{t+\Delta t} + \Delta \boldsymbol{u}$ where $\boldsymbol{u}_{(i)}^{t+\Delta t}$ is the nodal displacement vector at iteration i, the internal nodal force vector $\boldsymbol{f}_{int}^{t+\Delta t}$ is expanded as

$$\boldsymbol{f}_{int}^{t+\Delta t}(\boldsymbol{u}^{t+\Delta t}) \approx \boldsymbol{f}_{int}^{t+\Delta t}(\boldsymbol{u}_{(i)}^{t+\Delta t}) + \left.\frac{\partial \boldsymbol{f}_{int}^{t+\Delta t}(\boldsymbol{u})}{\partial \boldsymbol{u}}\right|_{(i)} \Delta \boldsymbol{u} \tag{3.6}$$

Substituting the above equation into Eq.(3.5),

$$\left.\frac{\partial \boldsymbol{f}_{int}^{t+\Delta t}(\boldsymbol{u})}{\partial \boldsymbol{u}}\right|_{(i)} \Delta \boldsymbol{u} = \boldsymbol{f}_{ext}^{t+\Delta t} - \boldsymbol{f}_{int}^{t+\Delta t}(\boldsymbol{u}_{(i)}^{t+\Delta t}) \tag{3.7}$$

Let $\boldsymbol{K}_{(i)} = \left.\frac{\partial \boldsymbol{f}_{int}^{t+\Delta t}(\boldsymbol{u})}{\partial \boldsymbol{u}}\right|_{(i)}$, which is the tangential stiffness matrix at iteration i.

Hence, Eq.(3.7) is written as

$$\boldsymbol{K}_{(i)} \Delta \boldsymbol{u} = \boldsymbol{f}_{ext}^{t+\Delta t} - \boldsymbol{f}_{int}^{t+\Delta t}(\boldsymbol{u}_{(i)}^{t+\Delta t}) = \boldsymbol{f}_{res} \tag{3.8}$$

where $\boldsymbol{f}_{ext}^{t+\Delta t} - \boldsymbol{f}_{int}^{t+\Delta t}(\boldsymbol{u}_{(i)}^{t+\Delta t})$ is the residual force vector, denoted as $\boldsymbol{f}_{res}$.

Solving the linear system defined by Eq.(3.8) to obtain $\Delta \boldsymbol{u}$, which is then used to update the nodal displacement vector at iteration i+1 $\boldsymbol{u}_{(i+1)}^{t+\Delta t}$, i.e.

$$\boldsymbol{u}_{(i+1)}^{t+\Delta t} = \boldsymbol{u}_{(i)}^{t+\Delta t} + \Delta \boldsymbol{u} \tag{3.9}$$

The above iterative process continues until the norm of $\boldsymbol{f}_{res}$ is smaller than a predefined convergence tolerance. The L^2-norm of $\boldsymbol{f}_{res}$ is employed in the current study.

3.2.2 Nonlinear finite element equations

In the case of finite deformation, it must be ensured the that stress and strain measures employed to formulate the nonlinear finite element equations are work conjugate pairs [54, 56]. In the present study, the second Piola-Kirchhoff stress tensor S_{ij} and the Green-Lagrange strain tensor ε_{ij} are taken to be the stress and strain measures, respectively. As the basis for deriving the displacement based finite element formulation, the principle of virtual displacement established in the current (unknown) configuration is written as

$$\int_{V_0} S_{ij}{}^{t+\Delta t} \delta \varepsilon_{ij}{}^{t+\Delta t} dV_0 = R^{t+\Delta t} \tag{3.10}$$

The superscript $t+\Delta t$ represents the configuration in which the quantity (stress, strain, body force, surface traction, etc.) occurs, i.e. $S_{ij}{}^{t+\Delta t}$ and $\varepsilon_{ij}{}^{t+\Delta t}$ denote second Piola-Kirchhoff stress and Green strain measured at the unknown configuration corresponding to load level at $t+\Delta t$; $R^{t+\Delta t}$ is the virtual external work induced by the virtual displacement applied at the unknown configuration at load level $t+\Delta t$.

The first step to derive the linearized finite element formulation is to write the principle of virtual displacement at $t+\Delta t$ (Eq.(3.10)) as an incremental decomposition, i.e. to express the virtual internal work (left hand side of Eq.(3.10)) by use of known quantities at t and associated increments from t to $t+\Delta t$.

$$S_{ij}{}^{t+\Delta t} = S_{ij}{}^{t} + \Delta S_{ij} \tag{3.11a}$$

$$\varepsilon_{ij}{}^{t+\Delta t} = \varepsilon_{ij}{}^{t} + \Delta \varepsilon_{ij} \tag{3.11b}$$

where ΔS_{ij} and $\Delta \varepsilon_{ij}$ are incremental stress and strain from load level t to $t+\Delta t$;

By definition of Green strain [57],

$$\varepsilon_{ij}{}^{t+\Delta t} = \frac{1}{2}(u_{i,j}{}^{t+\Delta t} + u_{j,i}{}^{t+\Delta t} + u_{k,i}{}^{t+\Delta t} u_{k,j}{}^{t+\Delta t}) \quad i, j = 1, 2, 3 \tag{3.12a}$$

$$\varepsilon_{ij}{}^{t} = \frac{1}{2}(u_{i,j}{}^{t} + u_{j,i}{}^{t} + u_{k,i}{}^{t}u_{k,j}{}^{t}) \quad i,j = 1,2,3 \tag{3.12b}$$

where $u_{i,j}$ is the derivative of the i^{th} component of displacement with respect to the j^{th} component of spatial coordinates. Subtracting Eq.(3.12b) from Eq.(3.12a) and using $\Delta u_i = u_i^{t+\Delta t} - u_i^t, i = 1,2,3$, the incremental Green's strain $\Delta\varepsilon_{ij}$ is obtained as

$$\Delta\varepsilon_{ij} = \varepsilon_{ij}{}^{t+\Delta t} - \varepsilon_{ij}{}^{t} = \frac{1}{2}(\Delta u_{i,j} + \Delta u_{j,i} + u_{k,i}{}^{t}\Delta u_{k,j} + u_{k,j}{}^{t}\Delta u_{k,i}) + \frac{1}{2}\Delta u_{k,i}\Delta u_{k,j} \tag{3.13}$$

Further decomposing the incremental Green's strain $\Delta\varepsilon_{ij}$ into two terms, Δe_{ij} and $\Delta\eta_{ij}$,

$$\Delta\varepsilon_{ij} = \Delta e_{ij} + \Delta\eta_{ij} \tag{3.14a}$$

$$\Delta e_{ij} = \frac{1}{2}(\Delta u_{i,j} + \Delta u_{j,i} + u_{k,i}{}^{t}\Delta u_{k,j} + u_{k,j}{}^{t}\Delta u_{k,i}) \tag{3.14b}$$

$$\Delta\eta_{ij} = \frac{1}{2}\Delta u_{k,i}\Delta u_{k,j} \tag{3.14c}$$

in which Δe_{ij} is linear with Δu_i (note that $u_{k,i}{}^{t}$ is a known quantity) and $\Delta\eta_{ij}$ is nonlinear with Δu_i. It is shown in the next section that these two terms contribute to the linear and nonlinear part of tangential stiffness matrix, respectively.

Substituting the above incremental forms of stress and strain (Eq.3.11, 3.14) into Eq.(3.10) and noting that $\delta\varepsilon_{ij}{}^{t+\Delta t} = \delta(\varepsilon_{ij}{}^{t} + \Delta\varepsilon_{ij}) = \delta\Delta\varepsilon_{ij}$, the principle of virtual displacement with incremental decomposition is obtained

$$\int_{V_0} \Delta S_{ij}\delta\Delta\varepsilon_{ij}dV_0 + \int_{V_0} S_{ij}{}^{t}\delta\Delta\eta_{ij}dV_0 = R^{t+\Delta t} - \int_{V_0} S_{ij}{}^{t}\delta\Delta e_{ij}dV_0 \tag{3.15}$$

Linearizing the first term on the left hand side using a Taylor series,

$$\int_{V_0} \Delta S_{ij}\delta\Delta\varepsilon_{ij}dV_0 = \int_{V_0} \left(\frac{\partial S_{ij}}{\partial\varepsilon_{rs}}\bigg|_t \Delta\varepsilon_{rs} + \text{h.o.t.}\right)\delta(\Delta e_{ij} + \Delta\eta_{ij})dV_0 \tag{3.16a}$$

Neglecting higher order terms (h.o.t) in the Taylor series and using $\Delta\varepsilon_{rs} = \Delta e_{rs} + \Delta\eta_{rs}$, Eq.(3.16a) becomes

$$\int_{V_0} \Delta S_{ij}\delta\Delta\varepsilon_{ij}dV_0 = \int_{V_0} \left.\frac{\partial S_{ij}}{\partial \varepsilon_{rs}}\right|_t (\Delta e_{rs} + \Delta\eta_{rs})\delta(\Delta e_{ij} + \Delta\eta_{ij})dV_0$$
$$= \int_{V_0} \left.\frac{\partial S_{ij}}{\partial \varepsilon_{rs}}\right|_t (\Delta e_{rs}\delta\Delta e_{ij} + \Delta e_{rs}\delta\Delta\eta_{ij} + \Delta\eta_{rs}\delta\Delta e_{ij} + \Delta\eta_{rs}\delta\Delta\eta_{ij}) \tag{3.16b}$$

Noting that $\delta\Delta\eta_{ij} = \frac{1}{2}(\Delta u_{k,i}\delta\Delta u_{k,j} + \Delta u_{k,j}\delta\Delta u_{k,i})$ and $\Delta\eta_{ij} = \frac{1}{2}\Delta u_{k,i}\Delta u_{k,j}$, hence, among the four terms in the bracket in Eq. (3.16b), only the first term $\Delta e_{rs}\delta\Delta e_{ij}$ is linear with incremental displacement Δu_i and the left three terms are higher order terms which are neglected. Eq. (3.16b) becomes

$$\int_{V_0} \Delta S_{ij}\delta\Delta\varepsilon_{ij}dV_0 = \int_{V_0} \left.\frac{\partial S_{ij}}{\partial \varepsilon_{rs}}\right|_t \Delta e_{rs}\delta\Delta e_{ij}dV_0 = \int_{V_0} C_{ijrs}\Delta e_{rs}\delta\Delta e_{ij}dV_0 \tag{3.17}$$

where

$C_{ijrs} = \left.\frac{\partial S_{ij}}{\partial \varepsilon_{rs}}\right|_t$ is the fourth order material tangent elasticity tensor evaluated at known configuration corresponding to load step at *t*.

Substituting Eq.(3.17) into Eq.(3.15), the following equation is constructed

$$\int_{V_0} C_{ijrs}\Delta e_{rs}\delta\Delta e_{ij}dV_0 + \int_{V_0} S_{ij}{}^t\delta\Delta\eta_{ij}dV_0 = R^{t+\Delta t} - \int_{V_0} S_{ij}{}^t\delta\Delta e_{ij}dV_0 \tag{3.18}$$

which is the principle of virtual displacements after linearization. From Eq. (3.18), the linear tangent matrix stiffness $\boldsymbol{K}_L$, nonlinear tangent matrix stiffness $\boldsymbol{K}_{NL}$ are derived.

To make Eq.(3.18) more compact, each term in the equation can be case in a matrix format

$$\int_{V_0} C_{ijrs}\Delta e_{rs}\delta\Delta e_{ij}dV_0 = \int_{V_0} \delta\Delta\tilde{\boldsymbol{e}}^T\hat{\boldsymbol{C}}\Delta\tilde{\boldsymbol{e}}dV_0 = \delta\Delta\boldsymbol{u}^T(\int_{V_0} \boldsymbol{B}_L{}^T\hat{\boldsymbol{C}}\boldsymbol{B}_L dV_0)\Delta\boldsymbol{u} \tag{3.19a}$$

$$\int_{V_0} S_{ij}{}^t\delta\Delta\eta_{ij}dV_0 = \int_{V_0} \delta\Delta\tilde{\boldsymbol{\eta}}^T\tilde{\boldsymbol{S}}^t\Delta\tilde{\boldsymbol{\eta}}dV_0 = \delta\Delta\boldsymbol{u}^T(\int_{V_0} \boldsymbol{B}_{NL}{}^T\tilde{\boldsymbol{S}}^t\boldsymbol{B}_{NL}dV_0)\Delta\boldsymbol{u} \tag{3.19b}$$

$$\int_{V_0} S_{ij}{}^t\delta\Delta e_{ij}dV_0 = \int_{V_0} \delta\Delta\tilde{\boldsymbol{e}}^T\hat{\boldsymbol{S}}^t dV_0 = \delta\Delta\boldsymbol{u}^T(\int_{V_0} \boldsymbol{B}_L{}^T\hat{\boldsymbol{S}}^t dV_0) \tag{3.19c}$$

$$\int_{V_0} \delta\Delta\tilde{\boldsymbol{e}}^T \hat{\boldsymbol{C}} \Delta\tilde{\boldsymbol{e}} dV_0 + \int_{V_0} \delta\Delta\tilde{\boldsymbol{\eta}}^T \tilde{\boldsymbol{S}}^t \Delta\tilde{\boldsymbol{\eta}} dV_0 = R^{t+\Delta t} - \int_{V_0} \delta\Delta\tilde{\boldsymbol{e}}^T \hat{\boldsymbol{S}}^t dV_0 \tag{3.19d}$$

where

$$\Delta\tilde{\boldsymbol{e}} = [\Delta e_{11} \quad \Delta e_{22} \quad \Delta e_{33} \quad 2\Delta e_{12} \quad 2\Delta e_{23} \quad 2\Delta e_{31}]^T$$

$$\Delta\tilde{\boldsymbol{\eta}} = \begin{bmatrix} \Delta u_{1,1} & \Delta u_{1,2} & \Delta u_{1,3} & \Delta u_{2,1} & \Delta u_{2,2} & \Delta u_{2,3} & \Delta u_{3,1} & \Delta u_{3,2} & \Delta u_{3,3} \end{bmatrix}^T$$

$$\hat{\boldsymbol{C}} = \begin{bmatrix} C_{1111} & C_{1122} & C_{1133} & C_{1112} & C_{1123} & C_{1131} \\ C_{2211} & C_{2222} & C_{2233} & C_{2212} & C_{2223} & C_{2231} \\ C_{3311} & C_{3322} & C_{3333} & C_{3312} & C_{3323} & C_{3331} \\ C_{1211} & C_{1222} & C_{1233} & C_{1212} & C_{1223} & C_{1231} \\ C_{2311} & C_{2322} & C_{2333} & C_{2333} & C_{2323} & C_{2323} \\ C_{3111} & C_{3122} & C_{3133} & C_{3133} & C_{3123} & C_{3123} \end{bmatrix},$$

$$\tilde{\boldsymbol{S}}^t = \begin{bmatrix} \boldsymbol{S} & \tilde{\boldsymbol{0}} & \tilde{\boldsymbol{0}} \\ \tilde{\boldsymbol{0}} & \boldsymbol{S} & \tilde{\boldsymbol{0}} \\ \tilde{\boldsymbol{0}} & \tilde{\boldsymbol{0}} & \boldsymbol{S} \end{bmatrix}, \boldsymbol{S} = \begin{bmatrix} S_{11}{}^t & S_{12}{}^t & S_{13}{}^t \\ S_{12}{}^t & S_{22}{}^t & S_{23}{}^t \\ S_{13}{}^t & S_{23}{}^t & S_{33}{}^t \end{bmatrix}, \tilde{\boldsymbol{0}} = \begin{bmatrix} 0 & 0 & 0 \\ 0 & 0 & 0 \\ 0 & 0 & 0 \end{bmatrix}$$

$$\hat{\boldsymbol{S}}^t = \begin{bmatrix} S_{11}{}^t & S_{22}{}^t & S_{33}{}^t & S_{12}{}^t & S_{23}{}^t & S_{13}{}^t \end{bmatrix}^T$$

By interpolating the displacement field with appropriate shape functions, the incremental strain vectors $\Delta\tilde{\boldsymbol{e}}$ and $\Delta\tilde{\boldsymbol{\eta}}$ are related to nodal displacement vector $\Delta\boldsymbol{u}$ by $\Delta\tilde{\boldsymbol{e}} = \boldsymbol{B}_L \Delta\boldsymbol{u}$ and $\Delta\tilde{\boldsymbol{\eta}} = \boldsymbol{B}_{NL} \Delta\boldsymbol{u}$, where $\boldsymbol{B}_L$ and $\boldsymbol{B}_{NL}$ are correspondingly linear and nonlinear strain-displacement matrix respectively. Hence, Eq.(3.19d) is written as

$$\begin{aligned} &\delta\Delta\boldsymbol{u}^T \left(\int_{V_0} \boldsymbol{B}_L{}^T \hat{\boldsymbol{C}} \boldsymbol{B}_L dV_0\right) \Delta\boldsymbol{u} + \delta\Delta\boldsymbol{u}^T \left(\int_{V_0} \boldsymbol{B}_{NL}{}^T \tilde{\boldsymbol{S}}^t \boldsymbol{B}_{NL} dV_0\right) \Delta\boldsymbol{u} \\ &= R^{t+\Delta t} - \delta\Delta\boldsymbol{u}^T \left(\int_{V_0} \boldsymbol{B}_L{}^T \hat{\boldsymbol{S}}^t dV_0\right) \end{aligned} \tag{3.20}$$

Assuming there is no external force ($R^{t+\Delta t} = 0$),

$$\begin{aligned} &\delta\Delta\boldsymbol{u}^T \left(\int_{V_0} \boldsymbol{B}_L{}^T \hat{\boldsymbol{C}} \boldsymbol{B}_L dV_0\right) \Delta\boldsymbol{u} + \delta\Delta\boldsymbol{u}^T \left(\int_{V_0} \boldsymbol{B}_{NL}{}^T \tilde{\boldsymbol{S}}^t \boldsymbol{B}_{NL} dV_0\right) \Delta\boldsymbol{u} \\ &= -\delta\Delta\boldsymbol{u}^T \left(\int_{V_0} \boldsymbol{B}_L{}^T \hat{\boldsymbol{S}}^t dV_0\right) \end{aligned} \tag{3.21}$$

The above equation is valid for arbitrary virtual incremental displacement $\delta\Delta\boldsymbol{u}$, by eliminating $\delta\Delta\boldsymbol{u}$

$$\int_{V_0} \boldsymbol{B}_L{}^T \hat{\boldsymbol{C}} \boldsymbol{B}_L dV_0 \Delta\boldsymbol{u} + \int_{V_0} \boldsymbol{B}_{NL}{}^T \tilde{\boldsymbol{S}}^t \boldsymbol{B}_{NL} dV_0 \Delta\boldsymbol{u} = -\int_{V_0} \boldsymbol{B}_L{}^T \hat{\boldsymbol{S}}^t dV_0 \tag{3.22}$$

Let

$$\boldsymbol{K}_L = \int_{V_0} \boldsymbol{B}_L{}^T \boldsymbol{C} \boldsymbol{B}_L dV_0 \tag{3.23a}$$

$$\boldsymbol{K}_{NL} = \int_{V_0} \boldsymbol{B}_{NL}{}^T \tilde{\boldsymbol{S}}^t \boldsymbol{B}_{NL} dV \tag{3.23b}$$

$$\boldsymbol{f} = \int_{V_0} \boldsymbol{B}_L{}^T \hat{\boldsymbol{S}}^t dV_0 \tag{3.23c}$$

Therefore

$$(\boldsymbol{K}_L + \boldsymbol{K}_{NL})\Delta \boldsymbol{u} = -\boldsymbol{f} \tag{3.24}$$

3.2.3 Strain-displacement relationship for three dimensional matrix elements

This section derives the linear and nonlinear strain-displacement matrices $\boldsymbol{B_L}$ and $\boldsymbol{B_{NL}}$ by interpolating the displacement field using shape functions.

The displacement field of the linear tetrahedral element representing matrix material is interpolated by linear shape functions $\boldsymbol{N}^T = \begin{bmatrix} N_1 & N_2 & N_3 & N_4 \end{bmatrix}$, i.e.

$$u_i = \sum_{k=1}^{4} N_k u_i^k \text{ , } i\text{=1,2,3} \tag{3.25}$$

where u_i^k is the ith component of displacement vector at node k.

(1) Linear strain-displacement matrix $\boldsymbol{B}_L$ ($\Delta \tilde{\boldsymbol{e}} = \boldsymbol{B}_L \Delta \boldsymbol{u}$)

Recall

$$\Delta \tilde{\boldsymbol{e}} = [\Delta e_{11} \quad \Delta e_{22} \quad \Delta e_{33} \quad 2\Delta e_{12} \quad 2\Delta e_{23} \quad 2\Delta e_{31}]^T$$

$$\Delta e_{ij} = \frac{1}{2}(\Delta u_{i,j} + \Delta u_{j,i} + u_{k,i}{}^t \Delta u_{k,j} + u_{k,j}{}^t \Delta u_{k,i}), i, j, k = 1, 2, 3$$

and write

$$\Delta \tilde{\boldsymbol{e}} = \Delta \tilde{\boldsymbol{e}}^0 + \Delta \tilde{\boldsymbol{e}}^1, \boldsymbol{B}_L = \boldsymbol{B}_{L0} + \boldsymbol{B}_{L1} \tag{3.26a}$$

$$\Delta \tilde{\boldsymbol{e}}^0 = \boldsymbol{B}_{L0} \Delta \boldsymbol{u}, \Delta \tilde{\boldsymbol{e}}^1 = \boldsymbol{B}_{L1} \Delta \boldsymbol{u} \tag{3.26b}$$

where $\Delta \tilde{\boldsymbol{e}}^0 = [\Delta e_{11}{}^0 \quad \Delta e_{22}{}^0 \quad \Delta e_{33}{}^0 \quad 2\Delta e_{12}{}^0 \quad 2\Delta e_{23}{}^0 \quad 2\Delta e_{31}{}^0]^T$

$\Delta \tilde{\boldsymbol{e}}^1 = [\Delta e_{11}{}^1 \quad \Delta e_{22}{}^1 \quad \Delta e_{33}{}^1 \quad 2\Delta e_{12}{}^1 \quad 2\Delta e_{23}{}^1 \quad 2\Delta e_{31}{}^1]^T$

$$\Delta \boldsymbol{u} = \begin{bmatrix} \Delta u_1^1 & \Delta u_2^1 & \Delta u_3^1 & \Delta u_1^2 & \dots & \Delta u_3^4 \end{bmatrix}^T$$

with $\Delta e_{ij}^{\ 0} = \frac{1}{2}(\Delta u_{i,j} + \Delta u_{j,i})$ and $\Delta e_{ij}^{\ 1} = \frac{1}{2}(u_{k,i}^{\ t} \Delta u_{k,j} + u_{k,j}^{\ t} \Delta u_{k,i})$

Hence,

$$B_{L0} = \begin{bmatrix} N_{1,1} & 0 & 0 & N_{2,1} & 0 & 0 & N_{3,1} & 0 & 0 & N_{4,1} & 0 & 0 \\ 0 & N_{1,2} & 0 & 0 & N_{2,2} & 0 & 0 & N_{3,2} & 0 & 0 & N_{4,2} & 0 \\ 0 & 0 & N_{1,3} & 0 & 0 & N_{2,3} & 0 & 0 & N_{3,3} & 0 & 0 & N_{4,3} \\ N_{1,2} & N_{1,1} & 0 & N_{2,2} & N_{2,1} & 0 & N_{3,2} & N_{3,1} & 0 & N_{4,2} & N_{4,1} & 0 \\ 0 & N_{1,3} & N_{1,2} & 0 & N_{2,3} & N_{2,2} & 0 & N_{3,3} & N_{3,2} & 0 & N_{4,3} & N_{4,2} \\ N_{1,3} & 0 & N_{1,1} & N_{2,3} & 0 & N_{2,1} & N_{3,3} & 0 & N_{3,1} & N_{4,3} & 0 & N_{4,1} \end{bmatrix} \tag{3.27a}$$

where $N_{i,j}$ is the derivative of shape function at node i with respect to the jth component of spatial coordinates.

$$B_{L1} = \begin{bmatrix} l_{11}N_{1,1} & l_{21}N_{1,1} & l_{31}N_{1,1} & l_{11}N_{2,1} & \dots & l_{31}N_{4,1} \\ l_{12}N_{1,2} & l_{22}N_{1,2} & l_{32}N_{1,2} & l_{12}N_{2,2} & \dots & l_{32}N_{4,2} \\ l_{13}N_{1,3} & l_{23}N_{1,3} & l_{33}N_{1,3} & l_{13}N_{2,3} & \dots & l_{33}N_{4,3} \\ l_{11}N_{1,2} + l_{12}N_{1,1} & l_{21}N_{1,2} + l_{22}N_{1,1} & l_{31}N_{1,2} + l_{32}N_{1,1} & l_{11}N_{2,2} + l_{12}N_{2,1} & \dots & l_{31}N_{4,2} + l_{32}N_{4,1} \\ l_{12}N_{1,3} + l_{13}N_{1,2} & l_{22}N_{1,3} + l_{23}N_{1,2} & l_{32}N_{1,3} + l_{33}N_{1,2} & l_{12}N_{2,3} + l_{13}N_{2,2} & \dots & l_{32}N_{4,3} + l_{33}N_{4,2} \\ l_{11}N_{1,3} + l_{13}N_{1,1} & l_{21}N_{1,3} + l_{23}N_{1,1} & l_{31}N_{1,3} + l_{33}N_{1,1} & l_{11}N_{2,3} + l_{13}N_{2,1} & \dots & l_{31}N_{4,3} + l_{33}N_{4,1} \end{bmatrix}$$

$$l_{ij} = \sum_{k=1}^{4} N_{k,j} u_i^k \quad i, j = 1, 2, 3$$

(3.27b)

(2) Nonlinear strain-displacement matrix $\boldsymbol{B}_{NL}$ ($\Delta \tilde{\boldsymbol{\eta}} = \boldsymbol{B}_{NL} \Delta \boldsymbol{u}$)

Recall that $\Delta \tilde{\boldsymbol{\eta}} = \begin{bmatrix} \Delta u_{1,1} & \Delta u_{1,2} & \Delta u_{1,3} & \Delta u_{2,1} & \Delta u_{2,2} & \Delta u_{2,3} & \Delta u_{3,1} & \Delta u_{3,2} & \Delta u_{3,3} \end{bmatrix}^T$

It is straightforward to construct

$$\boldsymbol{B}_{NL} = \begin{bmatrix} \tilde{\boldsymbol{B}}_{\boldsymbol{NL}} & \tilde{\boldsymbol{0}} & \tilde{\boldsymbol{0}} \\ \tilde{\boldsymbol{0}} & \tilde{\boldsymbol{B}}_{\boldsymbol{NL}} & \tilde{\boldsymbol{0}} \\ \tilde{\boldsymbol{0}} & \tilde{\boldsymbol{0}} & \tilde{\boldsymbol{B}}_{\boldsymbol{NL}} \end{bmatrix}, \tilde{\boldsymbol{0}} = \begin{bmatrix} 0 \\ 0 \\ 0 \end{bmatrix} \tag{3.28a}$$

$$\tilde{\boldsymbol{B}}_{\boldsymbol{NL}} = \begin{bmatrix} N_{1,1} & 0 & 0 & N_{2,1} & 0 & 0 & N_{3,1} & 0 & 0 & N_{4,1} \\ N_{1,2} & 0 & 0 & N_{2,2} & 0 & 0 & N_{3,2} & 0 & 0 & N_{4,2} \\ N_{1,3} & 0 & 0 & N_{2,3} & 0 & 0 & N_{3,2} & 0 & 0 & N_{4,3} \end{bmatrix} \tag{3.28b}$$

3.2.4 Nonlinear finite element formulation for one dimensional truss element

The nonlinear equations for one dimensional truss elements (Figure 3.1) are derived in a more straightforward manner since the expression of nodal forces at two ends of the truss element can be easily obtained by projecting axial force along the spatial axis. The element tangent stiffness matrix $\boldsymbol{K}^{TR}$ is obtained by direct differentiation of the element nodal force vector $\boldsymbol{f}$ with respect the nodal displacement vector $\boldsymbol{u}$ [54], i.e.

$$\boldsymbol{K}^{TR} = \frac{\partial \boldsymbol{f}}{\partial \boldsymbol{u}} \tag{3.29}$$

where $\boldsymbol{K}^{TR} = \begin{bmatrix} \frac{\partial f_1^1}{\partial u_1^1} & \frac{\partial f_1^1}{\partial u_2^1} & \frac{\partial f_1^1}{\partial u_3^1} & \frac{\partial f_1^1}{\partial u_1^2} & \frac{\partial f_1^1}{\partial u_2^2} & \frac{\partial f_1^1}{\partial u_3^2} \\ \frac{\partial f_2^1}{\partial u_1^1} & \frac{\partial f_2^1}{\partial u_2^1} & \frac{\partial f_2^1}{\partial u_3^1} & \frac{\partial f_2^1}{\partial u_1^2} & \frac{\partial f_2^1}{\partial u_2^2} & \frac{\partial f_2^1}{\partial u_3^2} \\ \frac{\partial f_3^1}{\partial u_1^1} & \frac{\partial f_3^1}{\partial u_2^1} & \frac{\partial f_3^1}{\partial u_3^1} & \frac{\partial f_3^1}{\partial u_1^2} & \frac{\partial f_3^1}{\partial u_2^2} & \frac{\partial f_3^1}{\partial u_3^2} \\ \frac{\partial f_1^2}{\partial u_1^1} & \frac{\partial f_1^2}{\partial u_2^1} & \frac{\partial f_1^2}{\partial u_3^1} & \frac{\partial f_1^2}{\partial u_1^2} & \frac{\partial f_1^2}{\partial u_2^2} & \frac{\partial f_1^2}{\partial u_3^2} \\ \frac{\partial f_2^2}{\partial u_1^1} & \frac{\partial f_2^2}{\partial u_2^1} & \frac{\partial f_2^2}{\partial u_3^1} & \frac{\partial f_2^2}{\partial u_1^2} & \frac{\partial f_2^2}{\partial u_2^2} & \frac{\partial f_2^2}{\partial u_3^2} \\ \frac{\partial f_3^2}{\partial u_1^1} & \frac{\partial f_3^2}{\partial u_2^1} & \frac{\partial f_3^2}{\partial u_3^1} & \frac{\partial f_3^2}{\partial u_1^2} & \frac{\partial f_3^2}{\partial u_2^2} & \frac{\partial f_3^2}{\partial u_3^2} \end{bmatrix}$

element nodal force vector $\boldsymbol{f}$

$$\boldsymbol{f} = \begin{bmatrix} f_1^1 & f_2^1 & f_3^1 & f_1^2 & f_2^2 & f_3^2 \end{bmatrix}^T \tag{3.30}$$

$$\boldsymbol{u} = \begin{bmatrix} u_1^1 & u_2^1 & u_3^1 & u_1^2 & u_2^2 & u_3^2 \end{bmatrix}^T \tag{3.31}$$

where f_i^j is the i^{th} component of nodal force vector at node j and u_i^j is the i^{th} component of displacement vector at node j.

By projecting the fiber axial force f^{fib} along spatial axis, the element nodal force vector $\boldsymbol{f}$ is written as

$$\boldsymbol{f} = f^{fib}\left[\frac{x_1^1 - x_1^2}{l} \quad \frac{x_2^1 - x_2^2}{l} \quad \frac{x_3^1 - x_3^2}{l} \quad \frac{x_1^2 - x_1^1}{l} \quad \frac{x_2^2 - x_2^1}{l} \quad \frac{x_3^2 - x_3^1}{l}\right]^T \tag{3.32}$$

where l is the length of the truss element in current configuration and x_i^j is the i^{th} component of position vector at node j.

Since $\boldsymbol{x} = \boldsymbol{x}_0 + \boldsymbol{u}$, $\boldsymbol{x}$ and $\boldsymbol{x}_0$ are nodal position vectors in current and initial configuration respectively,

$$\boldsymbol{x} = \begin{bmatrix} x_1^1 & x_2^1 & x_3^1 & x_1^2 & x_2^2 & x_3^2 \end{bmatrix}^T$$

$$\boldsymbol{x}_0 = \begin{bmatrix} x_{01}^1 & x_{02}^1 & x_{03}^1 & x_{01}^2 & x_{02}^2 & x_{03}^2 \end{bmatrix}^T$$

Eq.(3.29) is becomes

$$\boldsymbol{K}^{TR} = \frac{\partial \boldsymbol{f}}{\partial \boldsymbol{u}} = \frac{\partial \boldsymbol{f}}{\partial \boldsymbol{x}} \tag{3.33}$$

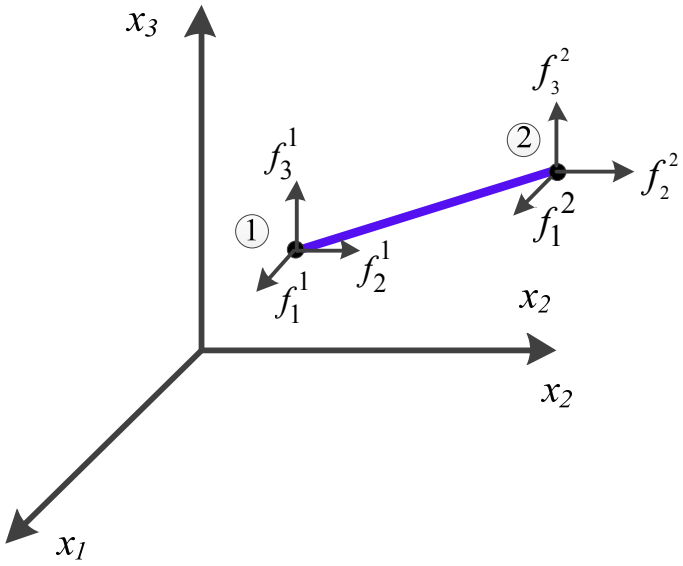

Figure 3.1: Illustration of a linear truss element.

Take the derivation of the first entry of tangent stiffness matrix $\frac{\partial f_1^1}{\partial x_1^1}$ as an example.

By projecting axial force along x_1, nodal force at node 1 along x_1 direction is

$$f_1^1 = f^{fib} \frac{x_1^1 - x_1^2}{l} \tag{3.34}$$

in which fiber axis force f^{fib} and the current fiber length l are functions of current nodal coordinates.

Using the chain rule,

$$\frac{\partial f_1^1}{\partial x_1^1} = \frac{\partial f_1^1}{\partial f^{fib}} \frac{\partial f^{fib}}{\partial l} \frac{\partial l}{\partial x_1^1} + \frac{\partial f_1^1}{\partial l} \frac{\partial l}{\partial x_1^1} + \frac{f^{fib}}{l} \tag{3.35}$$

The first two terms of the right hand side of Eq.(3.35) are written as:

$$\frac{\partial f_1^1}{\partial f^{fib}} \frac{\partial f^{fib}}{\partial l} \frac{\partial l}{\partial x_1^1} = \left(\frac{x_1^1 - x_1^2}{l} \right)^2 \frac{\partial f^{fib}}{\partial l} \tag{3.36}$$

$$\frac{\partial f_1^1}{\partial l} \frac{\partial l}{\partial x_1^1} = -\frac{f^{fib}}{l} \left(\frac{x_1^1 - x_1^2}{l} \right)^2 \tag{3.37}$$

Hence,

$$\frac{\partial f_1^1}{\partial x_1^1} = \left(\frac{\partial f^{fib}}{\partial l} - \frac{f^{fib}}{l} \right) \left(\frac{x_1^1 - x_1^2}{l} \right)^2 + \frac{f^{fib}}{l} \tag{3.38a}$$

Similarly,

$$\frac{\partial f_1^1}{\partial x_2^1} = \left(\frac{\partial f^{fib}}{\partial l} - \frac{f^{fib}}{l} \right) \frac{x_1^1 - x_1^2}{l} \frac{x_2^1 - x_2^2}{l} \tag{3.38b}$$

$$\frac{\partial f_1^1}{\partial x_3^1} = \left(\frac{\partial f^{fib}}{\partial l} - \frac{f^{fib}}{l} \right) \frac{x_1^1 - x_1^2}{l} \frac{x_3^1 - x_3^2}{l} \tag{3.38c}$$

$$\frac{\partial f_1^1}{\partial x_1^2} = -\frac{\partial f_1^1}{\partial x_1^1}, \frac{\partial f_1^1}{\partial x_2^2} = -\frac{\partial f_1^1}{\partial x_2^1}, \frac{\partial f_1^1}{\partial x_3^2} = -\frac{\partial f_1^1}{\partial x_3^1} \tag{3.38d}$$

$$\frac{\partial f_2^1}{\partial x_1^1} = \left(\frac{\partial f^{fib}}{\partial l} - \frac{f^{fib}}{l} \right) \frac{x_1^1 - x_1^2}{l} \frac{x_2^1 - x_2^2}{l} = \frac{\partial f_1^1}{\partial x_2^1} \tag{3.38e}$$

$$\frac{\partial f_2^1}{\partial x_2^1} = \left(\frac{\partial f^{fib}}{\partial l} - \frac{f^{fib}}{l} \right) \left(\frac{x_2^1 - x_2^2}{l} \right)^2 + \frac{f^{fib}}{l} \tag{3.38f}$$

$$\frac{\partial f_2^1}{\partial x_3^1} = \left(\frac{\partial f^{fib}}{\partial l} - \frac{f^{fib}}{l} \right) \left(\frac{x_2^1 - x_2^2}{l} \right) \left(\frac{x_3^1 - x_3^2}{l} \right) \tag{3.38g}$$

$$\frac{\partial f_2^1}{\partial x_1^2} = -\frac{\partial f_2^1}{\partial x_1^1}, \frac{\partial f_2^1}{\partial x_2^2} = -\frac{\partial f_2^1}{\partial x_2^1}, \frac{\partial f_2^1}{\partial x_3^2} = -\frac{\partial f_2^1}{\partial x_3^1} \tag{3.38h}$$

$$\frac{\partial f_3^1}{\partial x_1^1} = \left(\frac{\partial f^{fib}}{\partial l} - \frac{f^{fib}}{l} \right) \left(\frac{x_1^1 - x_1^2}{l} \right) \left(\frac{x_3^1 - x_3^2}{l} \right) = \frac{\partial f_1^1}{\partial x_3^1} \tag{3.38i}$$

$$\frac{\partial f_3^1}{\partial x_2^1} = \left(\frac{\partial f^{fib}}{\partial l} - \frac{f^{fib}}{l}\right)\left(\frac{x_2^1 - x_2^2}{l}\right)\left(\frac{x_3^1 - x_3^2}{l}\right) = \frac{\partial f_2^1}{\partial x_3^1} \tag{3.38j}$$

$$\frac{\partial f_3^1}{\partial x_3^1} = \left(\frac{\partial f^{fib}}{\partial l} - \frac{f^{fib}}{l}\right)\left(\frac{x_3^1 - x_3^2}{l}\right)^2 + \frac{f^{fib}}{l} \tag{3.38k}$$

$$\frac{\partial f_3^1}{\partial x_1^2} = -\frac{\partial f_3^1}{\partial x_1^1}, \frac{\partial f_3^1}{\partial x_2^2} = -\frac{\partial f_3^1}{\partial x_2^1}, \frac{\partial f_3^1}{\partial x_3^2} = -\frac{\partial f_3^1}{\partial x_3^1} \tag{3.38l}$$

…

Element nodal force vector is

$$\boldsymbol{f} = f^{fib}\left[\frac{x_1^1 - x_1^2}{l} \quad \frac{x_2^1 - x_2^2}{l} \quad \frac{x_3^1 - x_3^2}{l} \quad \frac{x_1^2 - x_1^1}{l} \quad \frac{x_2^2 - x_2^1}{l} \quad \frac{x_3^2 - x_3^1}{l}\right]^T \tag{3.39}$$

3.3 Matrix and vector assembling of coupled linear tetrahedron and truss

As indicated in Chapter 2, the multi-dimensional mesh is generated such that fibers discretized into mesh edges and matrix material discretized into mesh regions share the same mesh vertices along fibers. Figure 3.2 shows a representative picture of the coupled two dimensional types of mesh elements. Mesh vertices 2 and 3 are shared by adjacent tetrahedron and truss members.

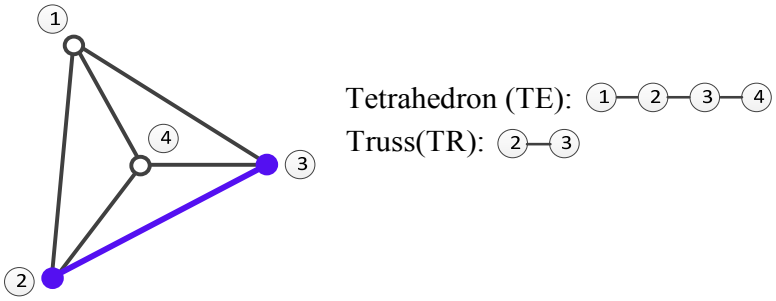

Figure 3.2: A representative example of the coupled tetrahedron and truss members.

Each node is associated with three degree of freedom representing nodal displacement variables. Table 3.1 shows numbering of degree of freedoms with respect to each node.

Table 3.1: Numbering of degree of freedoms

Node Number	Numbering of Degree of freedom
①	1,2,3
②	4,5,6
③	7,8,9
④	10,11,12

For the example shown in Figure 3.2, the element tangential stiffness matrix from tetrahedron ('TE') $\boldsymbol{K}_e^{TE}$ is written as

$$\boldsymbol{K}_e^{TE} = \begin{bmatrix} p_1^1 & \cdots & p_1^4 & p_1^5 & \cdots & p_1^9 & \cdots & p_1^{12} \\ p_2^1 & \cdots & p_2^4 & p_2^5 & \cdots & p_2^9 & \cdots & p_2^{12} \\ p_3^1 & \cdots & p_3^4 & p_3^5 & \cdots & p_3^9 & \cdots & p_3^{12} \\ p_4^1 & \cdots & p_4^4 & p_4^5 & \cdots & p_4^9 & \cdots & p_4^{12} \\ p_5^1 & \cdots & p_5^4 & p_5^5 & \cdots & p_5^9 & \cdots & p_5^{12} \\ p_6^1 & \cdots & p_6^4 & p_6^5 & \cdots & p_6^9 & \cdots & p_6^{12} \\ p_7^1 & \cdots & p_7^4 & p_7^5 & \cdots & p_7^9 & \cdots & p_7^{12} \\ p_8^1 & \cdots & p_8^4 & p_8^5 & \cdots & p_8^9 & \cdots & p_8^{12} \\ p_9^1 & \cdots & p_9^4 & p_9^5 & \cdots & p_9^9 & \cdots & p_9^{12} \\ p_{10}^1 & \cdots & p_{10}^4 & p_{10}^5 & \cdots & p_{10}^9 & \cdots & p_{10}^{12} \\ p_{11}^1 & \cdots & p_{11}^4 & p_{11}^5 & \cdots & p_{11}^9 & \cdots & p_{11}^{12} \\ p_{12}^1 & \cdots & p_{12}^4 & p_{12}^5 & \cdots & p_{12}^9 & \cdots & p_{12}^{12} \end{bmatrix}_{12\times 12} \tag{3.40}$$

in which the entry p_j^i represents it is located in row j (which is associated with degree j) and column i (which is associated with degree i) in the global system. The element tangential matrix stiffness from truss ('TR') $\boldsymbol{K}_e^{TR}$ is written as

$$\boldsymbol{K}_e^{TR} = \begin{bmatrix} q_4^4 & q_4^5 & q_4^6 & q_4^7 & q_4^8 & q_4^9 \\ q_5^4 & q_5^5 & q_5^6 & q_5^7 & q_5^8 & q_5^9 \\ q_6^4 & q_6^5 & q_6^6 & q_6^7 & q_6^8 & q_6^9 \\ q_7^4 & q_7^5 & q_7^6 & q_7^7 & q_7^8 & q_7^9 \\ q_8^4 & q_8^5 & q_8^6 & q_8^7 & q_8^8 & q_8^9 \\ q_9^4 & q_9^5 & q_9^6 & q_9^7 & q_9^8 & q_9^9 \end{bmatrix}_{6\times 6} \tag{3.41}$$

When assembling $\boldsymbol{K}_e^{TE}$ and $\boldsymbol{K}_e^{TR}$ together, the entries with the same locations in the global system is added together to form the global stiffness matrix $\boldsymbol{K}_{cp}$,

$$\boldsymbol{K}_{cp} = \begin{bmatrix} p_1^1 & \cdots & p_1^4 & p_1^5 & \cdots & p_1^9 & \cdots & p_1^{12} \\ p_2^1 & \cdots & p_2^4 & p_2^5 & \cdots & p_2^9 & \cdots & p_2^{12} \\ p_3^1 & \cdots & p_3^4 & p_3^5 & \cdots & p_3^9 & \cdots & p_3^{12} \\ p_4^1 & \cdots & p_4^4+q_4^4 & p_4^5+q_4^5 & \cdots & p_4^9+q_4^9 & \cdots & p_4^{12} \\ p_5^1 & \cdots & p_5^4+q_5^4 & p_5^5+q_5^5 & \cdots & p_5^9+q_5^9 & \cdots & p_5^{12} \\ p_6^1 & \cdots & p_6^4+q_6^4 & p_6^5+q_6^5 & \cdots & p_6^9+q_6^9 & \cdots & p_6^{12} \\ p_7^1 & \cdots & p_7^4+q_7^4 & p_7^5+q_7^5 & \cdots & p_7^9+q_7^9 & \cdots & p_7^{12} \\ p_8^1 & \cdots & p_8^4+q_8^4 & p_8^5+q_8^5 & \cdots & p_8^9+q_8^9 & \cdots & p_8^{12} \\ p_9^1 & \cdots & p_9^4+q_9^4 & p_9^5+q_9^5 & \cdots & p_9^9+q_9^9 & \cdots & p_9^{12} \\ p_{10}^1 & \cdots & p_{10}^4 & p_{10}^5 & \cdots & p_{10}^9 & \cdots & p_{10}^{12} \\ p_{11}^1 & \cdots & p_{11}^4 & p_{11}^5 & \cdots & p_{11}^9 & \cdots & p_{11}^{12} \\ p_{12}^1 & \cdots & p_{12}^4 & p_{12}^5 & \cdots & p_{12}^9 & \cdots & p_{12}^{12} \end{bmatrix}_{12\times 12} \tag{3.42}$$

Similar assembling process is done with the tetrahedron element force vector and truss element force vector to obtain the global force vector.

4. Mechanical behaviors of the RVE composite

The mechanical behavior of the RVE composite under tensile loading is investigated with emphasis on examining the interaction between the embedded fiber network and matrix material. Section 4.1 provides the problem definition (i.e. boundary conditions, material parameters and network properties) of the RVE composite. Section 4.2 studies the overall constitutive response of the coupled fiber-matrix system; Section 4.3 and 4.4 investigate the interactions between the two constituents; Section 4.5 proposes an analytical method to predict the effective elastic modulus and Poisson's ratio of the RVE composite and compare them with numerical solutions.

4.1 Problem definition

4.1.1 Boundary conditions

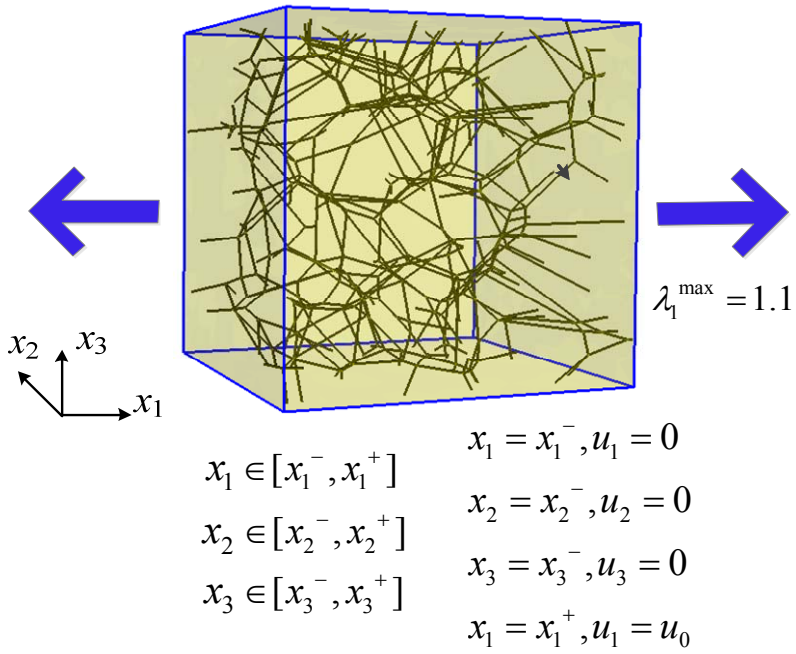

Figure 4.1: Symmetric boundary condition applied in in the uniaxial tensile test.

For the coupled model, strain steps of 0.25% are applied incrementally in the x_1-direction until an RVE strain of 10% is achieved. Symmetric boundary conditions are applied (see Figure 4.1). In Figure 4.1, x_i^+ and x_i^- denote the higher and lower bounds of

the RVE cube in i-direction (i=1, 2, 3); u_i is the displacement in i-direction(i=1, 2, 3); u_0 is the applied displacement boundary condition to the surface perpendicular to x_1 direction and λ_1^{max} is the maximum stretch ratio applied at the RVE cube along x_1 direction. Other faces perpendicular to x_2 and x_3 axes are kept traction free.

4.1.2 Nomenclature

To effectively present the results, table 4.1 summarizes the notations of parameters used in this chapter. The definitions of some parameters are also referenced.

Table 4.1: Nomenclature.

E_{f}	Fiber Young's modulus
A_{f}	Fiber cross-sectional area
E_{m}	Matrix Young's modulus
v_{m}	Matrix Poisson's ratio
G_{m}	Matrix shear modulus
ρ	Network density (see Chapter 2, section 2.2)
l_c	Network mean segment length (see Chapter 2, section 2.2)
Ω_{11}, Ω_{22}, Ω_{33}	Fiber orientation parameter (see Chapter 2, section 2.2)
$\hat{\sigma}_{ij}$	Averaged total stress of the RVE composite
$\hat{\sigma}^{n}_{ij}$	Averaged network stress of the RVE composite
$\hat{\sigma}^{m}_{ij}$	Averaged matrix stress of the RVE composite
σ^{m}_{ij}	Local matrix stress of the RVE composite
$\hat{\lambda}_{\mathrm{f}}$	Mean fiber stretch ratio
$\hat{v}_{\mathrm{app}}$	Apparent ('app') Poisson's ratio of the RVE composite (see Chapter 4, section 4.2)
$\hat{v}$	Effective Poisson's ratio of the RVE composite
$\hat{E}$	Effective modulus of the RVE composite
$\hat{E}^{n}_{aff}$	Effective modulus of the affinely ('aff') deforming network

4.1.3 Material constitutive models

Both nonlinear and linear material constitutive models are employed to represent embedded fiber and matrix. Geometric nonlinearity (i.e. large deformation) has been taken into account in all simulations. The nonlinear material model parameters are selected to fit the experimental results of the collagen-agarose gels [5] and the results are compared with the previously developed parallel model in subsequent section. To

examine the effect of just the geometric nonlinearity, test cases with linear materials are also employed to represent both the fibers and matrix.

The current section describes these two types of material models and also the network properties.

4.1.3.1 Nonlinear material constitutive model and anisotropic network properties

The nonlinear material constitutive models for fibers and matrix materials (described in chapter 3, section 3.1) are employed together with anisotropic Voronoi networks (table 4.2), which are generated and simulated so as to approximate the alignment of collagen-agarose co-gel [5].

Table 4.2: Initial properties of anisotropic Voronoi networks used with nonlinear material models.

	Number of Fibers	**Orientation Parameter**		
Network	*Total*	Ω_{11}	Ω_{22}	Ω_{33}
1	689	0.590	0.196	0.214
2	828	0.625	0.187	0.188
3	668	0.607	0.196	0.197
4	725	0.584	0.198	0.218
5	682	0.597	0.203	0.200
Mean	**718.4**	**0.601**	**0.196**	**0.203**
Std. Dev.	64.8	0.016	0.006	0.012

Figure 4.2~4.5 and Figure 4.7 are obtained from nonlinear material model and anisotropic networks.

4.1.3.2 Linear material constitutive models and isotropic network properties

In the case of linear elastic material models, the matrix material is described with Young's modulus E_m and Poisson ratio υ_m. The fibers are also described by a linear elastic model with modulus E_f, and have cross-sectional area A_f. The relevant quantity is actually the axial stiffness of the fibers, $E_f A_f$, which is kept as a parameter. The range

over which these parameters are varied is: $E_m \in [10, 10^5]Pa$, υ_m=0.3, $E_fA_f \in$ [8.17,65.34] *N*. Isotropic fiber networks (table 4.3) are used with linear material models.

Table 4.3: Initial properties of isotropic Voronoi networks used with linear material models.

	Number of Fibers	**Orientation Parameters**		
Network	*Total*	Ω_{11}	Ω_{22}	Ω_{33}
1	703	0.347	0.342	0.311
2	711	0.324	0.345	0.331
3	717	0.342	0.336	0.322
4	710	0.337	0.345	0.318
5	754	0.318	0.331	0.351
Mean	719	0.334	0.340	0.326
Std. Dev.	20.2	0.012	0.006	0.0154

Figure 4.6 and Figure 4.8~4.13 are obtained with linear material model and isotropic networks.

4.2 Overall RVE constitutive response

4.2.1 Overall RVE constitutive response with nonlinear materials

The RVE constitutive responses under tensile loading are described by reporting (1) the averaged network stress $\hat{\sigma}_{11}^{n}$, (2) the averaged matrix stress $\hat{\sigma}_{11}^{m}$, (3) the averaged total stress, $\hat{\sigma}_{11}$ (4) the apparent Poisson's ratio $\hat{\nu}_{\text{app}}$ (Eq. 4.1) .

The overall Cauchy stress, $\hat{\sigma}_{11}$, is evaluated based on the reactions evaluated on the face with normal in the x_1 direction, and the current area of the respective model boundary segment. Formally one may refer to stresses associated with the network and with the matrix, i.e. $\hat{\sigma}_{11} = \hat{\sigma}_{11}^{m} + \hat{\sigma}_{11}^{n}$, the two components being computed with the reactions acting at the nodes where the network intersects the model boundary and those corresponding to matrix elements, respectively.

The apparent Poisson's ratio $\hat{\nu}_{\text{app}}$ is obtained by averaging $\hat{\nu}_{12}$ and $\hat{\nu}_{13}$ (Eq. 4.1), which are apparent Poisson's ratio in directions x_1 and x_2 and directions x_1 and x_3 respectively.

$$\hat{\nu}_{12} = -\frac{\ln \lambda_2}{\ln \lambda_1}, \hat{\nu}_{13} = -\frac{\ln \lambda_3}{\ln \lambda_1} \tag{4.1a}$$

$$\hat{\nu}_{\text{app}} = \frac{\nu_{12} + \nu_{13}}{2} \tag{4.1b}$$

where λ_1, λ_2 and λ_3 are stretch ratios of the RVE along x_1, x_2 and x_3 axes respectively. Since nodal displacements on traction-free surfaces normal to x_2 and x_3 direction are not constrained, λ_2 and λ_3 are calculated by averaging the associated displacement component over all boundary nodes on surfaces normal to x_2 and x_3 axes respectively.

In the coupled fiber-matrix model [1], the stress due to the fiber network $\hat{\sigma}_{11}^{n}$ increases with increasing non-fibrillar matrix (NFM) shear modulus G_{m}, and the non-linearity of fiber stress-strain curves become less pronounced at higher G_{m} values

[1] Portions of this chapter previously appeared as: (1) L. Zhang, S. P. Lake, V. K. Lai, C. R. Picu, V. H. Barocas, and M. S. Shephard, "A coupled fiber-matrix model demonstrates highly inhomogeneous microstructural interactions in soft tissues under tensile load," J. Biomech. Eng., vol. 135, p. 011008, Jan. 2013, and
(2) L. Zhang, S. P. Lake, V. H. Barocas, M. S. Shephard, and R. C. Picu, "Cross-linked fiber network embedded in an elastic matrix," Soft Matter, vol. 9, p. 6398, 2013.

(Figure 4.2(a)). As one might expect, the matrix stress $\hat{\sigma}_{11}^{m}$ increases with increasing NFM shear modulus (Figure 4.2(b)), which accounts for much of the increase in total stress (Figure 4.2(c)). The RVE Poisson's ratio decreases with increasing G_m, but increases with strain for G_m =10 and 110 Pa (Figure 4.2(d)).

In addition to comparing model results computed at the same imposed strain, results are also evaluated at the same imposed total stress $\hat{\sigma}_{11}$ (in this case, 200 Pa). Matrix stress values $\hat{\sigma}_{11}^{m}$ increase with increasing shear modulus for both cases (Figure 4.3(a)). In contrast, fiber stress $\hat{\sigma}_{11}^{n}$ values increase for the constant strain case, but decrease for the constant total stress case (Figure 4.3(b)), with the stiffer NFM shielding the network.

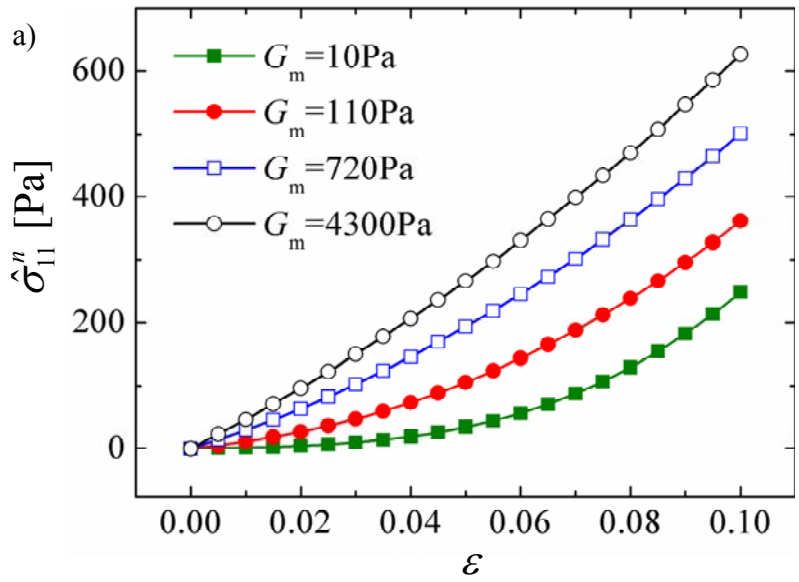

b)

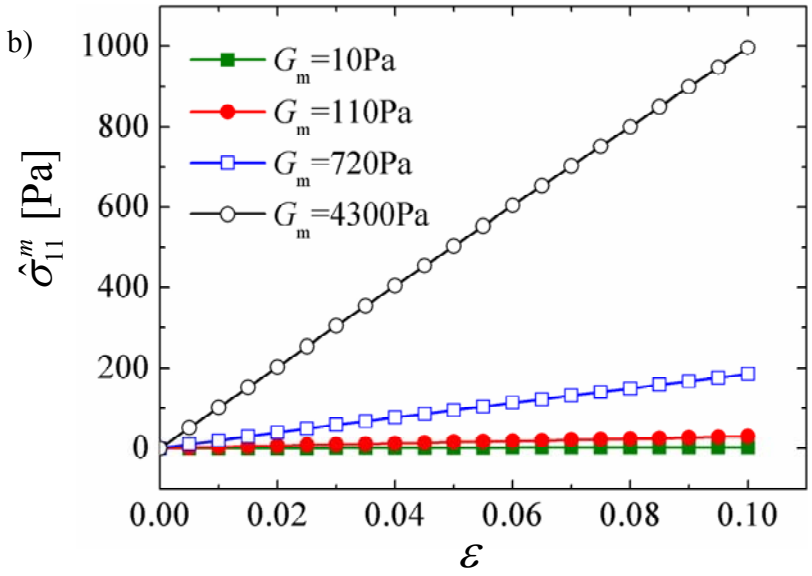
1000
800
600
400
200
0
0.00
0.02
0.04
0.06
0.08
0.10
$\hat{\sigma}_{11}^{m}$ [Pa]
ε
G_m=10Pa
G_m=110Pa
G_m=720Pa
G_m=4300Pa

c)

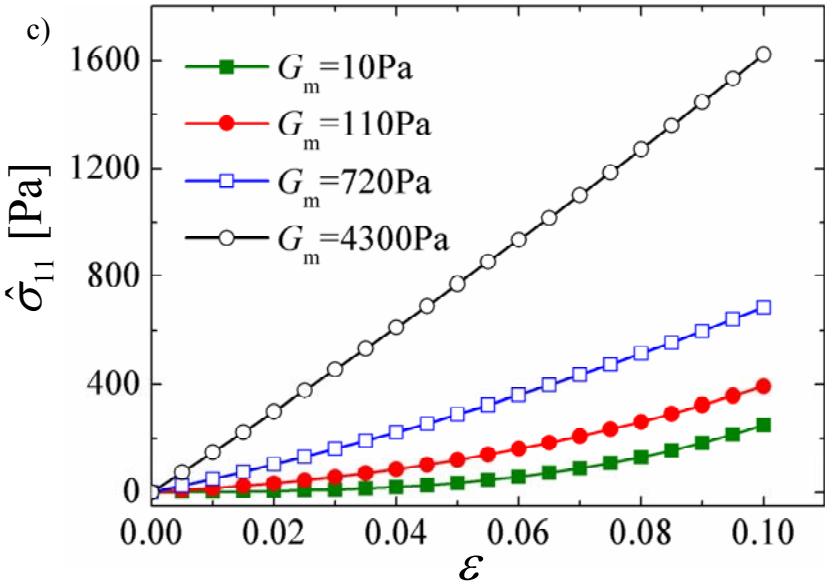
1600
1200
800
400
0
0.00
0.02
0.04
0.06
0.08
0.10
$\hat{\sigma}_{11}$ [Pa]
ε
G_m=10Pa
G_m=110Pa
G_m=720Pa
G_m=4300Pa

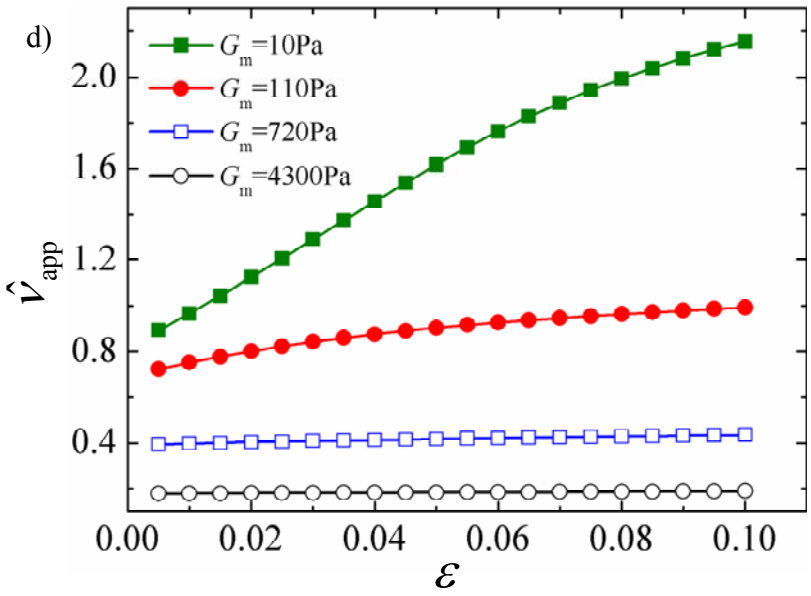

Figure 4.2: (a) Averaged fiber stress, (b) averaged matrix stress, (c) averagedtotalstress, and (d) apparent RVE Poisson's ratio vs. engineering strain $\varepsilon$for the coupled fiber-matrix model at varying values of G_m.

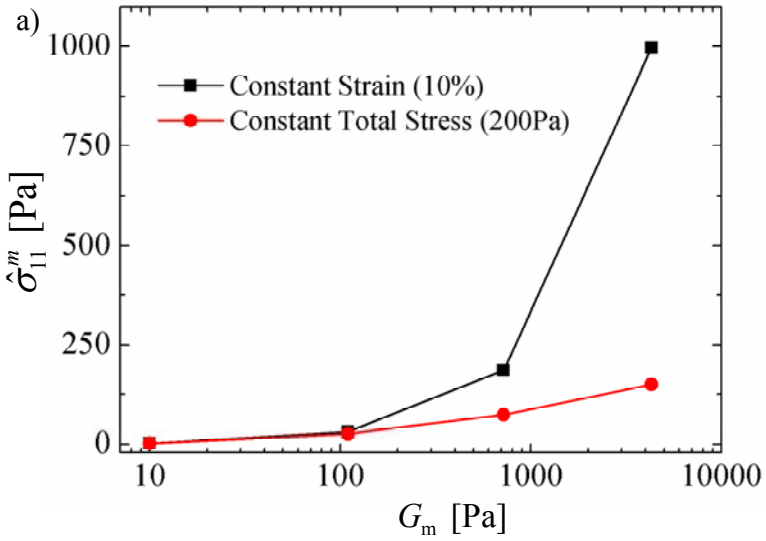

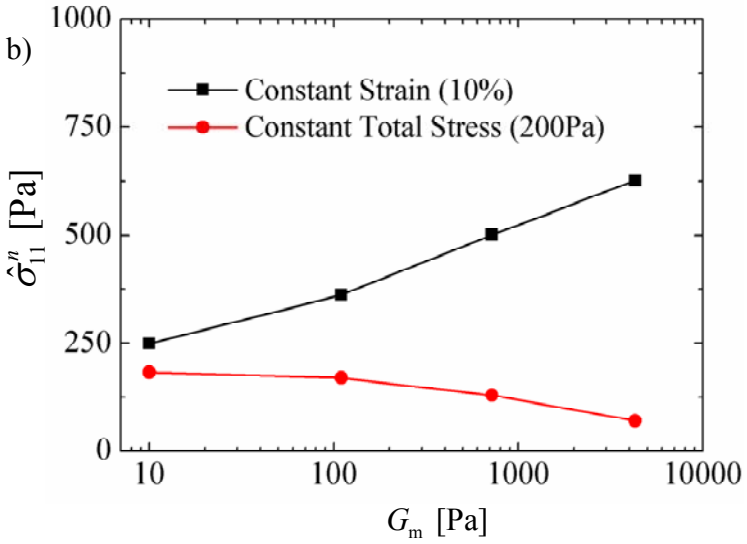

Figure 4.3: Magnitude of stress contributions are different functions of whether simulation results are evaluated at constant total strain or constant total stress; (a) while matrix stress values increase in both cases, (b) fiber stresses show opposite trends for the two cases, where decreasing values for the constant-stress case demonstrates stress-shielding (by the matrix) at high shear modulus.

4.2.2 Comparison between the coupled model and parallel model

Results from the coupled model with nonlinear fiber and matrix are compared with those from the parallel model [45]. A brief review of the parallel model is provided.

4.2.2.1 Parallel Model

In the parallel model, the stress due to the embedded network is computed via a volume-averaging approach based on the nodal forces on each RVE boundary:

$$\hat{\sigma}_{ij}^{n} = \frac{1}{V} \sum_{\substack{\text{boundary} \\ \text{node}}} x_i f_j \tag{4.2}$$

where $\hat{\sigma}_{ij}^{n}$ is the volume averaged Cauchy stress from network, V is RVE volume, and f_j are the forces acting on boundary nodes (at positions x_i). The matrix stresses are dependent only on the macroscopic deformation of the RVE, and the two stress fields are combined in a simple summed (parallel) sense:

$$\hat{\sigma}_{ij} = \hat{\sigma}_{ij}^{n} + \sigma_{ij}^{m} \tag{4.3a}$$

where $\hat{\sigma}_{ij}$ is the averaged total stress and σ_{ij}^{m} is the matrix stress, which is calculated by

$$\sigma_{11}^{m} = G_m(\frac{\lambda_1^{\,2}}{J} - J^{-2\beta-1}) \tag{4.3b}$$

where G_m is the shear modulus and the matrix, λ_1 is the RVE stretch ratio (here λ_1=1.1), J is the Jacobian, $\beta = \nu_m/(1-2\nu_m)$ and ν_m is the Poisson's ratio of matrix. Other components of matrix stress are zero.

After application of RVE strain, positions of the internal nodes and of the unloaded boundaries are adjusted iteratively until the force balance at each internal node is satisfied and the total stresses on the free surfaces are minimized.

4.2.2.2 Results Comparison between parallel and coupled model

The results of coupled fiber-matrix model are compared with those from parallel model through the following measures: (1) Averaged network stress $\hat{\sigma}_{11}^{n}$ and matrix stress $\hat{\sigma}_{11}^{m}$; (2) Apparent Poisson's ratio of the composite RVE $\hat{\nu}_{\text{app}}$; (3) Average fiber stretch ratio $\hat{\lambda}_{\text{f}}$; (4) Fiber orientation parameter Ω_{11}.

Results from the coupled model are similar to those from the parallel model for the system parameters used in this study. Specifically, the parallel and coupled models produce nearly identical average matrix stress values (Figure 4.4(a)). The coupled model exhibits smaller fiber stress values (Figure 4.4(b)), but both models show similar fractions of total stress as a function of different G_{m} (Figure 4.4(c)). In both cases, when ν_{m} is increased from 0.1 to 0.45, a slight increase and decrease are seen in fiber and matrix stress, respectively, with no net change in total stress.

In addition to normal stresses in the loading direction, several other metrics are similar for the coupled and parallel models. The average fiber stretch increases with increasing G_{m} (Figure 4.5(a)), while apparent Poisson's ratio $\hat{\nu}_{\text{app}}$ (Figure 4.5(b)) and fiber orientation represented via Ω_{11}, Figure 4.5(c)), both decrease with increasing G_{m}. For each of these output parameters, the values are slightly smaller for the coupled model, but show the same patterns of change as a function of shear modulus. At high

NFM Poisson's ratio (i.e., ν_m=0.45), $\hat{\lambda}_f$ and $\hat{\nu}_{app}$ are slightly increased and decreased, respectively, with no change in Ω_{11}.

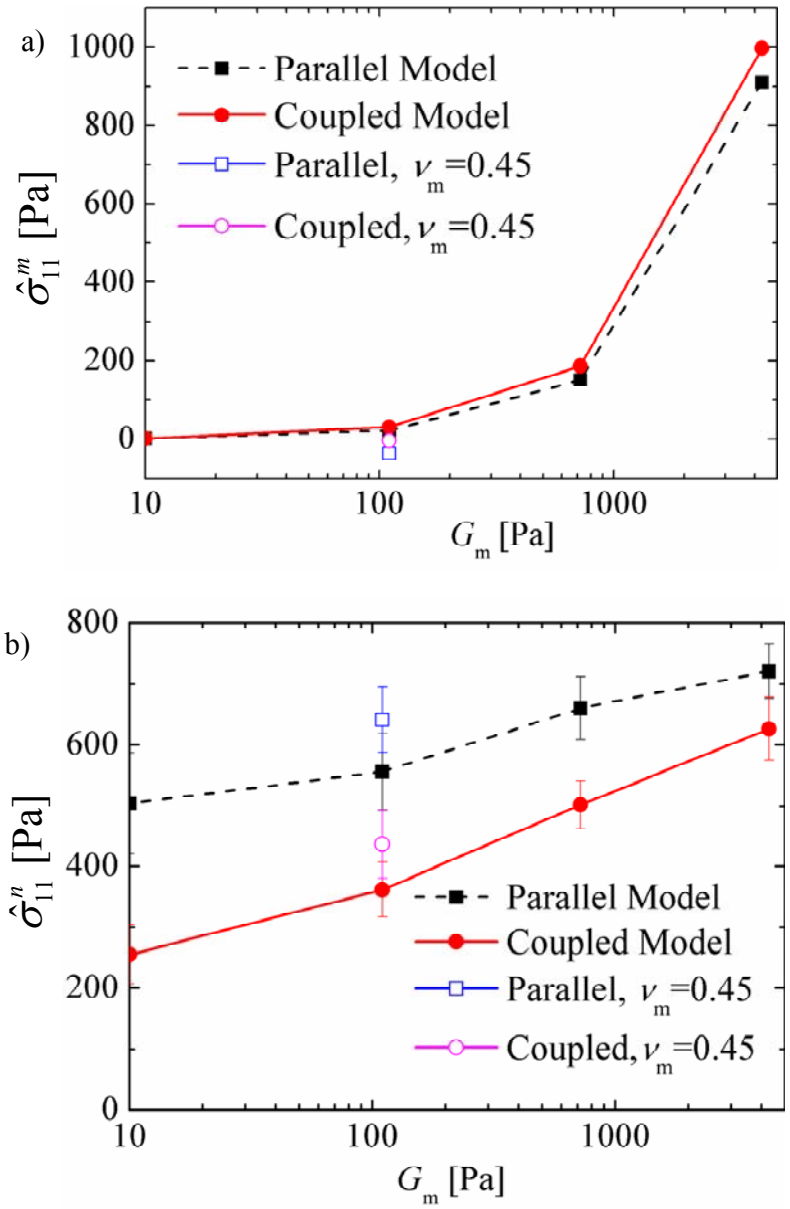

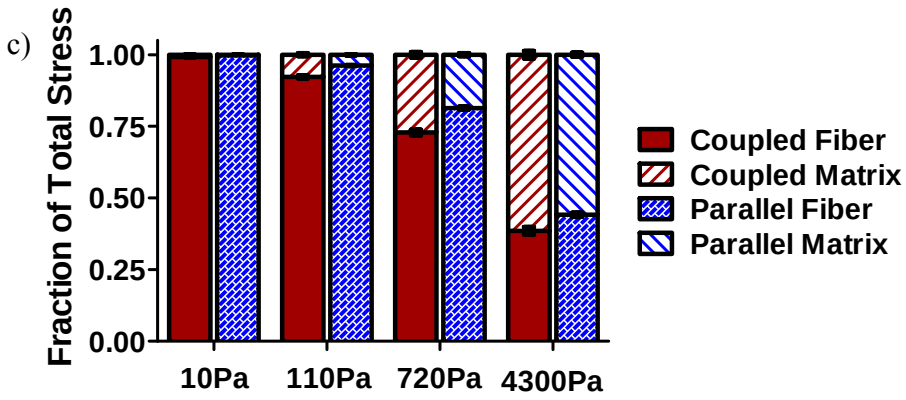

Figure 4.4: Average (a) matrix stress, (b) fiber stress, and (c) fraction of total stress at 10% strain and with ν_m=0.1 show good agreement between the parallel and coupled models; stress values at a larger Poisson's ratio (i.e., ν_m=0.45) at G_m =110Pa show a small shift of stress from the matrix to fibers.

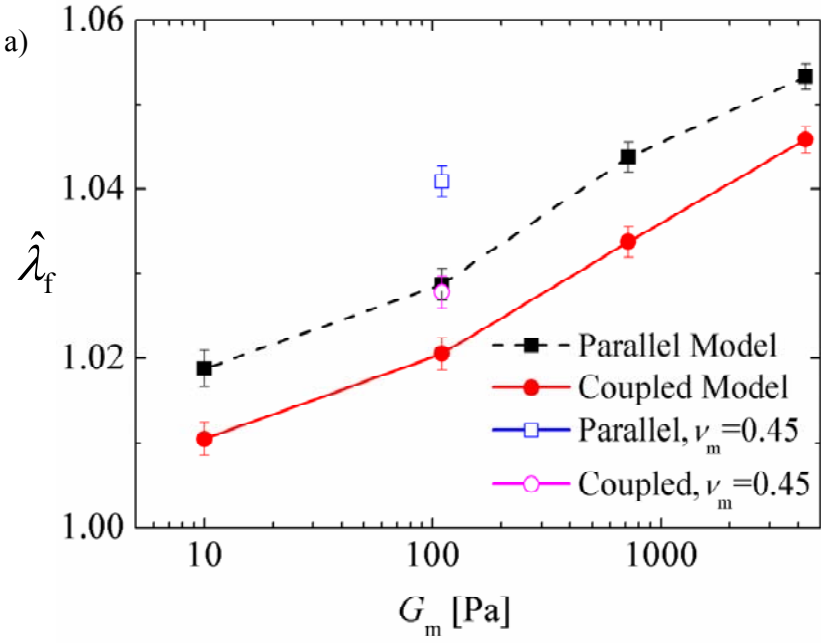

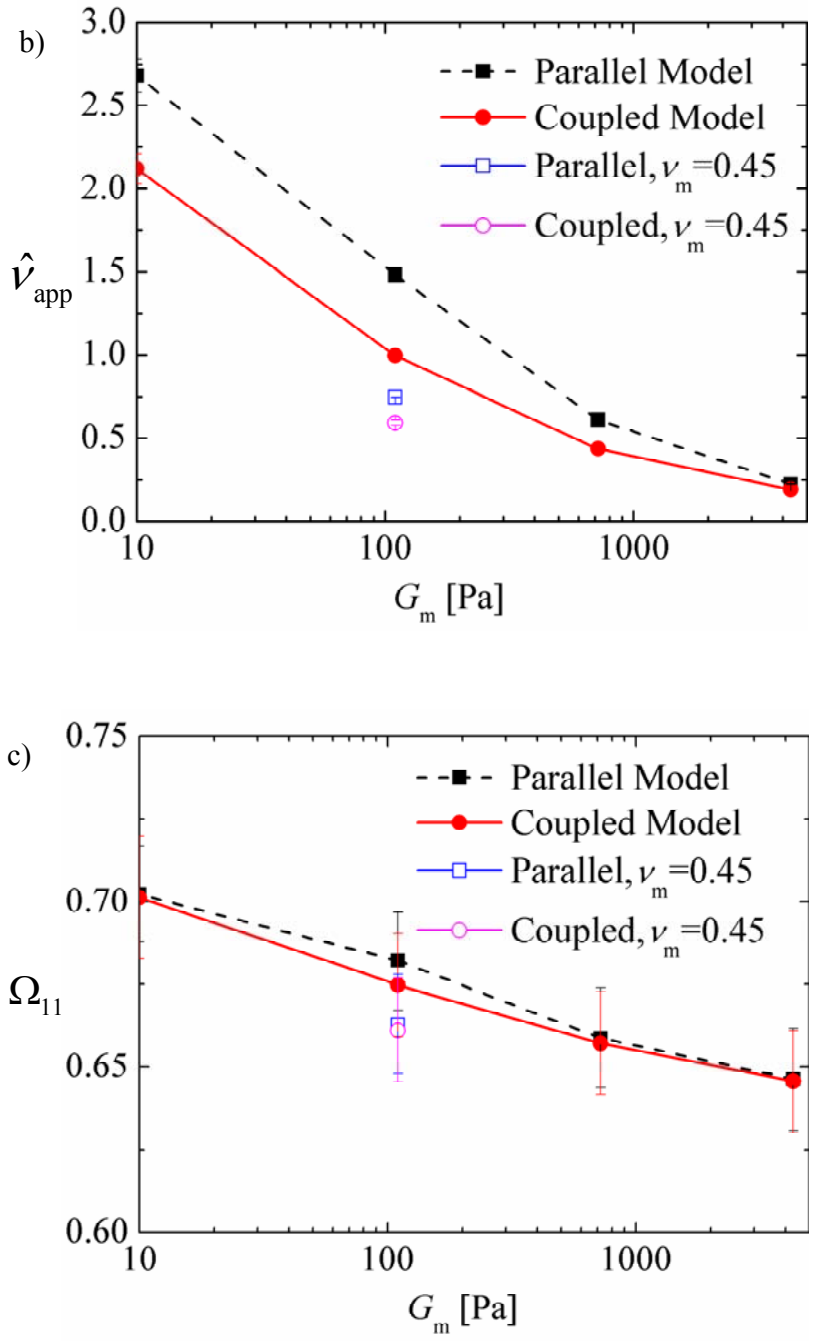

Figure 4.5: (a) average fiber stretch $\hat{\lambda}_f$, (b) apparent RVE Poisson's ratio $\hat{\nu}_{app}$, and (c) fiber orientation Ω_{11} at 10% strain and with ν_m=0.1 show decreased values for the coupled model compared to the parallel model, but similar qualitative changes as a function of increasing G_m; for the case where ν_m=0.1 and G_m=110Pa, fiber stretch and Poisson's ratio increased and decreased, respectively, with no change in Ω_{11}.

4.2.3 RVE constitutive response with linear material models

To examine the effect of only the geometric nonlinearity on the RVE constitutive response, a linear material model is employed to represent fiber and matrix in this section [58]. The stress-strain curves of all systems considered are non-linear. The non-linearity here is purely geometric since the constitutive equations of the matrix and fiber materials are both linear. Figures 4.6(a) and 4.6(b) show the stress strain curves, $\hat{\sigma}_{11}(\epsilon)$, of two models with E_m=10 and 10^4 Pa, respectively. The embedded network characterized by E_fA_f= 8.168N and l_c/L = 0.104, is embedded in the two matrices. The filled symbols correspond to the total stress $\hat{\sigma}_{11}(\epsilon)$, while the open symbols correspond to the component of the total stress associated with the network, $\hat{\sigma}^n_{11}(\epsilon)$. In the stiffer matrix case (Figure 4.6(a)), the network contributes little to the overall modulus, as expected, and the degree of non-linearity of $\hat{\sigma}_{11}(\epsilon)$ is small. The situation is reversed in the softer matrix case (Figure 4.6(b)). The non-linearity of the network is pronounced and this reflects in $\hat{\sigma}_{11}(\epsilon)$. The data indicate the intuitive fact that the non-linearity in the behavior of the network-matrix system is associated with the large geometric non-linearity of the network. To make this effect more obvious, Figure 4.6(c) shows the contribution to these stress-strain curves from the non-linear component. Denote by $\hat{E}$ the small strain effective modulus of the network-matrix system ($\hat{E} = \hat{\sigma}_{11}/\epsilon$ for $\epsilon \to 0$), and further, define $\hat{E}^n = \hat{\sigma}^n_{11}/\epsilon$ for $\epsilon \to 0$. The non-linear component is evaluated as

$$NL(\varepsilon) = (\hat{\sigma}_{11}(\varepsilon) - \hat{E}\varepsilon) / \hat{\sigma}_{11}(\varepsilon) \tag{4.4}$$

The non-linearity is much more pronounced in the soft matrix case, while the network component is always more non-linear than the total stress-strain curve.

a)

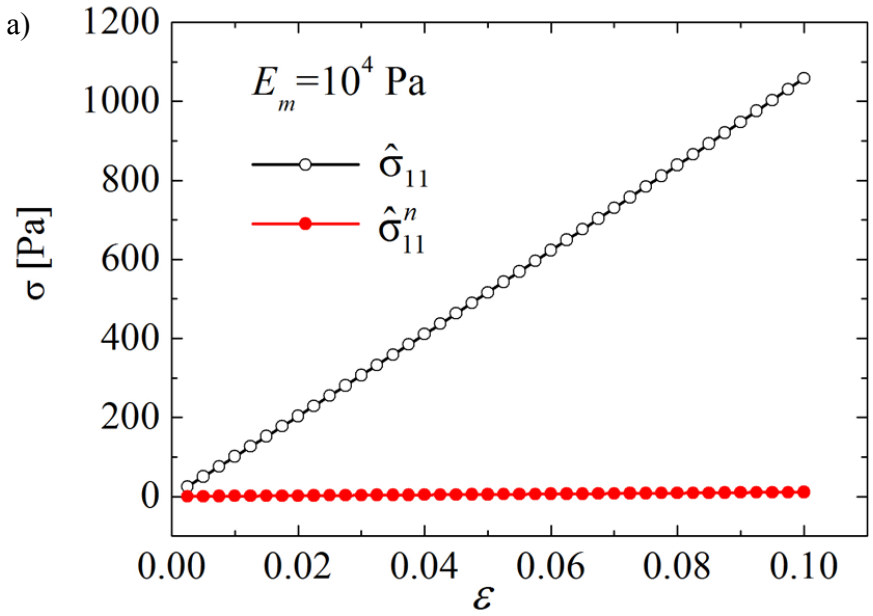
1200
1000
800
600
400
200
0
σ [Pa]
E_m=10^4 Pa
$\hat{\sigma}_{11}$
$\hat{\sigma}^n_{11}$
0.00
0.02
0.04
0.06
0.08
0.10
ε

b)

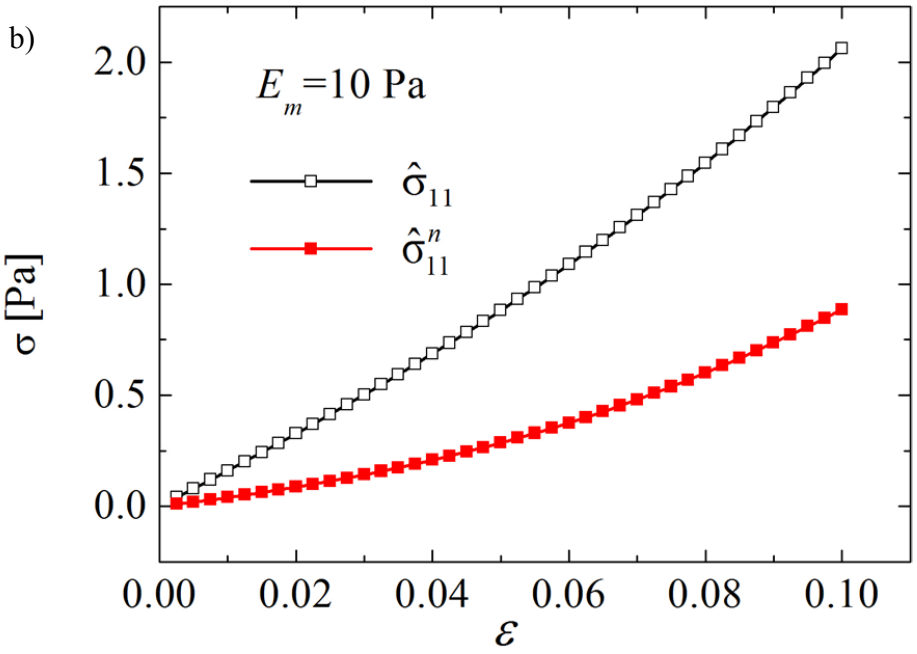
2.0
1.5
1.0
0.5
0.0
σ [Pa]
E_m=10 Pa
$\hat{\sigma}_{11}$
$\hat{\sigma}^n_{11}$
0.00
0.02
0.04
0.06
0.08
0.10
ε

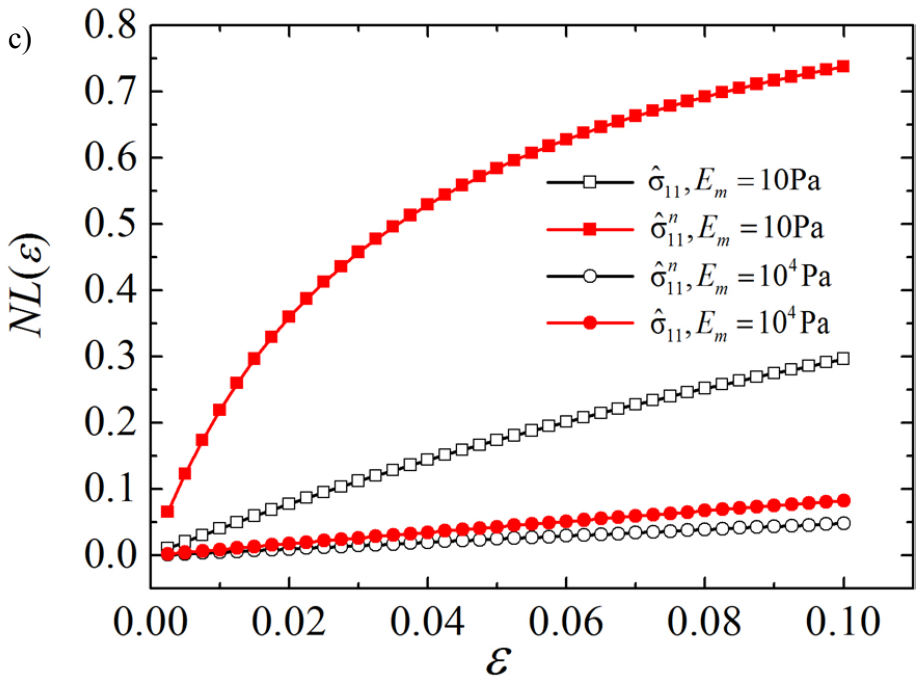

Figure 4.6: Stress-strain curves for the matrix-fiber system and for the network evaluated for systems with (a) Em = 10^4 (b) 10 Pa and (c) Nonlinearity parameter of Eq. (4.4) corresponding to the total and fiber stress-strain relationships.

4.2.4 Discussion

In section 4.2.2, we compare the detailed coupled model to the parallel model. Matrix stress (Figure 4.4(a)), total stress fraction (Figure 4.4(c)), fiber orientation (Figure 4.5(c)), and Poisson's ratio values (Figure 4.5(b)) agree particularly well between the two models, while the coupled model demonstrates slightly lower mean fiber stretch (Figure 4.5(a)) and fiber stress values (Figure 4.5(b)) than the parallel model. This discrepancy could be due to a mechanism wherein the matrix material has a stronger stress shielding effect on the embedded collagen network in the coupled model than in the parallel model. The stress shielding effect is revealed in Figure 4.3(b), in which fiber stress decreases as matrix material stiffness increases at constant stress.

Results obtained via the coupled model for bulk RVE properties are generally as expected. Stress values increase with strain, and both fiber and matrix stresses at a given strain increase with NFM shear modulus (Figure 4.2). A nonlinear toe-region with an initially low modulus is observed in the fiber stress-strain curve at small NFM modulus

values, but nonlinearity is less pronounced at larger NFM modulus values. The tendency toward linearity is consistent with a stiffer matrix eliminating the non-affine, low-stretch reorientation of the fiber network, which is proved in subsequent sections on the interactions between the two constituents.

In addition, the nonlinear relationship of Poisson's ratio and strain at low G_m (Figure 4.2(d)) closely matched the relationship observed in experimental tests of collagen-agarose co-gels [5]. The bulk RVE stresses analyzed in this model are obtained from simulations at a constant strain value (e.g., 10% stretch). When results are computed at a constant total stress (200 Pa) for each of the varied simulations, fiber stresses decrease with increasing NFM modulus, demonstrating a stress shielding role of the NFM at large G_m.

4.3 Effect of fiber network on matrix – the case of linear material models

This section focuses on investigating the effect of the fiber network on the matrix material. The effect is outlined by analyzing (1) the probability distribution function of matrix element stresses, and (2) the variation of stress within the matrix. Obviously, the matrix without the embedded network deforms affinely and, in this case, the stress is uniform throughout.

4.3.1 Inhomogeneous stress distribution in the matrix

The use of the coupled model allows for full-field quantification of the six independent Cauchy stress components of the matrix material, visualized via slice plots through the RVE midsection. The embedded fiber network had a significant effect on the stress field of the surrounding matrix material, as demonstrated by the inhomogeneity of the internal stress distribution. Figure 4.7 shows representative plots of stress fields for the system with matrix shear modulus G_m = 720 Pa. The black dots in Figure 4.7 represent the intersection points between fibers and the cutting plane.

Tensile normal stresses (i.e., positive values) are evident in the loading direction (σ_{11}), whereas compressive stresses are observed in the transverse directions (e.g., σ_{22} and σ_{33}) in response to the extreme tendency of the collagen network to contract in the

transverse directions. Stress concentrations (either positive or negative) occur at locations where two or more fibers traverse the slice plane in close proximity.

The tensile normal stresses in the loading direction (σ_{11}) are relatively consistent across the RVEs, although smaller values are observed in the vicinity of multiple fiber intersection points. Compressive normal stresses in traverse directions (i.e., σ_{22} and σ_{33}) are caused by fibers squeezing the surrounding matrix material in the lateral direction during reorientation. Due to the Poisson effect, the matrix material is compressed in the lateral directions as it is concurrently stretched in the loading direction, thereby decreasing the local tensile stress and leading to smaller σ_{11} values in areas of concentrated fiber intersection points. Maps of internal shear stresses demonstrate complex patterns (Figure 4.7(bottom)), with areas of particularly high shear stress co-localized with significant fiber clustering.

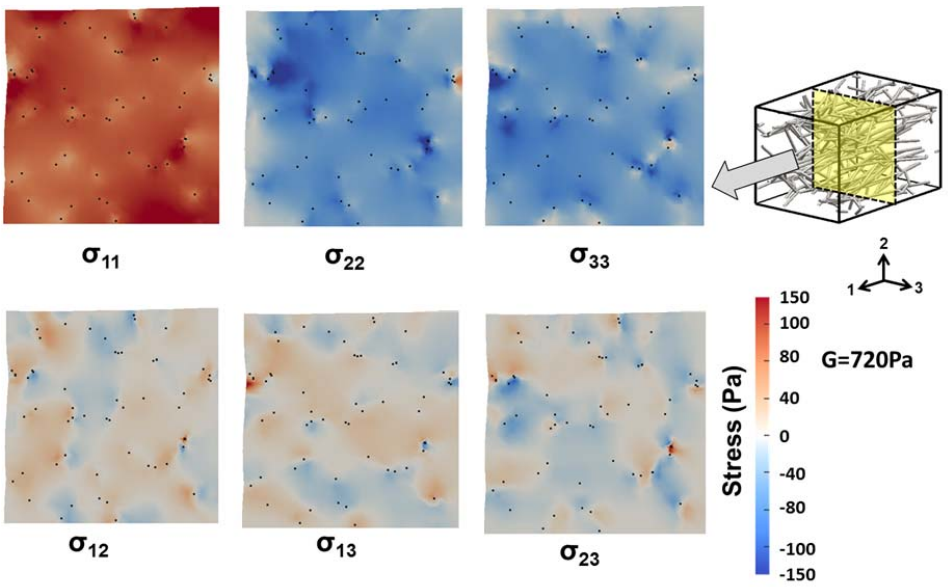

Figure 4.7: Interior normal and shear stress fields at 10% strain on the mid-section slice for a representative network (G_m=720Pa; ν_m=0.1) demonstrates a highly inhomogeneous distribution for all six independent stress components; slices are cut normal to the loading (x_1) direction in the 2-3 plane (represented by the dashed lines in the RVE schematic) and black dots indicate locations of fibers intersecting the cutting plane.

In presenting these stress field plots, we acknowledge that the magnitudes of the stresses contained therein have not been validated against experimental values. To date, only the average stresses of the parallel model have been confirmed by experiments [5]. However, we believe the pronounced inhomogeneity of the stress fields presented here to be real while the magnitude of stress values in areas of stress concentration (e.g., where many fibers intersect the cutting plane) may be subject to modeling and/or discretization error. The discretization error could be reduced with additional mesh refinement in the locations of these higher stress values. However, more detailed consideration of these local stresses should also consider the effects of the current modeling assumptions, particularly the treatment of the fibers. Our interpretation thus focuses on location and relative stress magnitudes instead of absolute magnitudes. Novel experimental techniques (e.g., 3D traction force microscopy [59]) may allow future estimation of internal stress fields in multicomponent tissues and more complete testing of this coupled microstructural model.

4.3.2 Probability distribution function of matrix element stresses

For a more accurate, statistical characterization of the stress distribution in the matrix, we evaluate the probability distribution function (PDF) of several stress components. Note that results presented in the current and subsequent sections in chapter 4 are obtained with linear material model.

The PDF is calculated in a standard way, in three steps: (1) divide the range of stress values into a series of bins $[s_i, s_{i+1}]$ with $s_{i+1} - s_i = \Delta s$; (2) Count N_i - the number of stress values that fall into the bin $[s_i, s_{i+1}]$ and plot the histogram of stress values (3) normalize N_i by $\sum_i N_i \Delta s$, which is the total area under the histogram curve to get PDF.

Let us consider systems in which an isotropic network with $E_f A_f = 8.168$ N and $l_c/L = 0.104$ is embedded in matrices of different moduli, E_m, and deform these systems up to $\epsilon = 0.105$. Figure 4.8 shows the probability distribution functions (PDF) of normal stresses σ_{11}^{m} and σ_{22}^{m} evaluated locally in the matrix elements. The horizontal axis is normalized by E_m in order to allow direct comparison of the various cases considered. In the pure matrix case, the PDFs are delta functions located at 0.105 and 0 (Figs. 4.8(a)

and 4.8(b), respectively) corresponding to σ_{11}^{m} and σ_{22}^{m}. In presence of the network, the PDFs are broad, with the second moment increasing as E_m decreases. Hence, the network induces large spatial stress variability in soft matrices. This is an important observation since the stress states control fracture and damage accumulation during fatigue loading.

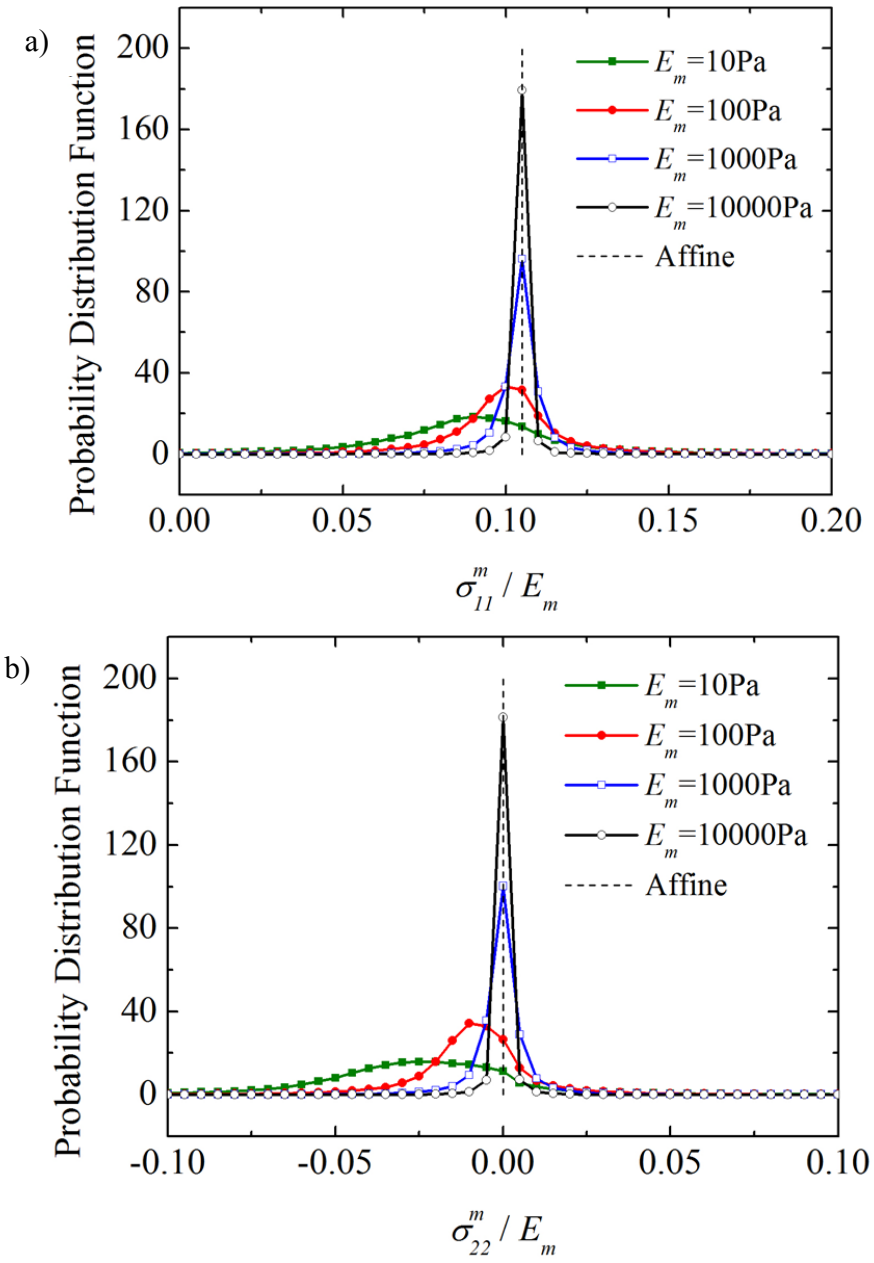

Figure 4.8: Probability distribution functions of normalized σ_{11}^{m} (a) and σ_{22}^{m} (b) computed in the matrix. The stress is normalized with the matrix modulus, E_m.

It is also interesting to observe that the means of the PDFs in Figure 4.8(a) shift to smaller values as the matrix stiffness decreases. In other words, when subjected to the same global strain, a system with a softer matrix would carry smaller normalized stresses (normalization with E_m) than a system with a stiffer matrix. A similar effect is observed in Figure 4.8(b)) where it is seen that the mean increases in absolute value as E_m decreases. This effect was discussed in [52] and it is due to the fact that the network subjected to tension has a Poisson ratio much larger than that of the matrix. Therefore, when the same strain is imposed in the x_1 direction on the network and matrix, the network tends to shrink more in the x_2 and x_3 directions, therefore compressing the matrix. This leads to a mean compressive stress in x_2 and x_3, and, due to the Poisson effect of the matrix, to unloading in the x_1 direction.

4.3.3 Locations of stress concentration in the matrix material

Since the fibers are represented by straight truss segments in this model, the interaction between network and matrix takes place exclusively through forces applied by the network on the matrix at the cross-links. The situation is expected to remain qualitatively similar even in presence of moderate fiber crimp and curl and when the interface between fibers and matrix are weak. This leads to significant stress concentration and a highly heterogeneous stress field characterized by the broad distributions of Figure 4.8. To demonstrate the presence of such concentration sites, the locations (Gauss points) where stress is larger than a specified threshold are identified and the pair correlation function, g(r), of these points is computed. A brief explanation of the calculation of g(r) is as follows:

- **Calculation of the pair correlation function g(r)**

(1) Create a series of concentric spherical bins with radius r_j (j=1,2,…, $N_i^{\max}$) centered at each fiber crosslink i within the RVE (see Figure 4.9). $N_i^{\max}$ is the number of concentric bins centered at crosslink i inside the RVE. The volume of each bin V_j is

$$V_j = \frac{4}{3}\pi(r_j^{\,3} - r_{j-1}^{\,3}), r_j = j\Delta r \tag{4.5}$$

(2) Loop over all bins created inside the RVE to count the total number of high-stress elements, denoted as N_j^{HS} .

(3) Compute the averaged density $g(r_j)$ of Gauss points carrying stresses larger than an imposed threshold.

$$g(\mathrm{r}_j) = \frac{N_j^{HS}}{N_j^{Bin}} / V_j \tag{4.6}$$

in which N_j^{Bin} is the total number of bins inside the RVE with a distance r_j from its center(fiber crosslink).

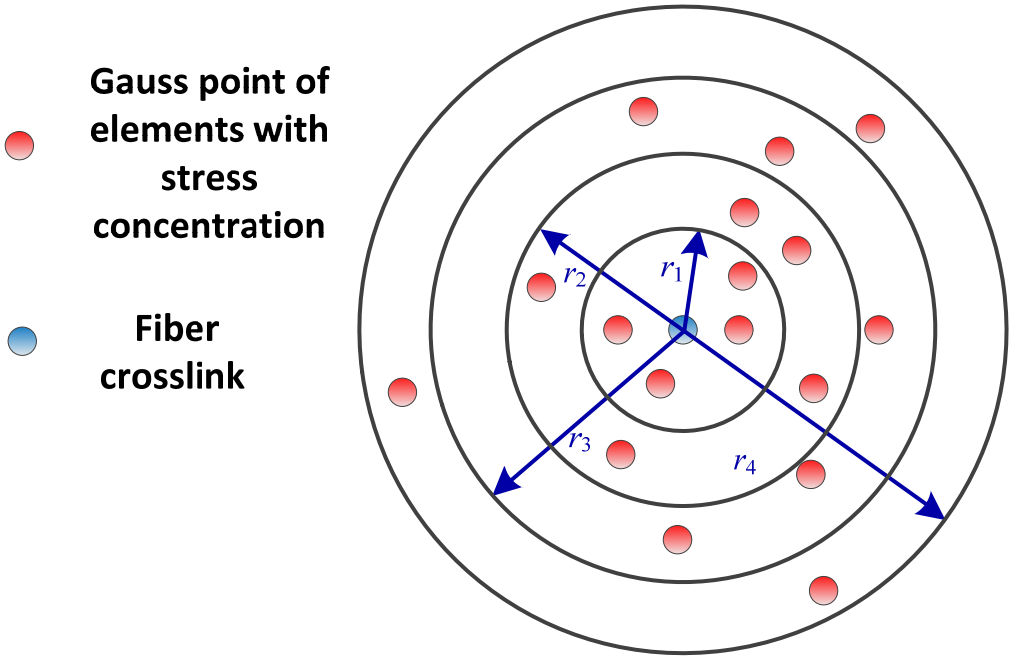

Figure 4.9: Calculation of pair correlation function *g*(*r*).

Consider a system with E_m = 10 Pa and impose a threshold stress for the calculation of $g(r)$ equal to the standard deviation of the curve in Figure 4.8(a). $g(r)$ is computed for this set of points with the origin being selected always at cross-links. The resulting function is normalized by $g_0(r)$, the pair correlation function evaluated for all Gauss points of the matrix elements, irrespective of the stress carried (which is equivalent to reducing the threshold stress for the evaluation of $g_0(r)$ to zero), and with the same origin. The ratio $g(r)/g_0(r)$ represents the fraction of the Gauss points carrying stresses

larger than the imposed threshold (Figure 4.10). It is clear that large stresses are found predominantly close to the cross-links of the network ($r \rightarrow 0$). The asymptote at larger values of the variable represents the fraction of all Gauss points of the model carrying stresses larger than the imposed threshold.

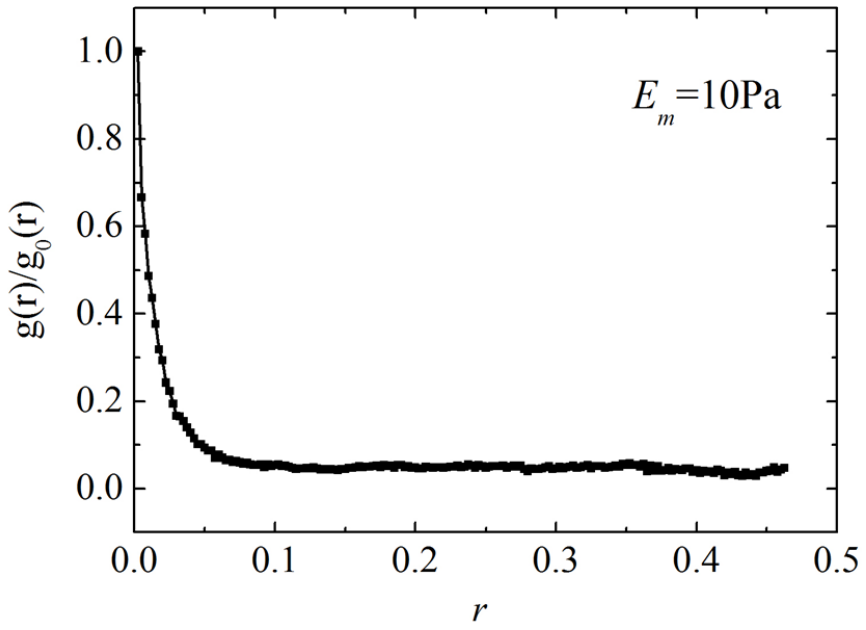

Figure 4.10: Normalized pair correlation function g(r) indicating stress concentration close to the network cross-links (i.e. at $r \rightarrow 0$).

4.4 Effect of matrix material on the fiber network – the case of linear material models

Networks of trusses are known to be unstable if the coordination number, z, is smaller than 2d, where d is the dimensionality of the embedding space [60]. Networks with lower coordination numbers are floppy and deform without storing energy. The networks considered in this study have coordination number $z = 4$, smaller than the value of 6 required for stability and hence are intrinsically floppy. As discussed in the literature [23, 28, 60], a floppy network can be stabilized by accounting for the bending stiffness of fibers and by transforming the cross-links into connectors that transmit both moments and forces between the fibers in contact. A floppy network acquires stiffness

after a certain amount of strain is applied. In the case discussed here, the floppy network is stabilized by the presence of the matrix. Even a matrix with very small E_m performs this function.

Fiber networks are highly heterogeneous structures which, at low density, low cross-link density, and/or low fiber bending stiffness (relative to the axial stiffness), deform non-affinely [26, 28]. The deformation is approximately affine at high densities and/or higher fiber bending stiffness. Various measures of non-affinity have been proposed [28, 29, 30]. Here we use the measure described by:

$$H = \frac{\left\| \boldsymbol{u}^{NF} - \boldsymbol{u}^{AF} \right\|}{\left\| \boldsymbol{u}^{AF} \right\|} \tag{4.7}$$

where $\boldsymbol{u}^{NF}$ and $\boldsymbol{u}^{AF}$ are the displacements of the cross-links in the actual case (NF), and when the deformation is affine (AF); $\|\bullet\|$ is the Euclidean length of a vector (Eq.4.8), which is equivalent with an average over components of the vector,

$$\|\boldsymbol{v}\| = \sqrt{v_1^{\,2} + v_2^{\,2} + \ldots + v_n^{\,2}} \tag{4.8}$$

where v_i is i^{th} component of vector $\boldsymbol{v}$, n is the size of vector $\boldsymbol{v}$.

Define the norm and indicate it is equivalent with an average over the entire system.

Figure 4.11 shows the value of the non-affinity parameter of Eq. (4.7) computed for networks embedded in matrices with various E_m. The non-affinity is pronounced when E_m is small and decreases to zero as E_m increases. Therefore, in the limit of large matrix stiffness, the network deforms affinely. This is possible only if constraint forces, the reactions of the forces acting on the matrix described in section 4.3, act on the network at the cross-links. In the limit of large E_m, the network is more compliant than the matrix and hence the internal forces imposing the compatibility of the two constituents do not lead to significant matrix deformations. Hence, in this limit, the network follows the matrix and deforms affinely.

a)

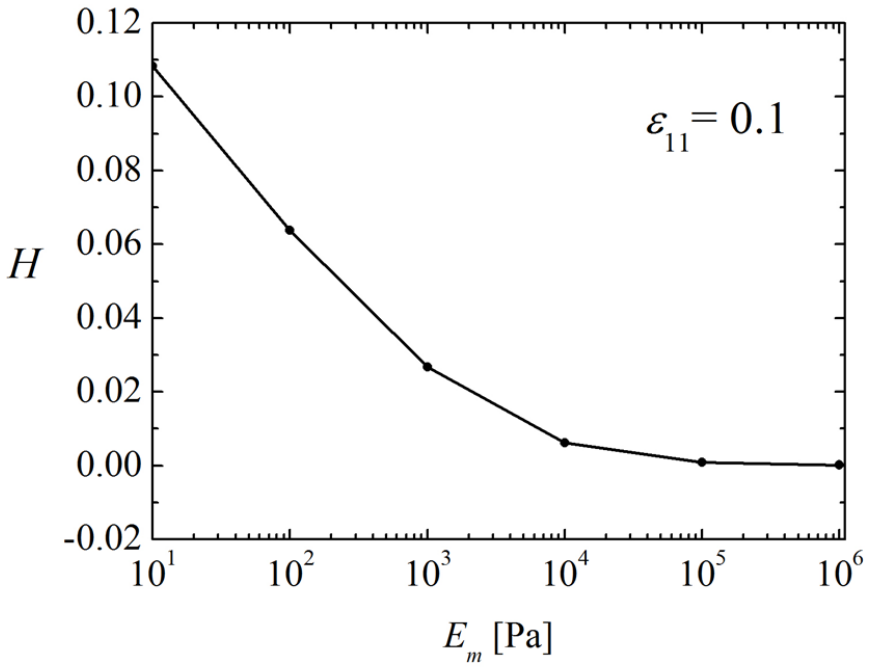

b)

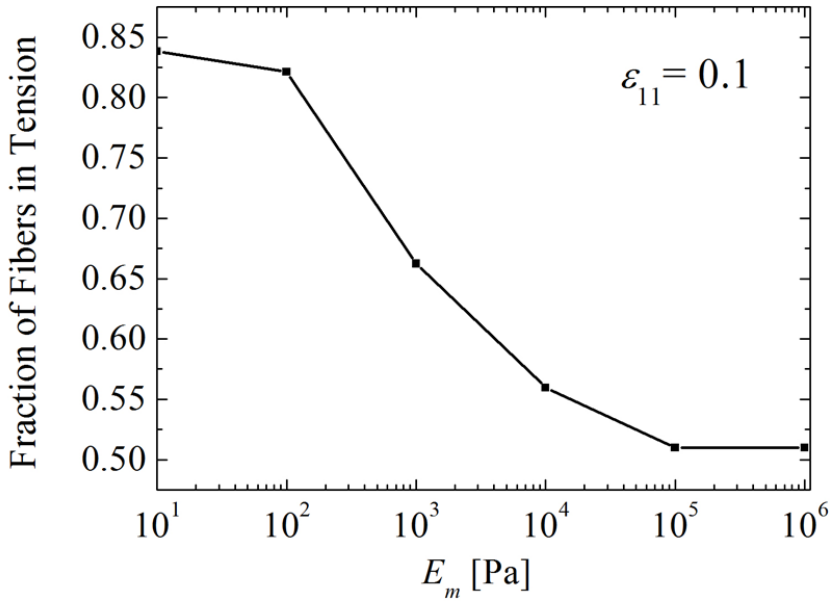

Figure 4.11: (a) Variation of the nonaffinity measure of Eq. (4.7) with the matrix elastic modulus E_m; (b) Fraction of fibers loaded in tension versus the matrix modulus E_m.

The fraction of fibers subjected to tension (Figure 4.11(b)) also tells the fact that fibers are forced to deform affinely in stiffer matrix. When E_m is large, the fraction is similar to that predicted by the affine model. For an effective Poisson ratio of 0.3 and affine deformation with strain $\varepsilon_{11} < 0.2$, 51% of the fibers are in tension. Our model predicts an asymptote to this limit (51%) when $E_m > 10^5$ Pa. For E_m=10 Pa, 84% of the fibers are in tension for all strains $\varepsilon_{11} < 0.2$. When deformation is more non-affine, the amount of relaxation is larger and hence more fibers are engaged in the tensile macroscopic deformation.

4.5 Effective elastic modulus and Poisson ratio of the composite

Evaluating the effective modulus, $\hat{E}$, and Poisson ratio, $\hat{\nu}$, of the network-matrix system yields additional insights. Figure 4.12(a) shows the computed $\hat{E}$ function of the matrix modulus for the network considered above, with E_fA_f= 8.168N and l_c/L = 0.104 (black squares). The effective modulus is always larger than E_m and increases with increasing matrix modulus. When E_m is so large that the matrix constrains the network to deform affinely ($E_m > 10^4$ Pa for this particular network), the effective modulus reaches a plateau. This plateau can be predicted by observing that in this regime both network and matrix deform affinely. Hence, the two components act as if they were in parallel in this limit. Specifically, $\hat{E}$ can be computed as the sum of E_m and an effective (fictitious) modulus of the affinely deforming network, E^n_{aff}.

Let us estimate E^n_{aff} by imposing an affine deformation on all network segments. For a uniaxial deformation with $\varepsilon_{11} = \epsilon$ and $\varepsilon_{22} = \varepsilon_{33} = -\nu_m\epsilon$, and assuming that the fiber orientation distribution is uniform, one may write the strain energy density of an affinely deforming network as [61, 62]:

$$\begin{aligned} u^n_{aff} &= \frac{1}{4}\rho E_f A_f \int_0^{\pi} \sin\varphi \left(\sqrt{(1-\upsilon_m\varepsilon)^2 \sin\varphi^2 + (1+\varepsilon)^2 \cos\varphi^2} - 1\right)^2 d\varphi \\ &= \frac{1}{4}\rho E_f A_f F(\varepsilon) \end{aligned} \tag{4.9}$$

where φ is the angle made by the direction of given fiber with the x_1 axis and $F(\epsilon)$ represents the integral. Requiring that this energy density equals $1/2E^n_{aff}\epsilon^2$, leads to

$$E_{aff}^{n} = \frac{1}{2}\rho E_f A_f F(\varepsilon)/\varepsilon^2 \tag{4.10}$$

Therefore, for large enough E_m, $\hat{E} = E_m + E_{aff}^{n}$. E_{aff}^{n} computed with the values of and $E_f A_f$ of this particular network is used to normalize the vertical axis in Figure 4.12(a). The close match with the numerical data in the plateau region provides support for the conjecture that the two components of the system act in parallel in this regime.

Figure 4.12(b) shows the effective Poisson ratio versus E_m (black squares). As the matrix stiffness increases, the Poisson ratio decreases and becomes equal to that of the matrix, i.e. $\hat{\nu} = \nu_m = 0.3$. For this particular type of network, the value corresponding to E_m = 10 Pa is $\hat{\nu} = 0.376$.

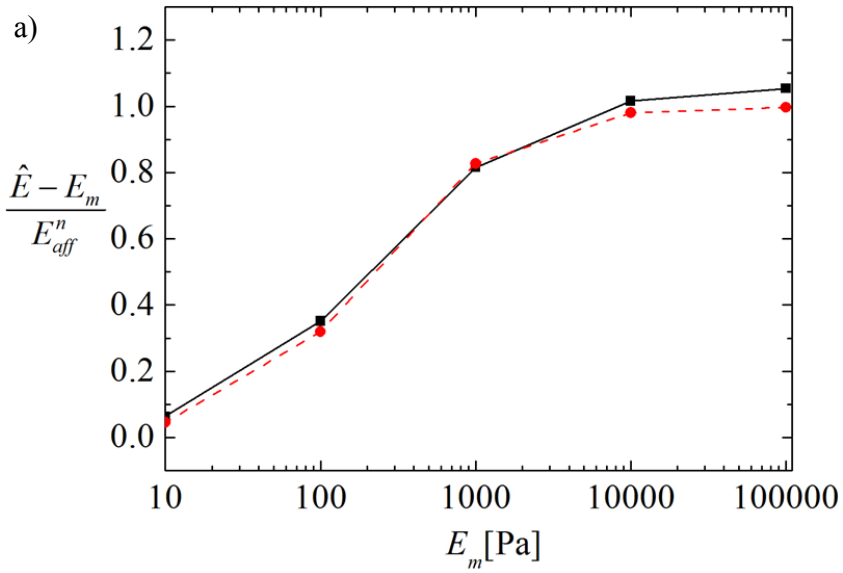

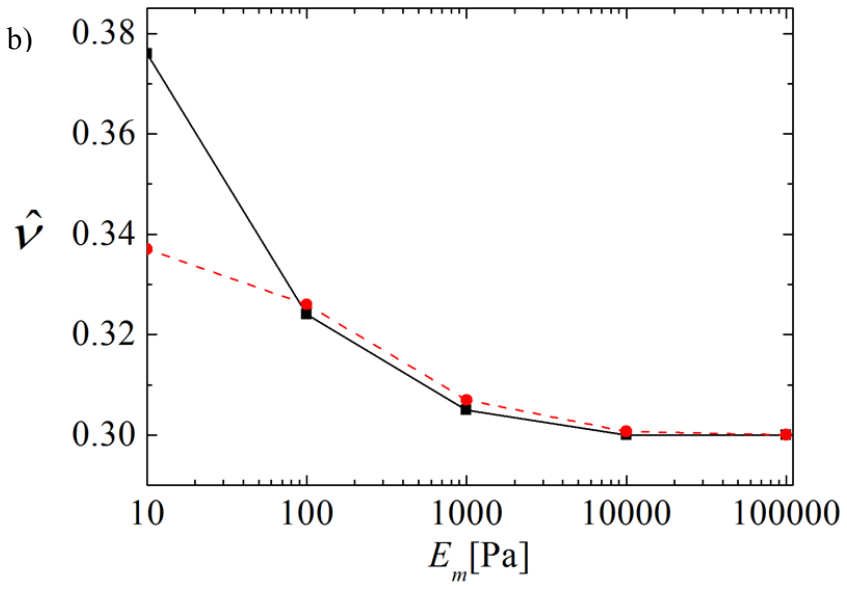

Figure 4.12: Variation of (a) the effective modulus of the network-matrix system, $\hat{E}$, and (b) the effective Poisson ratio, $\hat{\nu}$, with the matrix stiffness E_m. The vertical axis in (a) is normalized with the apparent modulus of the network constrained to deform affinely, provided by Eq. (4.10). The prediction of the mean field model of Eqs. (4.14) and (4.17) are shown by the dashed red lines in a) and b), respectively.

In order to estimate $\hat{E}$ for smaller values of E_m, for which the deformation is not affine, we develop a mean-field model based on the following simplified physical picture. Let us consider an isolated fiber tied to an infinite three-dimensional matrix. The system is deformed affinely by applying appropriate forces on the fiber (step 1). Note that no internal force acts on the matrix since the affine field matches the boundary conditions. The boundary of the model is then fixed and the interior is allowed to relax (step 2). In the equilibrium configuration the fiber changes length and the internal forces acting on it are the reactions of the forces acting on the matrix. Computing the energy of the system after relaxation allows evaluation of the effective stiffness of the network-matrix system based on an energetic approach similar to that used above for the affine deformation.

Two approximations are made when this approach is applied to the entire network. It is assumed that a) fibers relax independent of each other, and b) the interaction of the internal forces acting on the matrix due to fiber relaxation is neglected.

The strain energy density of the network during the relaxation of step 2 is computed by assuming that each fiber relaxes by a fraction β of its affine deformation of step 1. Then,

$$u^n(\beta) = \frac{1}{4}\rho E_f A_f (1-\beta)^2 F(\varepsilon) \tag{4.11}$$

The total energy stored in the matrix during the relaxation process is equal to the work performed by the internal forces. For each fiber, there are a pair of forces aligned with the fiber and acting on the matrix in opposite directions at the location of the two ends of the fiber. Under the assumption that these internal forces do not interact, the problem is equivalent to computing the work done by a force P acting on an infinite isotropic continuum, i.e. $P\delta/2$, where δ is the displacement of the point where P acts. Note that P is equal to the force stretching the bar and leading to the strain energy density of Eq. (4.11). Using the Green's function solution for an isotropic three-dimensional solid [64], one can write:

$$\frac{1}{2}P\delta = \frac{1}{2}\frac{E_m}{\alpha}\beta^2 L_f^2 \left(\sqrt{(1-\upsilon_m\varepsilon)^2 \sin\varphi^2 + (1+\varepsilon)^2 \cos\varphi^2}\, d\varphi - 1\right)^2 \tag{4.12}$$

In the Green's function solution, the energy stored in the body diverges and the solution predicts $\delta \to \infty$. To avoid this problem, an inner spherical cut-off of radius R_{min} needs to be taken in the vicinity of the force P. Parameter α in Eq. (4.12) depends on ν_m and R_{min} as $\alpha = h(\nu_m)/R_{min}$, and hence has units of inverse length. Function h reads $h(\nu) = (12\nu^3 - 10\nu^2 - 11\nu + 11)/(24\pi(1-\nu)^2)$. With this, the strain energy density stored in the matrix due to the relaxation of all (non-interacting) fibers is evaluated as:

$$u^m(\beta) = \frac{1}{4}\frac{E_m}{\alpha}\rho l_c \beta^2 F(\varepsilon) \tag{4.13}$$

Here we have taken $L_f = l_c$, the mean fiber length. Finding the minimum (with respect to β) of the total strain energy density $u(\beta) = u^n(\beta) + u^m(\beta)$ leads to $\beta = 1/(1+\eta)$, where $\eta = \frac{E_m}{E_f}\frac{l_c}{2\alpha A_f}$ is a non-dimensional parameter.

With this, one may compute the total strain energy stored and the effective modulus of the network-matrix system, which can be written as:

$$\hat{E} = E_m + E_{aff}^n \frac{\eta}{1+\eta} \tag{4.14}$$

Figure 4.13 shows the effective modulus of the network-matrix system, $(\hat{E} - E_m)/E_{aff}^n$, versus $\eta/(1+\eta)$ for several networks with different l_c/L (in the range 0.1 to 0.2) and E_fA_f (in the range 8.17 to 65.34 *N*) and embedded in matrices with E_m ranging from 10 to 10^4 Pa. The same value for parameter α (i.e. α = 4/3) is used for all curves. The data collapse on the line of slope 1, providing support to Eq. (4.14). The prediction of Eq. (4.14) is also added to Figure 4.12(a) and is seen to provide a good representation of the data.

The effective Poisson ratio of the material can be determined using the same model. Each fiber oriented at an angle φ with respect to the loading direction acts on the matrix with a force given by (after the relaxation of step 2):

$$P_\varphi = (1-\beta)E_f A_f \left(\sqrt{(1-\nu_m\varepsilon)^2 \sin\varphi^2 + (1+\varepsilon)^2 \cos\varphi^2} - 1\right) \tag{4.15}$$

which has a component in the direction perpendicular to the loading direction of magnitude $P_\varphi sin\varphi$. The planar density of fibers with orientation between φ and $\varphi + d\varphi$ crossing a plane parallel to the loading direction is $\rho_a = 1/2\,\rho\, sin^2\,\varphi\, d\varphi$, and the effective normal stress produced by these fibers perpendicular to the loading direction can be computed as $P_\varphi \rho_a \sin\varphi$. The average normal strain in the matrix in the x_2 direction due to the action of the network results by summing contributions of fibers with all orientations:

$$\begin{aligned}\bar{\varepsilon}_{22} &= \frac{1}{2E_m}(1-\beta)\rho E_f A_f \int_0^{\pi/2} \left(\sqrt{(1-\upsilon_m\varepsilon)^2 \sin\varphi^2 + (1+\varepsilon)^2 \cos\varphi^2} - 1\right) \sin^3\varphi d\varphi \\ &= \frac{1}{2E_m}(1-\beta)\rho E_f A_f G(\varepsilon)\end{aligned} \tag{4.16}$$

where $G(\epsilon)$ represents the integral. After adding the Poisson effect of the matrix, the effective Poisson ratio can be written:

$$\hat{\nu} = \nu_m + \lim_{\varepsilon\to 0} \left|\bar{\varepsilon}_{22}\right| / \varepsilon = \nu_m + \frac{1}{2}\frac{E_f}{E_m}\rho A_f \frac{\eta}{1+\eta} \lim_{\varepsilon\to 0} \frac{\left|G(\varepsilon)\right|}{\varepsilon} \tag{4.17}$$

The prediction of Eq. (4.17) is shown in Figure 4.11(b) with dashed line and is seen to be in good agreement with the values computed with the numerical model. The agreement is not as good at the lowest value of the matrix modulus.

It appears that, despite the approximations made, the simple model presented here captures the main features of the mechanics of this system. This indicates that, although the deformation is highly non-affine in systems with low E_m, the interaction of the internal forces is weak. Expression (4.14) allows for predicting the effective modulus of network composites over a broad range of system parameters.

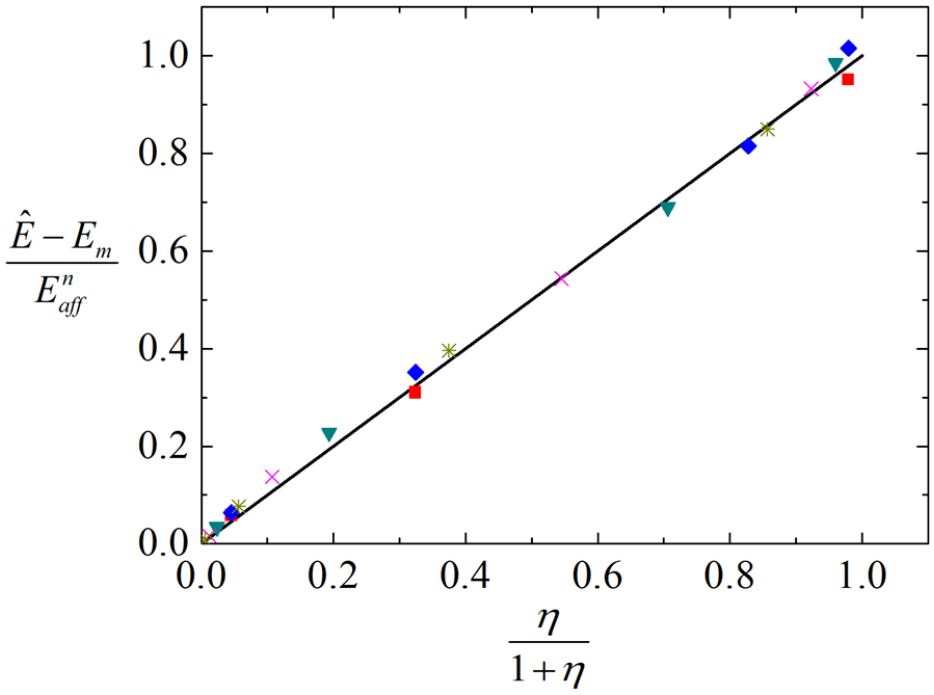

Figure 4.13: Variation of the normalized effective modulus of the network-matrix system with parameter η (Eq. (4.14)) for systems with various parameters.

4.6 Conclusion

The mechanical behavior of the RVE composite under tensile loading is investigated by applying both the parallel and coupled fiber-matrix models in this chapter.

In the nonlinear material constitutive model where individual fibers are represented as nonlinear members and the matrix is represented as neo-hookean material, anisotropic fiber networks are considered to approximate the preferred fiber alignment in the collagen-agarose co-gel. In terms of the overall RVE response (average stress, fiber

orientation, Poisson's ratio) and for these sets of system parameters, the coupled fiber-matrix model yields results consistent with those obtained using the parallel model which based upon superposition of matrix and network stresses. The detailed stress field in the composite RVE demonstrates a high degree of inhomogeneity, which cannot be captured by a parallel model.

To gain additional insight in the mechanics of cross-linked fiber embedded in matrix, a linear material model is also employed to represent both the fibers and matrix and the solution fields are examined for the case of an isotropic network. The presence of fiber network induces an inhomogeous stress distribution in matrix. The fiber-matrix composite has larger spatial stress variability in the case when the matrix stiffness is smaller. Also, in this case, the fiber network shrinks more in traverse directions and compresses the matrix, which leads to smaller normal stress (normalized by matrix Young's modulus) in the loading direction .

The network is constrained by the matrix to deform more affinely than it would in the absence of the embedding medium. This occurs due to internal forces applied by the matrix on the network. The reactions of these forces act on the matrix and introduce significantly heterogeneous stress and strain fields which are concentrated in the region of the network cross-links. Hence, damage is expected to nucleate at these concentration sites.

When matrix modulus is so large that the matrix constrains the network to deform affinely (Em > 104 Pa for this particular network), the effective modulus of the RVE composite reaches a plateau. The two components act as if they were in parallel in this limit.

A micromechanics model is developed to predict the effective modulus and Poisson's ratio of the RVE composite in terms of a set of system parameters. The result has yielded good agreement with numerical solution.

5. Volume averaging-based multiscale model

5.1 Introduction

The macroscopic behaviors of soft tissue are largely governed by the underlying microstructure. The volume averaging-based multiscale theory [48, 64] provides an effective way to directly link the mechanics of microstructure to the overall tissue mechanics. Hence, the proper mechanical modeling of microstructure is essential to the prediction of multiscale approach. As discussed in previous chapters, matrix plays an important role in affecting the network behaviors. Although the ultimate goal of the multiscale approach is to incorporate the contribution from both matrix and fiber network, for example, by employing the coupled fiber-matrix model at the representative volume element level, this chapter presents a general multiscale scheme to effectively incorporate the response of fiber network into the overall tissue mechanics.

In the present study, the microscale is represented as a three-dimensional interconnected fiber networks which transmit uniaxial forces through crosslinks. The crosslinked fiber network is contained in a representative volume element, which is constructed separately at each Gauss point of finite elements representing the macroscopic domain (Figure 5.1). In the multiscale scheme, the material constitutive model is not required at the macroscopic scale; instead, the local stress-strain response is obtained by solving a RVE boundary value problem at each Gauss point. After the RVE problem is solved, the averaged Cauchy stress is returned to the macroscopic scale to formulate nonlinear finite element equations.

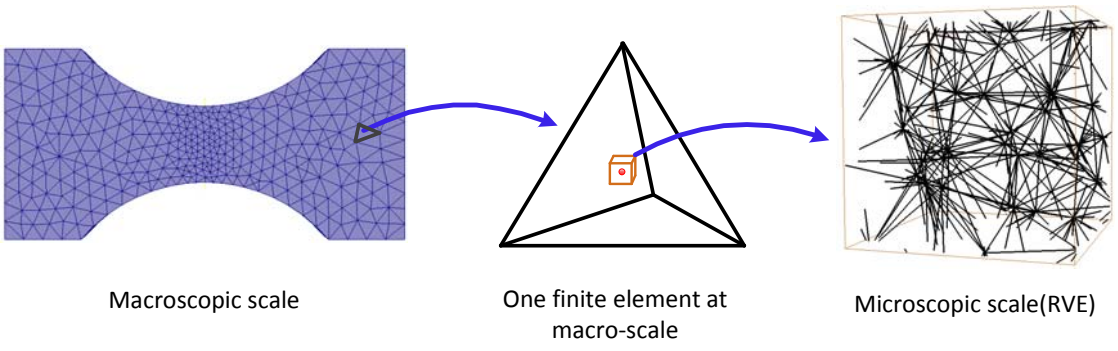

Figure 5.1: Illustration of the multiscale approach for soft tissue analysis.

5.2 Scale linking between macroscopic and microscopic scales

5.2.1 Downscaling – RVE boundary deformation

The RVE boundary deformation (i.e. displacements of fiber boundary crosslinks) is interpolated from the displacements of the eight vertices of the RVE, which in turn are determined from the calculated displacement field at the macroscopic scale (Figure 5.2). In the present model, the RVE is assumed to represent a material volume (a cube with side length a) of the physical domain. Since the coordinates of the Gauss point and physical length of RVE a (discussed in section 5.4) are known, the position vectors of the eight vertices of RVE $\boldsymbol{X}_i^{RVE}$ (i=1,2,…8) are easily obtained. By interpolating the displacement field at the macroscale, the displacement vector $\boldsymbol{U}_i^{RVE}$ of RVE vertex i is

$$\boldsymbol{U}_i^{RVE} = \sum_j N_j^{FE}(\boldsymbol{X}_i^{RVE})\boldsymbol{U}_j^{FE} \tag{5.1}$$

where $\boldsymbol{U}_j^{FE}$ is displacement vector of vertex j of the tetrahedron on which the RVE is constructed. The capital case indicates quantities are referred to the macroscopic scale.

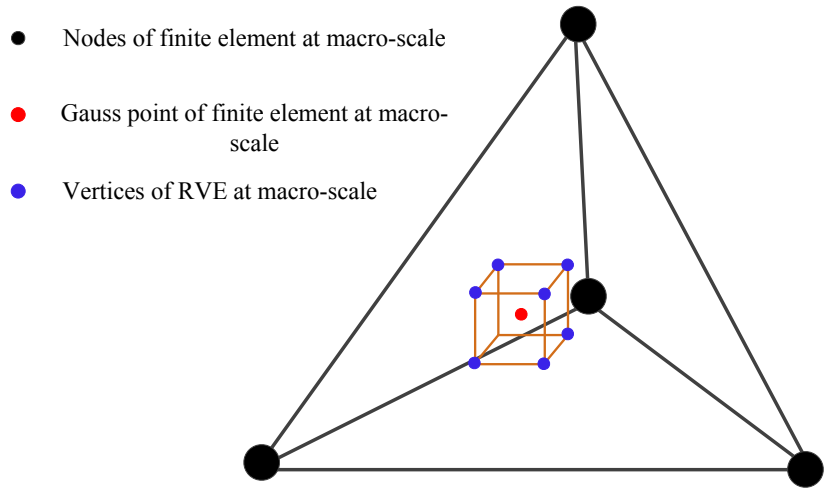

Figure 5.2: Representative volume element constructed on the Gauss point of a finite element.

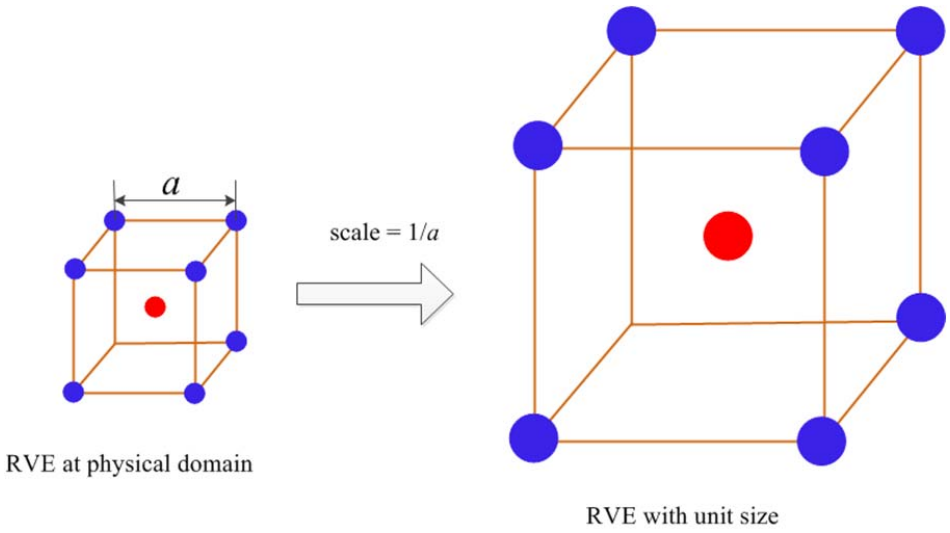

Figure 5.3: Scaling of the RVE from physical domain to microscopic scale.

5.2.2 Scaling

The RVE boundary displacements $\boldsymbol{U}_i^{RVE}$ calculated by Eq.(5.1) are referred to physical domain. When referring to the microscopic scale, the RVE boundary displacement $\boldsymbol{u}_i^{RVE}$ is scaled as (Figure 5.3),

$$\boldsymbol{u}_i^{RVE} = (\boldsymbol{U}_i^{RVE} - \boldsymbol{U}^{GP}) \cdot scale,\ i = 1,2,...,8 \tag{5.2a}$$

$$scale = 1/a \tag{5.2b}$$

where $\boldsymbol{U}^{GP}$ is the displacement vector of the Gauss point and the index i in Eq.(5.2a) represents the index of the RVE vertices. The displacement vector of Gauss point $\boldsymbol{U}^{GP}$ is calculated by interpolating the displacement field at the macroscopic scale, i.e.

$$\boldsymbol{U}^{GP} = \sum_j N_j^{FE}(\boldsymbol{X}^{GP})\boldsymbol{U}_j^{FE},\ j = 1,2,3,4 \tag{5.2c}$$

in which j is the index of vertices of the tetrahedron on which the Gauss point is constructed and $\boldsymbol{X}^{\mathrm{GP}}$ is the position vector of Gauss point at macroscale.

The displacements of network boundary crosslinks $\boldsymbol{u}_i^{bdy}$ are interpolated based on the displacements of the RVE eight vertices, i.e.

$$\boldsymbol{u}_i^{bdy} = \sum_j N_j^{RVE}(\boldsymbol{x}_i^{bdy})\boldsymbol{u}_j^{RVE},\ i = 1,2,...,N^{bdy},\ j = 1,2,...,8 \tag{5.3}$$

where $\boldsymbol{x}_j^{bdy}$ is the position vector of boundary crosslink j, N^{bdy} is the total number of fiber boundary crosslinks and N_j^{RVE} is the shape function of the cube.

5.2.3 Upscaling

After the RVE boundary value problem is solved, the average Cauchy stress (Eq.5.9) and force balance (Eq.5.10) are returned to the macroscale to formulate nonlinear finite element equations. The detailed nonlinear finite element formulation is provided in section 5 of Appendix A.

5.3 Governing equations

Three governing equations are required to formulate the multiscale model: a constitutive equation describing the force-elongation for the individual fiber; an equation relating microscopic Cauchy stress to the volume-averaged Cauchy stress at macroscopic scale and the equation for macroscopic stress balance [48].

- **Constitutive equation of individual fibers**

$$f^{fib} = \frac{E_f A}{B}(e^{B\varepsilon} - 1) \tag{5.4}$$

Parameters in Eq.(5.4) have the same definition as in Eq.(3.1).

- **Volume-averaged Cauchy stress at macroscale**

The volume-averaged Cauchy stress tensor, $\hat{\sigma}_{ij}$ at macroscopic scale is obtained from the microscopic stress tensor σ_{ij} by

$$\frac{1}{V}\left(\int_V \sigma_{ij} dV\right)_{,i} = \frac{1}{V}\left[\int_V \sigma_{ij,i} dV + \oint_{\partial V} \sigma_{ij} u_{k,j} n_k d\Gamma\right] \tag{5.5}$$

where V is the volume of the representative volume element (RVE).

By multiplying microscopic stress σ_{ij} with Kronecker delta δ_{ik},

$$\sigma_{ij} = \sigma_{kj}\delta_{ik} = \sigma_{kj} x_{i,k} \tag{5.6}$$

where x_i is the i^{th} component of position vector. Substituting Eq.(5.6) into Eq.(5.5) and applying the divergence theorem to transform the volume integral into surface integral,

$$\hat{\sigma}_{ij} = \frac{1}{V}\int_V \sigma_{kj} x_{i,k} dV = \frac{1}{V}\int_{\partial V} \sigma_{kj} x_i n_k d\Gamma - \frac{1}{V}\int_V \sigma_{kj,k} x_i dV \tag{5.7}$$

Applying the microscopic equilibrium, i.e. $\sigma_{kj,k} = 0$ and $t_j = \sigma_{kj} n_k$,

$$\hat{\sigma}_{ij} = \frac{1}{V} \int_{\partial V} \sigma_{kj} x_i n_k d\Gamma = \frac{1}{V} \int_{\partial V} x_i t_j d\Gamma \tag{5.8}$$

where t_j is the traction exerted on the boundaries of RVE. For a RVE consisting of only fibers, Eq.(5.8) is written as

$$\hat{\sigma}_{ij} = \frac{1}{V} \sum_{\substack{boundary \\ nodes}} x_i f_j \tag{5.9}$$

where f_j is the reaction force developed on the boundary node (crosslink) in j-direction. This equation could also be written in the virial formula, i.e

$$\hat{\sigma}_{ij} = \frac{1}{V} \sum_{\text{all nodes}} x_i f_j \tag{5.10}$$

which also holds because, since the internal nodes are in equilibrium, the terms corresponding to internal nodes do not contribute to the sum. Hence this sum is identical to that in Eq. (5.9).

- **Force balance for the macroscopic scale**

The momentum conservation equation at the macroscopic scale is derived by taking derivative with respect to x_i on both sides of Eq.(5.5) [65],

$$\left(\frac{1}{V} \int_V \sigma_{ij} dV \right)_{,i} = \frac{1}{V} \left(\int_V \sigma_{ij} dV \right)_{,i} + \left(\frac{1}{V} \right)_{,i} \int_V \sigma_{ij} dV \tag{5.11}$$

Using Leibnitz's rule, the first term on the right hand size of Eq.(5.11) is written as

$$\frac{1}{V} \left(\int_V \sigma_{ij} dV \right)_{,i} = \frac{1}{V} \left[\int_V \sigma_{ij,i} dV + \oint_{\partial V} \sigma_{ij} u_{k,i} n_k d\Gamma \right] \tag{5.12}$$

Again, applying Leibnitz's rule to the second term, we get

$$\left(\frac{1}{V} \right)_{,i} \int_V \sigma_{ij} dV = -\frac{1}{V^2} V_{,i} \int_V \sigma_{ij} dV = -\frac{\hat{\sigma}_{ij}}{V} \left(\int_V dV \right)_{,i} = -\frac{\hat{\sigma}_{ij}}{V} \oint_{\partial V} u_{k,i} n_k d\Gamma \tag{5.13}$$

Combing Eq.(5.12) and (5.13) and noting the microscopic balance (i.e. $\sigma_{ij,i} = 0$), the conservation of momentum at macroscopic scale is obtained

$$\begin{aligned} &\hat{\sigma}_{ij,i} - Q_j = 0 \\ &Q_j = \frac{1}{V} \int_{\partial V} (\sigma_{ij} - \hat{\sigma}_{ij}) u_{k,i} n_k d\Gamma \end{aligned} \tag{5.14}$$

where u_k is the displacement of the RVE boundary and n_k is the unit normal vector. The right hand side of Eq.(5.14) is due to the correlation between inhomogeneous displacement of RVE boundary and local inhomogeneities in the stress field. The macroscopic momentum balance equation given by Eq.(5.14) is solved by using finite element analysis.

5.4 Relating the microscopic scale to the macroscopic scale

In the volume-averaged multiscale model, the RVE is assumed to represent a material volume (a cube with side length a) at macroscale. The RVE scale is dimensionless and the side is of unit length in the undeformed configuration. This section reviews the conversion of the averaged stress calculated at the RVE scale to the physical scale [48].

At the RVE scale, the total fiber length in the RVE (1*1*1 cube) is L (dimensionless). Hence, the total fiber length in the macroscopic scale will be $L \cdot$a and the volume of fibers will be $A \cdot L \cdot$a. Therefore the volume fraction of fibers is

$$\theta_0 = \frac{ALa}{a^3} = \frac{AL}{a^2} \tag{5.15}$$

Solving a from Eq.(5.15),

$$a = \sqrt{\frac{LA}{\theta_0}} \tag{5.16}$$

Therefore, the RVE side length at physical domain is determined by the fiber radius and the volume fraction of the tissue. For the example shown in section 5.5, a is around 0.021mm.

Hence, the dimensional averaged stress $\hat{\sigma}_{ij}^{'}$ is calculated as

$$\hat{\sigma}_{ij}^{'} = \frac{1}{V^{'}} \sum_{\substack{boundary \\ nodes}} x_i^{'} f_j = \frac{1}{Va^3} \sum_{\substack{boundary \\ nodes}} a x_i f_j = \frac{1}{Va^2} \sum_{\substack{boundary \\ nodes}} x_i f_j \tag{5.17}$$

Substituting Eq.(5.16) into (5.17), the average Cauchy stress after conversion is

$$\hat{\sigma}_{ij}^{'} = \frac{\theta_0}{LA} \hat{\sigma}_{ij} \tag{5.18}$$

5.5 Example

A dogbone (shown in Figure 5.4) under 10% stretch is solved using the volume-averaging based multiscale model. The problem is solved in 5 load steps with 2% extension per step. The parameters in Eq.(5.4) are chosen as B=1.0, E_f=90Mpa, A=7.854E-09mm^2 corresponding to fiber radius 50nm, based on [66].

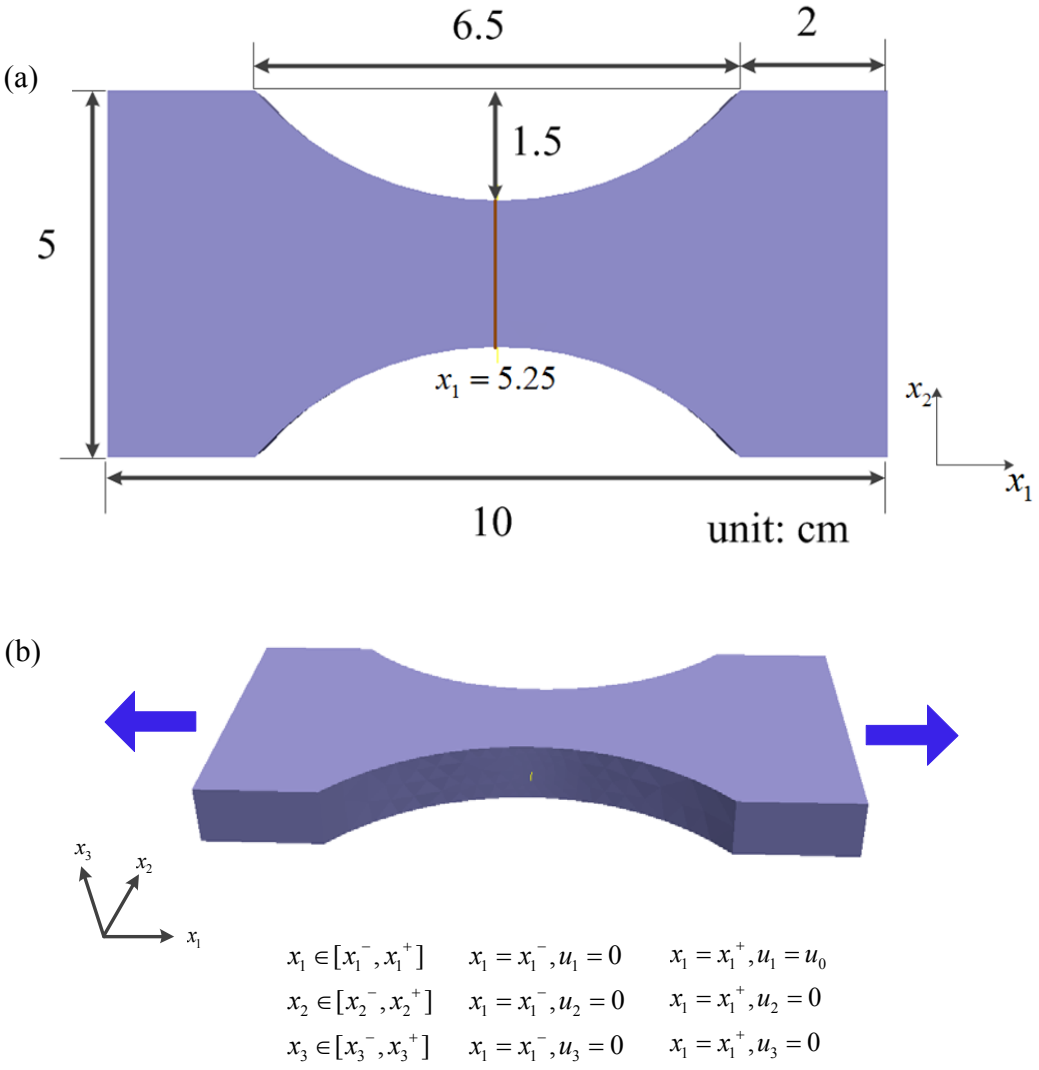

Figure 5.4: (a) Dimensions of the sample considered in this example and (b) Boundary conditions.

- **Network Properties**

Isotropic Delaunay fiber network are simulated in the representative volume element to obtain the local stress-strain response. The averaged coordination number (i.e. number of fibers emerging from given node) for this type of network is around 10, larger than the value of 6 required for stability. In the present multiscale soft tissue analysis, a Delaunay fiber network is randomly selected at each Gauss point out of a total of 30 fiber networks which have been stored in a database. Table 5.1 provides the statistical information of Delaunay fiber networks used in the multiscale simulation. Ω_{11}, Ω_{22} and Ω_{33} are fiber orientation parameter defined in Eq.(2.5) in chapter 2. For an ideal isotropic network, $\Omega_{11}=\Omega_{22}=\Omega_{33}=1/3$ and for a network with perfectly aligned fibers in the 1-direction, $\Omega_{11}=1$. Therefore, the networks used in the example are all isotropic networks before deformation.

Table 5.1 Statistical information of the simulated Delaunay fiber networks (total: 30)

	Number of crosslinks	Number of fibers	Ω_{11}	Ω_{22}	Ω_{33}
Mean	344.6	412.6	0.33288	0.336936	0.330184
Std. Dev	26.5	52.4	0.0184	0.0147	0.017

The geometric model shown in Figure 5.4 is discretized into a finite element mesh consisting of 8315 tetrahedrons and 1913 vertices. Linear shape functions are used at the macroscopic scale and there is one integration point per macro-element. The numbers of degree of freedom associated with the RVE computation and with the macroscopic scale model are 8,581,080(8315*344*3) and 5,739(1913*3) respectively. Therefore, the multiscale computation effort is substantial considering that the RVE boundary value problem is solved at every nonlinear iteration in each load step. The RVE computation is solved in parallel and the macroscopic computation is solved at the master processor based on [67]. Figure 5.5 shows the normal Cauchy stress distribution in 1-direction (loading direction), $\sigma_{11,}$ in the first and final load steps corresponding to 2% and 10% strain respectively. The fiber orientation parameter in 1-direction, Ω_{11}, evaluated by

averaging over elements intersecting the plane located at x_1=5.25 (shown by a vertical line in Figure 5.4) is shown in Figure 5.6. The orientation parameter increases with the applied strain from 0.33, which corresponds to the initial configuration, to 0.39 in the final configuration at 10% macroscopic uniaxial strain, which indicates that fibers are reorienting to the loading direction during applied extension.

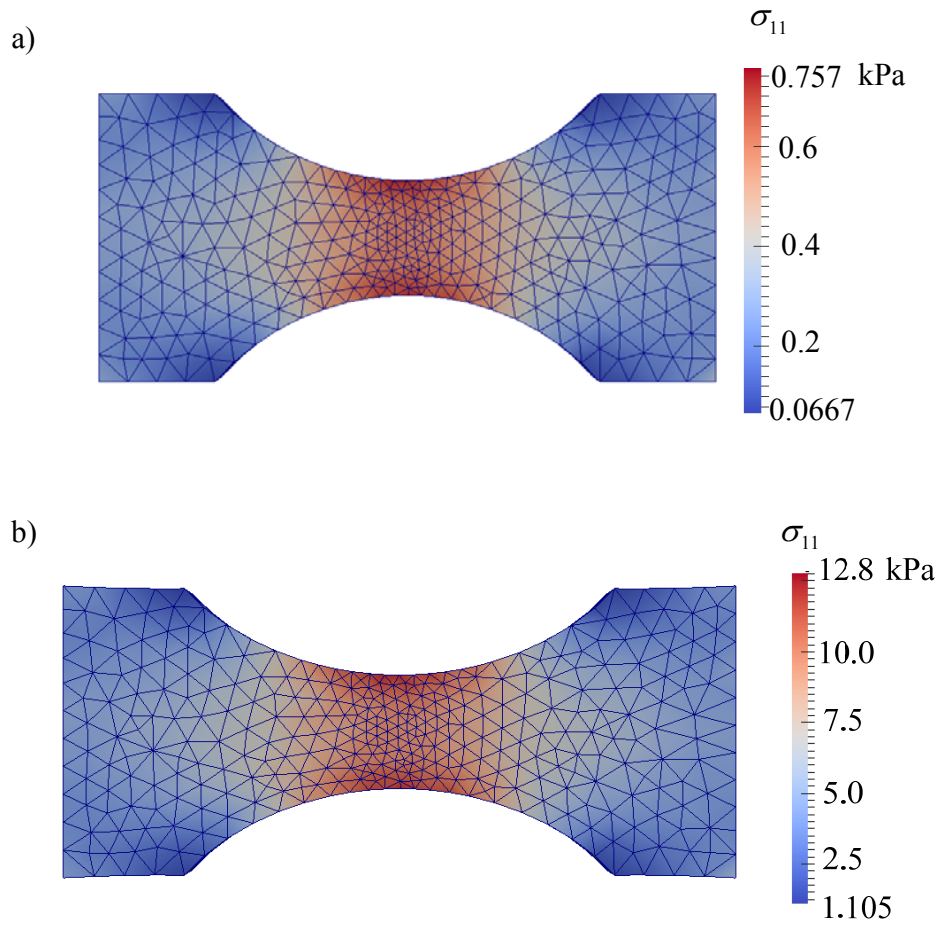

Figure 5.5: Normal Cauchy stress distribution in the load direction at (a) 2% strain (b) 10% strain.

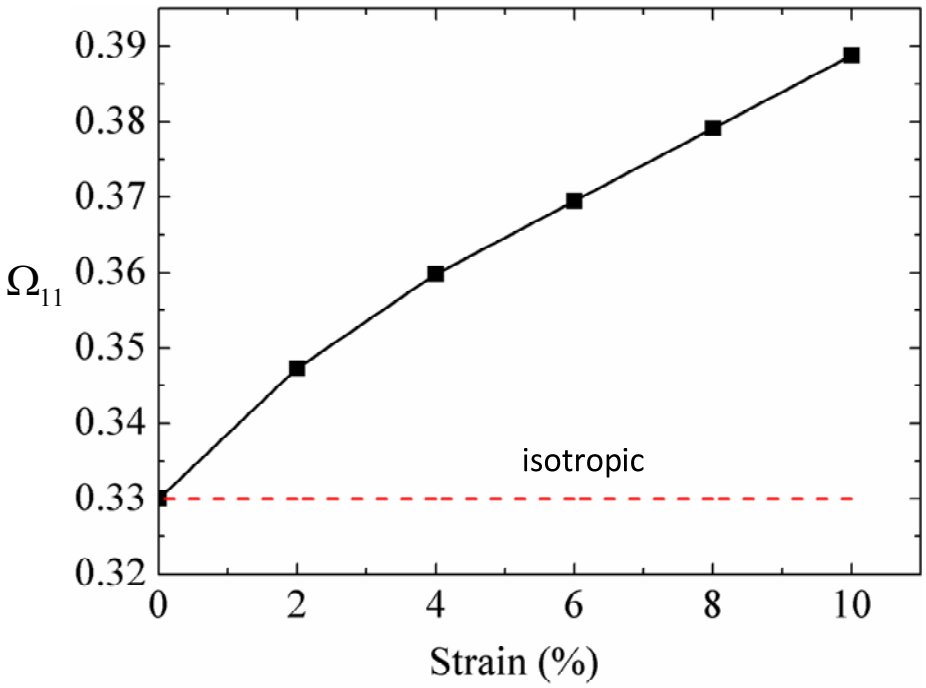

Figure 5.6: Variation of fiber orientation parameter computed along the vertical line shown in Figure 5.4(a) with the strain. The horizontal line indicates the value of the variable for the RVE with isotropic fiber orientation (state of the unloaded RVE).

5.6 Conclusion

A volume-averaging based multiscale model is presented in this chapter to directly link the microstructure mechanics to the macroscopic level. Delaunay fiber network is used to represent the collagen fiber network at the RVE level. Since two scale computations are involved, parallel computation is essential to improve computational efficiency. The dogbone example captures the fiber reorientation during the uniaxial extension at the macroscopic scale. Although the current multiscale model does not take the contribution of matrix into account, it presents a general computational scheme for future full development.

6. Conclusion and future work

6.1 Conclusion

The mechanical behavior of a three-dimensional cross-linked fiber network embedded in matrix is studied in this work. A finite element based coupled fiber-matrix model was developed to quantify the internal stress field and to explore interactions between the embedded fiber network and matrix.

In Chapter 2, we discussed the pre-processing step of the coupled fiber-matrix model, i.e. the non-manifold geometry creation for the model of the fiber network embedded in matrix, and multidimensional mesh generation. The geometry is based on a full representation of the network, which is generated using a Voronoi tessellation. The embedded fibers are represented as one-dimensional wire edges, therefore a non-manifold geometric topological representation is required. Topological adjacencies between geometric entities are specified by using Parasolid to create the non-manifold geometry. The multi-dimensional mesh with fibers meshed into one-dimensional mesh edges and matrix meshed into three-dimensional tetrahedrons are derived from the created non-manifold geometry. Both isotropic and gradedmeshes are generated for different purposes of finite element analysis. These developments make possible the creation of complex models of various types of networks embedded in matrix.

In Chapter 3, the formulation of the nonlinear equations representing the coupled fiber-matrix system was presented. Both geometric and material nonlinearities are taken into account in the analysis. Individual fibers are modeled as nonlinear trusses and the matrix material is modeled as compressible neo-Hookean material. The Newton's method is employed to solve the nonlinear equations and the tangential stiffness matrix and force vector are derived for the coupled fiber-matrix system. These developments make possible obtaining the non-linear solution for the models created using the methods presented in Chapter 2.

In Chapter 4, the mechanical behavior of the RVE composite under tensile loading was investigated by applying the coupled fiber-matrix model. In the nonlinear material constitutive model where individual fibers are represented as nonlinear trusses and the matrix is represented as neo-hookean material, anisotropic fiber networks are considered

to approximate the preferred fiber alignment in the collagen-agarose co-gel. In terms of the overall RVE response (average stress, fiber orientation, Poisson's ratio), the coupled fiber-matrix model yields results consistent with those obtained using the parallel model which based upon the superposition of matrix and network stresses. The detailed stress field in the composite RVE demonstrates a high degree of inhomogeneity, which cannot be captured by a parallel model.

To gain additional insight in the mechanics of cross-linked fiber embedded in matrix, a linear material model is also employed to represent both the fibers and matrix, and the solution fields are examined for the case of an isotropic network. The presence of the fiber network induces an inhomogeous stress distribution in matrix. The fiber-matrix composite has larger spatial stress variability in the case when the matrix stiffness is smaller. Also, in this case, the fiber network shrinks more in traverse directions and compresses the matrix, which leads to smaller normal stress (normalized by matrix Young's modulus) in the loading direction .

The network is constrained by the matrix to deform more affinely than it would in the absence of the embedding medium. This occurs due to internal forces applied by the matrix on the network. The reactions of these forces act on the matrix and introduce significantly heterogeneous stress and strain fields which are concentrated in the region of the network cross-links. Hence, damage is expected to nucleate at these concentration sites. When the matrix modulus is increased enough the matrix constrains the network to deform affinely ($E_m > 10^4$ Pa for this particular network), the effective modulus of the RVE composite reaches a plateau. The two components act as if they were in parallel in this limit and the parallel model described at the beginning of Chapter 4 becomes exact.

A micromechanics model is developed to predict the effective modulus and Poisson's ratio of the RVE composite in terms of a set of system parameters. The result has yielded good agreement with numerical results obtained by the coupled fiber-matrix model.

In Chapter 5, a volume averaging based multiscale model was presented to effectively link the microstructure mechanics to the overall tissue mechanics. In the multiscale scheme, the material constitutive model is not required at the macroscopic scale and the local stress-strain response is obtained by solving a RVE boundary value

problem at each Gauss point of the continuum model. The RVE is similar to that considered in Chapter 4. After the RVE problem is solved, the averaged Cauchy stress is returned to the macroscopic scale to formulate nonlinear finite element equations. By applying the multiscale approach, fiber reorientation occurring in the tissue microstructure was captured in the dogbone uniaxial extension test. This development demonstrates that the methodology developed can be applied to real systems and sets the stage for future developments and application to more complicated cases.

6.2 Future work

In the present work, fibers are modeled as one-dimensional straight edges embedded in three-dimensional matrix. However, individual collagen fibers are seen randomly crimped, as observed in photomicrographs of tissue samples. Although in the current work the effect of fiber crimp is incorporated by considering an exponential form for the material constitutive model of single fibers, there is no explicit modeling of the waviness of fibers. Under the current framework of the coupled model, once the wavy form of individual fibers is determined, such structural information could be directly modeled by creating a non-manifold geometry with embedded one-dimensional curves representing crimped fibers.

The sliding between embedded fibers and matrix is not taken into account. In the current work, embedded fibers and adjacent matrix are bonded by shared mesh vertices along fibers, which prevents the relative motion between the two components. Additional degree of freedoms could be added between the elements representing fibers and matrix to reduce the constraint of motion between the two components.

The results presented in chapter 4 are obtained with a representative volume element of a given size. However, the reported results, such as the effective elastic modulus of the composite, are dependent on the size of the RVE. Therefore the minimum size of the RVE beyond which size effects are negligible and the response becomes representative for the larger scale needs to be determined. When the RVE has a minimum size, the apparent stiffness tensor becomes independent of the applied boundary conditions and the variance of elastic properties for a set of microstructure realizations is sufficiently small.

For the present sequential multiscale analysis, the issue of the RVE size relative to the macro-scale finite element size is still under discussion. The principle of scale separation (the ratio between the length scale of the macroscopic scale and that of microscopic scale needs to be larger than one or two orders of magnitude) may not be satisfied in situations where the mesh needs to be refined (for example in regions of large stress gradient such as at crack tips. For example, in the current case, the RVE size is around 0.02mm and the minimum edge length of elements at macro-scale is 0.83mm, resulting in a ratio of 1/40 between the length scale of microscopic and macroscopic scales. This indicates that for those refined regions, the RVE may be too large to represent a local mechanical response for the macroscopic scale. Concurrent multiscale model is desirable in such cases when the scales are strongly coupled. In the concurrent model, the problem domain is often decomposed into different regions characterized by difference scales and physics. For example, in the present analysis, those refined mesh regions are considered dominated by the response of the smaller scale.

The internal stress distribution predicted by the coupled fiber-matrix model has not been verified by the experimental values. Novel experimental techniques (e.g. 3D traction force microscopy [59]) may allow the future estimation of internal stress fields in multicomponent tissues and more complete testing of this coupled microstructural model.

7. Reference

[1] D. L. Butler, S. A. Goldstein, R. E. Guldberg, X. E. Guo, R. Kamm, C. T. Laurencin, L. V. McIntire, V. C. Mow, R. M. Nerem, R. L. Sah, L. J. Soslowsky, R. L. Spilker, and R. T. Tranquillo, "The impact of biomechanics in tissue engineering and regenerative medicine," *Tissue Eng.*, vol. 15, p. 477, Dec. 2009.

[2] D. L. Butler, S. A. Goldstein, and F. Guilak, "Functional tissue engineering: The role of biomechanics," *J. Biomech. Eng.*, vol. 122, p. 570, Dec. 2000.

[3] U. A. Stock and J. P. Vacanti, "Tissue engineering: Current state and prospects," *Annu. Rev. Med.*, vol. 52, p. 443, Feb. 2001.

[4] J. Lemaitre, *Handbook of Materials Behavior Models: Nonlinear Models and Properties*, 2nd ed. San Diego, CA: Academic Press, 2001.

[5] S. P. Lake and V. H. Barocas, "Mechanical and structural contribution of non-fibrillar matrix in uniaxial tension: A collagen-agarose co-gel model.," *Ann. Biomed. Eng.*, vol. 39, p. 1891, Jul. 2011.

[6] J. D. Humphrey, "Continuum biomechanics of soft biological tissues," *Proc. R. Soc. London. Ser. A*, vol. 459, p. 3, Jan. 2003.

[7] Y. C. Fung, "Elasticity of soft tissues in simple elongation," *Am. J. Physiol.*, vol. 213, p. 1532, Dec. 1967.

[8] J. D. Humphrey, R. K. Strumpf, and F. C. Yin, "Determination of a constitutive relation for passive myocardium: II. Parameter estimation," *J. Biomech. Eng.*, vol. 112, p. 340, Aug. 1990.

[9] C. O. Horgan and G. Saccomandi, "A description of arterial wall mechanics using limiting chain extensibility constitutive models," *Biomech. Model. Mechanobiol.*, vol. 1, p. 251, Apr. 2003.

[10] J. D. Humphrey, "Mechanics of the arterial wall: Review and directions," *Crit. Rev. Biomed. Eng.*, vol. 23, p. 1, Jan. 1995.

[11] Y. Lanir, "A structural theory for the homogeneous biaxial stress-strain relationships in flat collagenous tissues," *J. Biomech.*, vol. 12, p. 423, Jun. 1979.

[12] W. F. Decraemer, M. A. Maes, and V. J. Vanhuyse, "An elastic stress-strain relation for soft biological tissues based on a structural model," *J. Biomech.*, vol. 13, p. 463, Jun. 1980.

[13] M. S. Sacks, “Incorporation of experimentally-derived fiber orientation into a structural constitutive model for planar collagenous iissues,” *J. Biomech. Eng.*, vol. 125, p. 280, Apr. 2003.

[14] D. H. Cortes, S. P. Lake, J. A. Kadlowec, L. J. Soslowsky, and D. M. Elliott, “Characterizing the mechanical contribution of fiber angular distribution in connective tissue: Comparison of two modeling approaches,” *Biomech. Model. Mechanobiol.*, vol. 9, p. 651, Oct. 2010.

[15] H. P. Wagner and J. D. Humphrey, “Differential passive and active biaxial mechanical behaviors of muscular and elastic arteries: Basilar versus common carotid,” *J. Biomech. Eng.*, vol. 133, p. 051009, May 2011.

[16] Y. Hollander, D. Durban, X. Lu, G. S. Kassab, and Y. Lanir, “Experimentally validated microstructural 3D constitutive model of coronary arterial media,” *J. Biomech. Eng.*, vol. 133, p. 031007, Mar. 2011.

[17] P. H. Kao, S. R. Lammers, L. Tian, K. Hunter, K. R. Stenmark, R. Shandas, and H. J. Qi, “A microstructurally driven model for pulmonary artery tissue.,” *J. Biomech. Eng.*, vol. 133, p. 051002, May 2011.

[18] A. L. F. Soares, M. Stekelenburg, and F. P. T. Baaijens, “Remodeling of the collagen fiber architecture due to compaction in small vessels under tissue engineered conditions,” *J. Biomech. Eng.*, vol. 133, p. 071002, Jul. 2011.

[19] N. T. Jacobs, D. H. Cortes, E. J. Vresilovic, and D. M. Elliott, “Biaxial tension of fibrous tissue: Using finite element methods to address experimental challenges arising from boundary conditions and anisotropy,” *J. Biomech. Eng.*, vol. 135, p. 021004, Feb. 2013.

[20] G. A. Ateshian, V. Rajan, N. O. Chahine, C. E. Canal, and C. T. Hung, “Modeling the matrix of articular cartilage using a continuous fiber angular distribution predicts many observed phenomena,” *J. Biomech. Eng.*, vol. 131, p. 061003, Jun. 2009.

[21] T. C. Gasser, R. W. Ogden, and G. A. Holzapfel, “Hyperelastic modelling of arterial layers with distributed collagen fibre orientations,” *J. R. Soc. Interface*, vol. 3, p. 15, Mar. 2006.

[22] A. D. Freed, D. R. Einstein, and I. Vesely, “Invariant formulation for dispersed transverse isotropy in aortic heart valves: An efficient means for modeling fiber splay,” *Biomech. Model. Mechanobiol.*, vol. 4, p. 100, Nov. 2005.

[23] R. C. Picu, “Mechanics of random fiber networks—a review,” *Soft Matter*, vol. 7, p. 6768, May 2011.

[24] K. L. Billiar, M. S. Sacks, and C. Gables, "A method to quantify the fiber kinematics of planar tissues under biaxial stretch," *J. Biomech.*, vol. 30, p. 753, Jul. 1997.

[25] K. K. Brewer, H. Sakai, A. M. Alencar, A. Majumdar, S. P. Arold, K. R. Lutchen, E. P. Ingenito, and B. Suki, "Lung and alveolar wall elastic and hysteretic behavior in rats: Effects of in vivo elastase treatment," *J. Appl. Physiol.*, vol. 95, p. 1926, Nov. 2003.

[26] P. L. Chandran and V. H. Barocas, "Affine versus non-affine fibril kinematics in collagen networks: Theoretical studies of network behavior," *J. Biomech. Eng.*, vol. 128, p. 259, Apr. 2006.

[27] D. A. Head, A. J. Levine, and F. C. MacKintosh, "Deformation of cross-linked semiflexible polymer networks," *Phys. Rev. Lett.*, vol. 91, p. 108102, Sep. 2003.

[28] D. A. Head, A. J. Levine, and F. C. MacKintosh, "Distinct regimes of elastic response and deformation modes of cross-linked cytoskeletal and semiflexible polymer networks," *Phys. Rev. E*, vol. 68, p. 061907, Dec. 2003.

[29] H. Hatami-Marbini and R. C. Picu, "Scaling of nonaffine deformation in random semiflexible fiber networks," *Phys. Rev. E*, vol. 77, p. 062103, Jun. 2008.

[30] P. R. Onck, T. Koeman, T. van Dillen, and E. van der Giessen, "Alternative explanation of stiffening in cross-linked semiflexible networks," *Phys. Rev. Lett.*, vol. 95, p. 178102, Oct. 2005.

[31] J. Liu, G. H. Koenderink, K. E. Kasza, F. C. MacKintosh, and D. A. Weitz, "Visualizing the strain field in semiflexible polymer networks: Strain fluctuations and nonlinear rheology of f-actin gels," *Phys. Rev. Lett.*, vol. 98, p. 198304, May 2007.

[32] F. LeonForte, A. Tanguy, J. P. Wittmer, and J. L. Barrat, "Continuum limit of amorphous elastic bodies II: Linear response to a point source force," *Phys. Rev. B*, vol. 70, p. 014203, Jul. 2004.

[33] B. A. DiDonna and T. C. Lubensky, "Nonaffine correlations in random elastic media," *Phys. Rev. E*, vol. 72, p. 066619, Dec. 2005.

[34] G. A. Holzapfel, T. C. Gasser, and R. W. Ogden, "A new constitutive framework for arterial wall mechanics and a comparative study of material models," *J. Elast.*, vol. 61, p. 1, Jul. 2000.

[35] N. J. B. Driessen, C. V. C. Bouten, and F. P. T. Baaijens, "A Structural Constitutive Model For Collagenous Cardiovascular Tissues Incorporating the Angular Fiber Distribution," *J. Biomech. Eng.*, vol. 127, p. 494, Jun. 2005.

[36] H. Tang, M. J. Buehler, and B. Moran, "A constitutive model of soft tissue: From nanoscale collagen to tissue continuum," *Ann. Biomed. Eng.*, vol. 37, p. 1117, Jun. 2009.

[37] T. Nagel and D. J. Kelly, "Remodelling of collagen fibre transition stretch and angular distribution in soft biological tissues and cell-seeded hydrogels.," *Biomech. Model. Mechanobiol.*, vol. 11, p. 325, Mar. 2012.

[38] K. M. Quapp and J. A. Weiss, "Material characterization of human medial collateral ligament," *J. Biomech. Eng.*, vol. 120, p. 757, Dec. 1998.

[39] H. L. Guerin and D. M. Elliott, "Quantifying the contributions of structure to annulus fibrosus mechanical function using a nonlinear, anisotropic, hyperelastic model," *J. Orthop. Res.*, vol. 24, p. 508, Apr. 2007.

[40] A. C. Abraham, J. T. Moyer, D. F. Villegas, G. M. Odegard, and T. L. Haut Donahue, "Hyperelastic properties of human meniscal attachments," *J. Biomech.*, vol. 44, p. 413, Feb. 2011.

[41] D. H. Cortes and D. M. Elliott, "Extra-fibrillar matrix mechanics of annulus fibrosus in tension and compression," *Biomech. Model. Mechanobiol.*, vol. 11, p. 781, Jul. 2012.

[42] D. R. Wagner and J. C. Lotz, "Theoretical model and experimental results for the nonlinear elastic behavior of human annulus fibrosus," *J. Orthop. Res.*, vol. 22, p. 901, Jul. 2004.

[43] X. Q. Peng, Z. Y. Guo, and B. Moran, "An anisotropic hyperelastic constitutive model with fiber-matrix shear interaction for the human annulus fibrosus," *J. Appl. Mech.*, vol. 73, p. 815, May 2005.

[44] G. D. O'Connell, H. L. Guerin, and D. M. Elliott, "Theoretical and uniaxial experimental evaluation of human annulus fibrosus degeneration," *J. Biomech. Eng.*, vol. 131, p. 111007, Nov. 2009.

[45] S. P. Lake, M. F. Hadi, V. K. Lai, and V. H. Barocas, "Mechanics of a fiber network within a non-fibrillar matrix: Model and comparison with collagen-agarose co-gels," *Ann. Biomed. Eng.*, vol. 40, p. 2111, Oct. 2012.

[46] E. A. Sander, T. Stylianopoulos, R. T. Tranquillo, and V. H. Barocas, "Image-based multiscale modeling predicts tissue-level and network-level fiber reorganization in stretched cell-compacted collagen gels," *Proc. Natl. Acad. Sci. U. S. A.*, vol. 106, p. 17675, Oct. 2009.

[47] S. Nachtrab, S. C. Kapfer, C. H. Arns, M. Madadi, K. Mecke, and G. E. Schröder-Turk, "Morphology and linear-elastic moduli of random network solids," *Adv. Mater.*, vol. 23, p. 2633, Jun. 2011.

[48] T. Stylianopoulos and V. H. Barocas, "Volume-averaging theory for the study of the mechanics of collagen networks," *Comput. Methods Appl. Mech. Eng.*, vol. 196, p. 2981, Jun. 2007.

[49] K. J. Weiler, *Topological structures for geometric modeling*. Ph.D dissertation, Dept. Comput. Sci., Rensselaer Polytechnic Institute, Troy, NY, 1986.

[50] Siemens Product Lifecycle Management Software, Inc., "Parasolid." [Online]. Available: http:www.plm.automation.siemens.com/, [Accessed Dec. 6. 2013].

[51] Simmetrix Inc., "The simulation modeling suite." [Online]. Available: http://www.simmetrix.com/, [Accessed Dec. 6. 2013].

[52] L. Zhang, S. P. Lake, V. K. Lai, C. R. Picu, V. H. Barocas, and M. S. Shephard, "A coupled fiber-matrix model demonstrates highly inhomogeneous microstructural interactions in soft tissues under tensile load," *J. Biomech. Eng.*, vol. 135, p. 011008, Jan. 2013.

[53] G. A. Holzapfel, *Nonlinear Solid Mechanics: A Continuum Approach for Engineering,*1st ed. West Sussex, England: Wiley, 2000.

[54] K. J. Bathe, *Finite Element Procedures,* 1st ed. Upper Saddle River, New Jersey: Prentice Hall, 1996.

[55] P. Wriggers, *Nonlinear Finite Element Methods,* 1st ed. Hannover, Germany: Springer, 2008.

[56] T. Belytschko, W. K. Liu and B. Moran, *Nonlinear Finite Elements for Continua and Structures,* 1st ed. West Sussex, England: Wiley, 2000.

[57] A. F. Bower, *Applied Mechanics of Solids,* 1st ed. Boca Raton, Florida: CRC Press, 2009.

[58] L. Zhang, S. P. Lake, V. H. Barocas, M. S. Shephard, and R. C. Picu, "Cross-linked fiber network embedded in an elastic matrix," *Soft Matter*, vol. 9, p. 6398, Jul. 2013.

[59] C. Franck, S. A. Maskarinec, D. A. Tirrell, and G. Ravichandran, "Three dimensional traction force microscopy: A new tool for quantifying cell-matrix interactions," *PLoS One*, vol. 6, p. e17833, Mar. 2011.

[60] M. Kellomäki, J. Åström, and J. Timonen, "Rigidity and dynamics of random spring networks," *Phys. Rev. Lett.*, vol. 77, p. 2730, Sep. 1996.

[61] A. Shahsavari and R. C. Picu, "Model selection for athermal cross-linked fiber networks," *Phys. Rev. E*, vol. 86, p. 011923, Jul. 2012.

[62] D. H. Lee and G. A. Carnaby, "Compressional energy of the random fiber assembly, part I: Theory," *Text. Res. J.*, vol. 62, p. 185, Apr. 1992.

[63] X. F. Wu and Y. A. Dzenis, "Elasticity of planar fiber networks," *J. Appl. Phys.*, vol. 98, p. 093501, Nov. 2005.

[64] A. E. H. Love, *A Treatise on the Mathematical Theory of Elasticity,* 4th ed. Mineola, New York: Dover, 2011.

[65] P. L. Chandran and V. H. Barocas, "Deterministic material-based averaging theory model of collagen gel micromechanics," *J. Biomech. Eng.*, vol. 129, p. 137, Apr. 2007.

[66] P. L. Chandran, T. Stylianopoulos, and V. H. Barocas, "Microstructure-based, multiscale modeling for the mechanical behavior of hydrated fiber networks," *Multiscale Model. Simul.*, vol. 7, p. 22, Apr. 2008.

[67] X. J. Luo, T. Stylianopoulos, V. H. Barocas, and M. S. Shephard, "Multiscale computation for bioartificial soft tissues with complex geometries," *Eng. Comput.*, vol. 25, p. 87, Sep. 2008.

Appendix A

Documentation on finite element code of multiscale soft tissue analysis

1. Flow chart of the multiscale code

The flow chart of the multiscale soft tissue computation is shown in Figure A.1, which employs an incremental-iterative approach (details in Chapter 3.). The only difference from the standard approach is that microscale computation is executed at each nonlinear iteration before computing the tangential stiffness matrix and force vector at the macroscale to provide averaged stress and stress derivative on each Gauss point. In the following flow chart, the micro-scale computation is denoted as 'compute RVEs'.

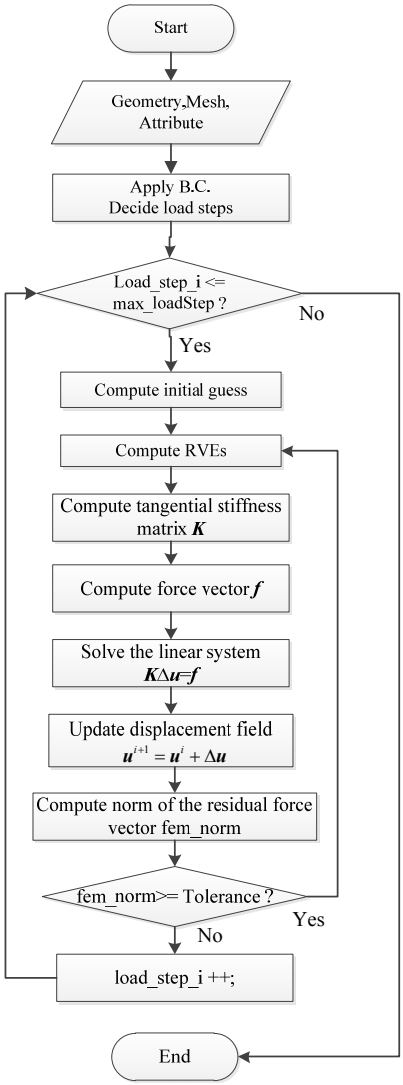

Figure A.1 flow chart of the multi-scale code

2. Interface functions passing information through scales

The multiscale analysis code consists of two scale computation. Each scale is treated as a C++ object with carefully designed member functions. The macro-scale computation is represented as class 'NonLinTissue'; the micro-scale computation is represented as class 'RepresentVolElem'. The two scales communicate through interfaces functions. Class definitions with essential member functions are provided in section 4.

2.1 Interface functions related to macro-scale to micro-scale information passing

The information passed from macroscale to microscale includes the nodal displacements of macro element on which the representative volume element (RVE) is constructed.

Related interface functions are:

```
// Retrieve the nodal displacements of mesh entity 'pEntity' and write into an array of   double
Void NonLinTissue :: retrieveCoordsDisp(pEntity, double *);

// Pass the nodal displacement of macro element to its RVE
void RepresentVolElem :: setupCoordsDisp(double *coordDisp);
```

2.2 Interface functions related to micro-scale to macro-scale information passing

The information passed from microscale to macroscale includes: (1) averaged stress (2) body force (3) the derivative of averaged stress with respect to the nodal displacement of macro element on which RVE is constructed.

Related interface functions are:

```
// Compute the averaged stress of the RVE and write it in the array 'vstress'
void RepresentVolElem :: calc_stress(double fvec[],double vstress[], int pas);

// Compute the unbalanced body force (referred as Q term in Chapter 5)
void RepresentVolElem :: avgvolstress(double fvec[],double vstress[],double loc_vastrx[], double
loc_vastry[],double loc_vastrz[],double vol,double coords_loc[], int nfe, int pas,double
init_coords_loc[],double fem_res_norm);
```

// Compute the derivative of averaged stress with respect to nodal displacement of macro element

void RepresentVolElem :: calc_femjacob_newmethod(double dSdx[],int pas,double vol,double dvol[],double vstress[],int tag,double init_coords_loc[],int nfe,int iter,int nmesh);

// Retrieve the averaged stress, body force(Q term) and stress derivative from the RVE on mesh entity pEntity;

SCOREC_Core::RVEInfo * NonLinTissue :: retrieveMatLawFromRVE (pEntity, int);

3. Pseudo code on the multiscale software design

The pseudo code for the mutilscale analysis is given below. In the pseudo code, 'NLT' represents the object with class type as 'NonLinTissue'(macroscale); 'RVE' represents the object with class type 'RepresentVolElem'(microscale). The first piece is the main flow described in Figure 1; the second piece represents microscale computation.

(1) Pseudo code of multiscale analysis

```
Input: geometry,mesh and attribute
// apply dirichlet boundary conditions
NLT->dirichlet();
// set up convergence tolerance
NLT->setConvTol();
Set current load step equal to 0
Set current nonlinear iteration equal to 0
Loop current load step = 0 to maximum load step
        If current nonlinear iteration equal to 0
        // set up and apply initial guess to the current displacement field
        NLT-> SetInitialGuess();
        Do {
                // retrieve the updated nodal displacement at each macro element to deform RVE
                NLT->retrieveCoordsDisp();
                // compute all RVEs driven by macro deformation field
                NLT->computeRVEs();
                // retrieve averaged stress and stress derivative after RVE computation
                NLT->retrieveMatLawFromRVE();
                // compute the tangential matrix stiffness at macroscale
```

```
                NLT->rveComputeTangentMatrix();
                // compute the residual force vector at macroscale
                NLT->rveComputeForceVector();
                // solve the linear system to get incremental nodal displacement
                NLT->solveLinearSystem();
                // update the solution field
                NLT->updateSolutionField();
                // increase the index for nonlinear iteration
                Current nonlinear iteration ++;
        }
        While (norm > tolerance)
Current load step ++;
End Loop
```

(2) Pseudo code of RVE computation

```
// retrieve nodal displacement at each macro element
NLT->retrieveCoordsDisp();
// pass nodal displacement of the macro element to RVE
RVE->setupCoordsDisp();
// Run RVE
RVE->run();
// calculate averaged stress
RVE->calculateAveragedStress();
// calculate the body force (Q term)
RVE->calculateBodyForceQterm();
// calculate the averaged stress derivative with respect to nodal displacement of macro element
RVE->calculateStressDerivative();
```

4. Class definitions for macro-scale and micro-scale

```
Class NonLinTissue : FiniteElementAnalysis {

Public:

// Initialization
void init();

// Apply dirichlet(essential) boundary condition
virtual void dirichlet();

// Apply Neumann boundary condition
```

```
void neumann();

// Run the macroscale computation
int run(bool);

// Set the maximum number of nonlinear iteration
void setNoOfIterations(int noiters);

// Set the convergence tolerance
void setConvTol(double convtol);

// Set total number of load steps
void setNumberOfLoadStep(int NbLoadStep);

// Write the mesh after deformation in VTK format
void writeToVTK(char *);

Private:

// Assemble tangential stiffness matrix and force vector
void assembleSystem (const std::string &systemName = "Default");

// Compute residual force vector at macroscale
void rveComputeForceVector(int, int, int, const std::string &, const
FiniteElementAnalysis::TimeDerivative, const bool, const std::string &);

// Compute tangential stiffness matrix at macroscale
void rveComputeTangentMatrix(int, int, int, const std::string &, const
FiniteElementAnalysis::TimeDerivative, const bool, const std::string &);

// Compute element tangent stiffness matrix
double * computeElementTangentStiffMatrix(pEntity, FiniteElementField*) ;

// Compute element residual force vector
double * computeElementForceVector(pEntity, FiniteElementField*) ;

// Apply the initial guess to the current displacement field
bool SetInitialGuess();

// Set up material parameter in the linear elasticity computation
bool SetupLinElasticity(pGModel model, pMesh inMesh);

// Run linear elasticity computation
bool ComputeLinElasticity();

// Retrieve averaged stress and stress derivative on pEntity
SCOREC_Core::RVEInfo * retrieveMatLawFromRVE(pEntity, int);

// Execute microscale RVE computation on all macro elements
void computeRVEs(FiniteElementField*);

}


Class  RepresentVolElem {
```

Public:

// pass initial coordinates of nodes of macro finite element to RVE
void setupInitCoords(double *initCoords);
// pass nodal displacement of the macro element to RVE
void setupCoordsDisp(double *coordDisp);

// run RVE computation
void run(int iter =0);

// Output the fiber configuration in VTK format
void outputFiberToVTK(const char *);

Private:

// pointer to array of fiber nodes
node_struct *arrnode;

// pointer to array of fiber elements
elmt_struct *arrelmt;

// read in network information
void read_init_net(char *finname,int pas);

// calculate averaged stress, body force and stress derivative
void calc_stress(double fvec[],double vstress[], int pas);
void avgvolstress(double fvec[],double vstress[],double loc_vastrx[], double loc_vastry[],double loc_vastrz[],double vol,double coords_loc[], int nfe, int pas,double init_coords_loc[],double fem_res_norm);
void calc_femjacob_newmethod(double dSdx[],int pas,double vol,double dvol[],double vstress[],int tag,double init_coords_loc[],int nfe,int iter,int nmesh);

5. Nonlinear finite element formulation

The principle of virtual displacement with incremental decomposition is

$$\int_V \Delta\sigma_{ij}\delta\Delta\varepsilon_{ij}dV + \int_V \sigma_{ij}\delta\Delta\eta_{ij}dV = R - \int_V \sigma_{ij}\delta\Delta e_{ij}dV \tag{A.1}$$

with

$$\Delta\varepsilon_{ij} = \Delta e_{ij} + \Delta\eta_{ij} \tag{A.2}$$

$$\Delta e_{ij} = \frac{1}{2}(\Delta u_{i,j} + \Delta u_{j,i}), \Delta\eta_{ij} = \frac{1}{2}\Delta u_{k,i}\Delta u_{k,j} \tag{A.3}$$

$$R = \int_V Q_i\delta\Delta u_i dV \tag{A.4}$$

where $\Delta\sigma_{ij}$ and $\Delta\varepsilon_{ij}$ are incremental unknown stress and strain from last known state to the known state , σ_{ij} is the Cauchy stress at last known state which is returned as averaged stress from the RVE constructed at the Gauss point, R is the virtual external

work done by Q_i , which is the body force returned from the RVE constructed at the Gauss point and Δu is incremental displacement from iteration i to iteration i+1.

Using Taylor's series,

The first term in the left hand side of Eq.(A.1) is expanded as

$$\int_V \Delta\sigma_{ij}\delta\Delta\varepsilon_{ij}dV = \int_V \frac{\partial\sigma_{ij}}{\partial u_l^k}\Delta u_l^k \delta\Delta\varepsilon_{ij}dV \doteq \int_V \frac{\partial\sigma_{ij}}{\partial u_l^k}\Delta u_l^k \delta\Delta e_{ij}dV = \int_V \tilde{C}_{ijkl}\Delta u_l^k \delta\Delta e_{ij}dV \quad \text{(A.5)}$$

$$\tilde{C}_{ijkl} = \frac{\partial\sigma_{ij}}{\partial u_l^k} \quad \text{(A.6)}$$

where u_l^k is the component l of displacement vector at node k of the macro finite element; $\frac{\partial\sigma_{ij}}{\partial u_l^k}$ is the derivative of the averaged stress (returned from RVE) with respect to the nodal displacement of the macro finite element.

Substituting (A.5) into (A.1), Eq.(A.1) becomes

$$\int_V \tilde{C}_{ijkl}\Delta u_l^k \delta\Delta e_{ij}dV + \int_V \sigma_{ij}\delta\Delta\eta_{ij}dV = \int_V Q_i\delta\Delta u_i dV - \int_V \sigma_{ij}\delta\Delta e_{ij}dV \quad \text{(A.7)}$$

Writing (A.7) into matrix form,

$$\int_V \tilde{C}_{ijkl}\Delta u_l^k \delta\Delta e_{ij}dV = \delta\Delta\boldsymbol{u}^T\left(\int_V \boldsymbol{B}_{L0}{}^T\tilde{\boldsymbol{C}}dV\right)\boldsymbol{\Delta u} = \delta\Delta\boldsymbol{u}^T\boldsymbol{K}_L\boldsymbol{\Delta u} \quad \text{(A.8a)}$$

$$\int_V \sigma_{ij}\delta\Delta\eta_{ij}dV = \delta\Delta\boldsymbol{u}^T\left(\int_V \boldsymbol{B}_{NL}{}^T\tilde{\boldsymbol{\sigma}}\boldsymbol{B}_{NL}dV\right)\boldsymbol{\Delta u} = \delta\Delta\boldsymbol{u}^T\boldsymbol{K}_{NL}\boldsymbol{\Delta u} \quad \text{(A.8b)}$$

$$\int_V Q_i\delta\Delta u_i dV = \delta\Delta\boldsymbol{u}^T\int_V \tilde{\boldsymbol{N}}^T\boldsymbol{Q}dV = \delta\Delta\boldsymbol{u}^T\boldsymbol{P} \quad \text{(A.8c)}$$

$$\int_V \sigma_{ij}\delta\Delta e_{ij}dV = \delta\Delta\boldsymbol{u}^T\left(\int_V \boldsymbol{B}_{L0}{}^T\boldsymbol{\sigma}dV\right) = \delta\Delta\boldsymbol{u}^T\boldsymbol{F} \quad \text{(A.8d)}$$

$$\begin{aligned}&\delta\Delta\boldsymbol{u}^T\boldsymbol{K}_L\boldsymbol{\Delta u} + \delta\Delta\boldsymbol{u}^T\boldsymbol{K}_{NL}\boldsymbol{\Delta u}\\ &= \delta\Delta\boldsymbol{u}^T\int_V \tilde{\boldsymbol{N}}^T\boldsymbol{Q}dV - \delta\Delta\boldsymbol{u}^T\left(\int_V \boldsymbol{B}_{L0}{}^T\boldsymbol{\sigma}dV\right)\end{aligned} \quad \text{(A.8e)}$$

$$(\boldsymbol{K}_L + \boldsymbol{K}_{NL})\Delta\boldsymbol{u} = \boldsymbol{P} - \boldsymbol{F} \quad \text{(A.8f)}$$

where

$$\tilde{C}=\begin{bmatrix} C_{1111} & C_{1122} & C_{1133} & C_{1112} & C_{1123} & C_{1131} \\ C_{2211} & C_{2222} & C_{2233} & C_{2212} & C_{2223} & C_{2231} \\ C_{3311} & C_{3322} & C_{3333} & C_{3312} & C_{3323} & C_{3331} \\ C_{1211} & C_{1222} & C_{1233} & C_{1212} & C_{1223} & C_{1231} \\ C_{2311} & C_{2322} & C_{2333} & C_{2333} & C_{2323} & C_{2323} \\ C_{3111} & C_{3122} & C_{3133} & C_{3133} & C_{3123} & C_{3123} \end{bmatrix}=\begin{bmatrix} \frac{\partial\sigma_{11}}{\partial u_1^1} & \frac{\partial\sigma_{11}}{\partial u_2^1} & \frac{\partial\sigma_{11}}{\partial u_3^1} & \frac{\partial\sigma_{11}}{\partial u_1^2} & \cdots & \frac{\partial\sigma_{11}}{\partial u_3^4} \\ \frac{\partial\sigma_{22}}{\partial u_1^1} & \frac{\partial\sigma_{22}}{\partial u_2^1} & \frac{\partial\sigma_{22}}{\partial u_3^1} & \frac{\partial\sigma_{22}}{\partial u_1^2} & \cdots & \frac{\partial\sigma_{22}}{\partial u_3^4} \\ \frac{\partial\sigma_{33}}{\partial u_1^1} & \frac{\partial\sigma_{33}}{\partial u_2^1} & \frac{\partial\sigma_{33}}{\partial u_3^1} & \frac{\partial\sigma_{33}}{\partial u_1^2} & \cdots & \frac{\partial\sigma_{33}}{\partial u_3^4} \\ \frac{\partial\sigma_{12}}{\partial u_1^1} & \frac{\partial\sigma_{12}}{\partial u_2^1} & \frac{\partial\sigma_{12}}{\partial u_3^1} & \frac{\partial\sigma_{12}}{\partial u_1^2} & \cdots & \frac{\partial\sigma_{12}}{\partial u_3^4} \\ \frac{\partial\sigma_{23}}{\partial u_1^1} & \frac{\partial\sigma_{23}}{\partial u_2^1} & \frac{\partial\sigma_{23}}{\partial u_3^1} & \frac{\partial\sigma_{23}}{\partial u_1^2} & \cdots & \frac{\partial\sigma_{23}}{\partial u_3^4} \\ \frac{\partial\sigma_{31}}{\partial u_1^1} & \frac{\partial\sigma_{31}}{\partial u_2^1} & \frac{\partial\sigma_{31}}{\partial u_3^1} & \frac{\partial\sigma_{31}}{\partial u_1^2} & \cdots & \frac{\partial\sigma_{31}}{\partial u_3^4} \end{bmatrix}_{6\times 12}$$

The entries in the above matrix are returned from the RVE computation.

$$B_{L0}=\begin{bmatrix} N_{1,1} & 0 & 0 & N_{2,1} & 0 & 0 & N_{3,1} & 0 & 0 & N_{4,1} & 0 & 0 \\ 0 & N_{1,2} & 0 & 0 & N_{2,2} & 0 & 0 & N_{3,2} & 0 & 0 & N_{4,2} & 0 \\ 0 & 0 & N_{1,3} & 0 & 0 & N_{2,3} & 0 & 0 & N_{3,3} & 0 & 0 & N_{4,3} \\ N_{1,2} & N_{1,1} & 0 & N_{2,2} & N_{2,1} & 0 & N_{3,2} & N_{3,1} & 0 & N_{4,2} & N_{4,1} & 0 \\ 0 & N_{1,3} & N_{1,2} & 0 & N_{2,3} & N_{2,2} & 0 & N_{3,3} & N_{3,2} & 0 & N_{4,3} & N_{4,2} \\ N_{1,3} & 0 & N_{1,1} & N_{2,3} & 0 & N_{2,1} & N_{3,3} & 0 & N_{3,1} & N_{4,3} & 0 & N_{4,1} \end{bmatrix}_{6\times 12}$$

Where $N_{i,j}$ is the shape function at node i with respect to component j of spatial coorindates.

$$\boldsymbol{B}_{NL}=\begin{bmatrix} \tilde{\boldsymbol{B}}_{\boldsymbol{NL}} & \tilde{\boldsymbol{0}} & \tilde{\boldsymbol{0}} \\ \tilde{\boldsymbol{0}} & \tilde{\boldsymbol{B}}_{\boldsymbol{NL}} & \tilde{\boldsymbol{0}} \\ \tilde{\boldsymbol{0}} & \tilde{\boldsymbol{0}} & \tilde{\boldsymbol{B}}_{\boldsymbol{NL}} \end{bmatrix}_{9\times 12},\tilde{\boldsymbol{0}}=\begin{bmatrix} 0 \\ 0 \\ 0 \end{bmatrix}$$

$$\tilde{\boldsymbol{B}}_{\boldsymbol{NL}}=\begin{bmatrix} N_{1,1} & 0 & 0 & N_{2,1} & 0 & 0 & N_{3,1} & 0 & 0 & N_{4,1} \\ N_{1,2} & 0 & 0 & N_{2,2} & 0 & 0 & N_{3,2} & 0 & 0 & N_{4,2} \\ N_{1,3} & 0 & 0 & N_{2,3} & 0 & 0 & N_{3,2} & 0 & 0 & N_{4,3} \end{bmatrix}$$

$$\tilde{\boldsymbol{\sigma}}=\begin{bmatrix} \hat{\boldsymbol{\sigma}} & \hat{\boldsymbol{0}} & \hat{\boldsymbol{0}} \\ \hat{\boldsymbol{0}} & \hat{\boldsymbol{\sigma}} & \hat{\boldsymbol{0}} \\ \hat{\boldsymbol{0}} & \hat{\boldsymbol{0}} & \hat{\boldsymbol{\sigma}} \end{bmatrix}_{9\times 9},\hat{\boldsymbol{\sigma}}=\begin{bmatrix} \sigma_{11} & \sigma_{12} & \sigma_{13} \\ \sigma_{12} & \sigma_{22} & \sigma_{23} \\ \sigma_{13} & \sigma_{23} & \sigma_{33} \end{bmatrix},\hat{\boldsymbol{0}}=\begin{bmatrix} 0 & 0 & 0 \\ 0 & 0 & 0 \\ 0 & 0 & 0 \end{bmatrix}$$

$$\boldsymbol{\sigma}=\begin{bmatrix} \sigma_{11} & \sigma_{22} & \sigma_{33} & \sigma_{12} & \sigma_{23} & \sigma_{13} \end{bmatrix}^T$$

The entries in the stress matrix and vector are returned from RVE computation.

$$\tilde{\boldsymbol{N}} = \begin{bmatrix} \tilde{\boldsymbol{N}}_1 & \tilde{\boldsymbol{N}}_2 & \tilde{\boldsymbol{N}}_3 & \tilde{\boldsymbol{N}}_4 \end{bmatrix}_{3\times 12}$$

$$\tilde{\boldsymbol{N}}_1 = \begin{bmatrix} N_1 & 0 & 0 \\ 0 & N_1 & 0 \\ 0 & 0 & N_1 \end{bmatrix}, \tilde{\boldsymbol{N}}_2 = \begin{bmatrix} N_2 & 0 & 0 \\ 0 & N_2 & 0 \\ 0 & 0 & N_2 \end{bmatrix}, \tilde{\boldsymbol{N}}_3 = \begin{bmatrix} N_3 & 0 & 0 \\ 0 & N_3 & 0 \\ 0 & 0 & N_3 \end{bmatrix}, \tilde{\boldsymbol{N}}_4 = \begin{bmatrix} N_4 & 0 & 0 \\ 0 & N_4 & 0 \\ 0 & 0 & N_4 \end{bmatrix}$$